

# **Following the trails of light in curved spacetime**

by

**Darius Bunandar**

**THESIS**

Presented in Partial Fulfillment  
of the Requirements for the Degree of

**Bachelor of Science in Physics**

The University of Texas at Austin

Austin, Texas

May 2013

The Thesis Committee for Darius Bunandar  
certifies that this is the approved version of the following thesis:

## **Following the trails of light in curved spacetime**

Committee:

---

Richard A. Matzner, Supervisor

---

Philip J. Morrison

---

Greg O. Sitz

© 2013 - *DARIUS BUNANDAR*

*ALL RIGHTS RESERVED.*

# Following the trails of light in curved spacetime

Darius Bunandar

The University of Texas at Austin, 2013

Supervisor: Richard A. Matzner

Light has played an instrumental role in the initial development of the theory of relativity. In this thesis, we intend to explore other physical phenomena that can be explained by tracing the path that light takes in curved spacetime. We consider the null geodesic and eikonal equations that are equivalent descriptions of the propagation of light rays within the framework of numerical relativity. We find that they are suited for different physical situations. The null geodesic equation is more suited for tracing the path of individual light rays. We solve this equation in order to visualize images of the sky that have been severely distorted by one or more black holes, the so-called gravitational lensing effect. We demonstrate that our procedure of solving the null geodesic equation is sufficiently robust to produce some of the world's first images of the lensing effect from fully dynamical binary black hole coalescence. The second formulation of propagation of light that we explore is the eikonal surface equation. Because this equation describes the propagation of whole surfaces of light, instead of individual light rays, we find it more apt in locating the event horizon of a black hole. We will

show that our solution method of the eikonal surface equation to locate event horizons is also robust enough to find the event horizon of a black hole that has accreted some negative energy density. While both of these numerical simulations were able to achieve their basic goals for dynamical spacetimes where solution by analytical methods is impractical, both simulations are limited by computational requirements that we discuss.

# Contents

1	INTRODUCTION	1
2	THEORETICAL FOUNDATIONS	4
2.1	The ADM Formalism . . . . .	4
2.2	Null Geodesic Equations . . . . .	7
2.3	The Eikonal Equation . . . . .	12
3	GRAVITATIONAL LENSING	15
3.1	Background and Motivation . . . . .	15
3.2	Implementation . . . . .	17
3.2.1	Initial Conditions . . . . .	18
3.2.2	Background Image . . . . .	23
3.3	Single Black Hole Cases . . . . .	24
3.3.1	The Kerr-Schild Metric . . . . .	24
3.3.2	Comparison against analytical integration . . . . .	26
3.3.3	Results . . . . .	34

3.4	Equal Mass Binary Black Holes . . . . .	46
3.5	Summary and Future Considerations . . . . .	58
4	FINDING THE EVENT HORIZON	60
4.1	Background and Motivation . . . . .	60
4.2	Black Holes . . . . .	62
4.2.1	Event Horizon . . . . .	62
4.2.2	Apparent Horizon . . . . .	65
4.2.3	Notions of Extremality . . . . .	67
4.3	Numerical Method . . . . .	70
4.3.1	Pseudospectral Collocation Method . . . . .	70
4.3.2	Choice of Domain and Basis Functions . . . . .	72
4.3.3	Choice of Collocation Points . . . . .	75
4.3.4	Time Evolution and Boundary Conditions . . . . .	76
4.3.5	Extraction of Null Surface and Initial Conditions . . . . .	78
4.3.6	Reinitialization . . . . .	79
4.3.7	Area Calculation . . . . .	80
4.3.8	Obtaining Metric Data . . . . .	82
4.4	Application to Puncture Black Holes . . . . .	83
4.4.1	Non-spinning Puncture Black Hole . . . . .	84
4.4.2	Puncture Black Hole with $a = 0.8M$ . . . . .	91
4.5	Puncture Black Hole with Negative Energy Density . . . . .	103
4.6	Summary and Future Considerations . . . . .	110

5	CONCLUSIONS	112
	APPENDIX A STRONG STABILITY PRESERVING RUNGE-KUTTA (SSPRK)	114
	REFERENCES	116



# Figures

3.1	A schematic of tracking the paths of photons backwards in time from the observer to their supposed origin. The paths of the photons are bent because of the strong gravitational field produced by the black holes. . . . .	17
3.2	Schematic of the spatial orthonormal vectors in relation to the pinhole camera. . . . .	19
3.3	A grid with the gradient color map. The projected angular positions of some lines are denoted, where $\theta$ is the latitude and $\phi$ is the longitude. . . . .	24
3.4	A gradient color map grid distorted by a non-spinning black hole. The arrow indicates the location of the Einstein ring in the image. The resolution of the pinhole camera is $300 \times 300$ in this case. . . . .	27

3.5	Plots comparing the trajectories of two photons: one that has originated from the night sky (red) and one that has originated from just outside the black hole (blue). The cyan points are those that are obtained from integrating the normalized form of the null geodesic equation backwards in time, and they are truncated earlier than the lines of trajectories obtained from analytical integration (red and blue). . . . .	32
3.6	Plots comparing the difference in trajectories obtained from integrating the null geodesic equation and those obtained from integrating the photons' equations of motion. The photon that has originated from the night sky is red and the photon that has originated from just outside the black hole is blue. . . . .	33
3.7	Side view image of the gradient color map distorted by a single black hole with no spin at camera resolution of $300 \times 300$ . .	36
3.8	Side view image of the gradient color map distorted by a single black hole with a spin of $0.2510M$ at camera resolution of $300 \times 300$ . . . . .	37
3.9	Side view image of the gradient color map distorted by a single black hole with a spin of $0.5035M$ at camera resolution of $300 \times 300$ . . . . .	38
3.10	Side view image of the gradient color map distorted by a single black hole with a spin of $0.7478 M$ at camera resolution of $300 \times 300$ . . . . .	39

3.11	Side view image of the gradient color map distorted by a single black hole with a spin of $0.9999M$ (nearly maximal spin) at camera resolution of $300 \times 300$ . . . . .	40
3.12	Top-down view image of the gradient color map distorted by a single black hole with no spin at camera resolution of $300 \times 300$ . . . . .	41
3.13	Top-down view image of the gradient color map distorted by a single black hole with a spin of $0.2510M$ at camera resolution of $300 \times 300$ . . . . .	42
3.14	Top-down view image of the gradient color map distorted by a single black hole with a spin of $0.5035M$ at camera resolution of $300 \times 300$ . . . . .	43
3.15	Top-down view image of the gradient color map distorted by a single black hole with a spin of $0.7478M$ at camera resolution of $300 \times 300$ . . . . .	44
3.16	Top-down view image of the gradient color map distorted by a single black hole with a spin of $0.9999M$ (nearly extremal spin) at camera resolution of $300 \times 300$ . . . . .	45
3.17	Side view image of the gradient color map distorted by equal mass binary black holes at $t = 3937M$ at camera resolution of $300 \times 300$ . . . . .	49

3.18	Side view image of the gradient color map distorted by equal mass binary black holes at $t = 3941M$ at camera resolution of $300 \times 300$ . . . . .	50
3.19	Side view image of the gradient color map distorted by equal mass binary black holes at $t = 3946M$ at camera resolution of $300 \times 300$ . . . . .	51
3.20	Side view image of the gradient color map distorted by equal mass binary black holes at $t = 3951M$ at camera resolution of $300 \times 300$ . . . . .	52
3.21	Side view image of the gradient color map distorted by equal mass binary black holes at $t = 3956M$ at camera resolution of $300 \times 300$ . . . . .	53
3.22	Side view image of the gradient color map distorted by equal mass binary black holes at $t = 3961M$ at camera resolution of $300 \times 300$ . . . . .	54
3.23	Side view image of an equal mass binary black hole inspiral observed at $t = 3937M$ . The trajectories of three labeled photons—one outside the Einstein ring, one inside the Einstein ring, and one inside the slit between the two black holes—are plotted in Fig. 3.24 . . . . .	55

3.24	Trajectories of three photons labeled in Fig. 3.23, started at $t = 3937M$ and evolved backwards in time. The yellow trajectory corresponds to photon A, the cyan trajectory corresponds to photon B, and the green trajectory corresponds to photon C. The blue and red spheres are the apparent horizons of the two equal mass black holes. From top to bottom, left to right, the snapshots are taken at times $t = 3874M, t = 3872M, t = 3870M, t = 3867M, t = 3860M$ , and $t = 3855M$ . . . . .	56
3.25	Top-down view image of the gradient color map distorted by equal mass binary black holes at $t = 3167M$ at camera resolution of $300 \times 300$ . . . . .	57
4.1	A comparison between the maximum and minimum radial coordinate locations for both the null surface $\Gamma_N$ and the apparent horizon. In this case, $N_r = 40$ and $L = 30$ . The black hole is a non-spinning puncture black hole. The event horizon finder starts at $t = 50M$ and evolves backwards in time. . . . .	87
4.2	A comparison between the area of the null surface $\Gamma_N$ and the area of the apparent horizon. In this particular case $N_r = 40$ and $L = 30$ . The black hole is a non-spinning puncture black hole. The event horizon finder starts at $t = 50M$ and evolves backwards in time. . . . .	88

4.3	Absolute difference in the radial coordinate location between the null surface $\Gamma_N$ and the apparent horizon, for different orders of Chebyshev expansion: $N_r = 30, 40, 50, 60, 70$ . The black hole is a non-spinning puncture black hole. The order of spherical harmonic expansion is kept fixed at $L = 30$ . The event horizon finder starts at $t = 50M$ and evolves backwards in time. The growing difference at late times reflects the event horizon tracker's exponential approach to the horizon, as it is evolved backwards in time. . . . .	89
4.4	Normalized absolute area difference between the null surface $\Gamma_N$ and the apparent horizon, for different orders of Chebyshev expansion: $N_r = 30, 40, 50, 60, 70$ . The black hole is a non-spinning puncture black hole. The order of spherical harmonic expansion is kept fixed at $L = 30$ . The event horizon finder starts at $t = 50M$ and evolves backwards in time. The growing difference at late times reflects the event horizon tracker's exponential approach to the horizon, as it is evolved backwards in time. . . . .	90

4.5	A comparison between the maximum and minimum radial coordinate locations for both the null surface $\Gamma_N$ and the apparent horizon. In this particular case $N_r = 40$ and $L = 30$ . The black hole is a puncture black hole with a spin of $J/M = a = 0.8M$ . The event horizon finder starts at $t = 75M$ and evolves backwards in time. . . . .	95
4.6	A comparison between the area of the null surface $\Gamma_N$ and the area of the apparent horizon. In this particular case $N_r = 40$ and $L = 30$ . The black hole is a puncture black hole with a spin of $J/M = a = 0.8M$ . The event horizon finder starts at $t = 75M$ and evolves backwards in time. . . . .	96
4.7	Normalized absolute area difference between the null surface $\Gamma_N$ and the apparent horizon, for different orders of Chebyshev expansion: $N_r = 30, 40, 50, 60, 70$ . The black hole is a puncture black hole with a spin of $J/M = a = 0.8M$ . The order of spherical harmonic expansion is kept fixed at $L = 30$ . The event horizon finder starts at $t = 75M$ and evolves backwards in time. The growing difference at late times reflects the event horizon tracker's exponential approach to the horizon, as it is evolved backwards in time. . . . .	97

- 4.8 Normalized absolute area difference between the null surface  $\Gamma_N$  and the apparent horizon, for different orders of spherical harmonic expansion:  $L = 16, 20, 24, 28, 30$ . The black hole is a puncture black hole with a spin of  $J/M = a = 0.8M$ . The order of Chebyshev expansion is kept fixed at  $N_r = 40$ . The event horizon finder starts at  $t = 75M$  and evolves backwards in time. The growing difference at late times reflects the event horizon tracker's exponential approach to the horizon, as it is evolved backwards in time. . . . . 98
- 4.9 Absolute difference in the *maximum* radial coordinate location between the null surface  $\Gamma_N$  and the apparent horizon, for different orders of Chebyshev expansion:  $N_r = 30, 40, 50, 60, 70$ . The black hole is a puncture black hole with a spin of  $J/M = a = 0.8M$ . The order of spherical harmonic expansion is kept fixed at  $L = 30$ . The event horizon finder starts at  $t = 75M$  and evolves backwards in time. The growing difference at late times reflects the event horizon tracker's exponential approach to the horizon, as it is evolved backwards in time. . . . 99



- 4.10 Absolute difference in the *maximum* radial coordinate location between the null surface  $\Gamma_N$  and the apparent horizon, for different orders of spherical harmonic expansion:  $L = 16, 20, 24, 28, 30$ . The black hole is a puncture black hole with a spin of  $J/M = a = 0.8M$ . The order of Chebyshev expansion is kept fixed at  $N_r = 40$ . The event horizon finder starts at  $t = 75M$  and evolves backwards in time. The growing difference at late times reflects the event horizon tracker's exponential approach to the horizon, as it is evolved backwards in time. . . . . 100
- 4.11 Absolute difference in the *minimum* radial coordinate location between the null surface  $\Gamma_N$  and the apparent horizon, for different orders of Chebyshev expansion:  $N_r = 30, 40, 50, 60, 70$ . The black hole is a puncture black hole with a spin of  $J/M = a = 0.8M$ . The order of spherical harmonic expansion is kept fixed at  $L = 30$ . The event horizon finder starts at  $t = 75M$  and evolves backwards in time. The anomalously small differences found for  $L = 16$  is probably due to an intersection between the specific values of  $L$  and  $N_r$ . The growing difference at late times reflects the event horizon tracker's exponential approach to the horizon, as it is evolved backwards in time. 101

4.12	Absolute difference in the <i>minimum</i> radial coordinate location between the null surface $\Gamma_N$ and the apparent horizon, for different orders of spherical harmonic expansion: $L = 16, 20, 24, 28, 30$ . The black hole is a puncture black hole with a spin of $J/M = a = 0.8M$ . The order of Chebyshev expansion is kept fixed at $N_r = 40$ . The event horizon finder starts at $t = 75M$ and evolves backwards in time. The growing difference at late times reflects the event horizon tracker's exponential approach to the horizon, as it is evolved backwards in time. . . . .	102
4.13	A comparison between the maximum and minimum radial coordinate locations for both the null surface $\Gamma_N$ and the apparent horizon. The black hole is a puncture black hole with a spin of $a = 0.8M$ that has accreted some negative energy density. The apparent high-frequency oscillations in the maximum radial coordinate location $r_{EH,max}$ and the absence of it in the minimum radial coordinate location $r_{EH,min}$ are effects of numerical instabilities. The event horizon finder starts at $t = 200M$ and evolves backwards in time. . . . .	106

4.14	A comparison between the area of the null surface $\Gamma_N$ and the area of the apparent horizon. The black hole is a puncture black hole with a spin of $a = 0.8M$ that has accreted some negative energy density. The event horizon finder starts at $t = 200M$ and evolves backwards in time. . . . .	107
4.15	Normalized absolute area difference between the null surface $\Gamma_N$ and the apparent horizon. The black hole is a puncture black hole with a spin of $a = 0.8M$ that has accreted some negative energy density. The event horizon finder starts at $t = 200M$ and evolves backwards in time. The growing difference at late times reflects the event horizon tracker's exponential approach to the horizon, as it is evolved backwards in time. . .	108
4.16	A comparison between the different radial coordinate locations of the null surface $\Gamma_N$ at the equator ( $\theta = \pi/2$ )—showing the loss of axisymmetry. The black hole is a puncture black hole with a spin of $a = 0.8M$ that has accreted some negative energy density. Only evolution between $t = 50M$ and $t = 200M$ is shown. . . . .	109

TO MY FAMILY, FOR BELIEVING.

# Acknowledgments

I owe my deepest gratitude to my advisor, Prof. Richard Matzner, who taught me everything I know about general relativity. I extend my most sincere thanks to Prof. Matzner for his insight, guidance and tremendous patience. I am especially grateful to have worked under his mentorship.

I would like to thank members of the Caltech-Cornell SXS Collaboration, especially Mark Scheel, Nicholas Taylor, Andrew Bohn, Francois Hebert, and William Throwe, for welcoming and mentoring me in their gravitational lensing project. I benefited tremendously from those short three months I spent at Caltech. I am also indebted to Tanja Bode who helped me immensely by providing the spacetime data for my rudimentary event horizon finder program, despite her hectic schedule.

It is a great pleasure for me to thank my friends at UT for all the caffeine, the joy, and the laughter that we shared. I am grateful to Victor Chua, Gabriel Elpers, Giovanni Rossi, James Kubricht, Aditi Raye Allen, Michelle Rascati, William Berdanier, and Hayley Manning. I have always felt their

support throughout my years at UT. Those years would not have been the same without them.

I wish to thank my sister and my brother-in-law, Erika and Timothy Coffey, for supporting me and caring for me throughout my undergraduate career. It has been a pleasure living with them in Austin, but it's time to move on. I would like to thank my little niece, Alanna Coffey, for reminding me what blissfulness is.

Lastly, and most importantly, I wish to thank my parents: Sudono Lukito and Kiki Rejeki Bunandar. I owe my whole life to them for nurturing me, supporting me, loving me, and believing in me.

# 1

## Introduction

Light has played a special role in the development of the theory of relativity. The theory of relativity was developed as a resolution to the problem of the constancy of the speed of light. When James Clerk Maxwell formulated the laws of electromagnetism in the 1860's, he demonstrated that light is an oscillation of electromagnetic field, and it propagates at a constant speed of approximately 300,000 km/s in air. He pointed out that the calculated speed agreed well with the speed of light measured by Hippolyte Fizeau and Léon Foucault [1]. With the Newton's laws of motion and its Galilean symmetry being the only physical theory of motion, it was natural to deduce that only in one inertial frame is 300,000 km/s the measured speed of light. This observation led to theories postulating the existence of ether: an invisible medium in which light propagates and in which it achieves its "natural" speed. However, an experiment done by two American physicists—Albert Michelson and Edward Morley—showed that the speed of light is 300,000 km/s in *any* reference frame—in disagreement with expectations of an ether theory. The Special Theory of Relativity was proposed by Einstein in 1905 as

a resolution to this crisis. Realizing that the theory of special relativity was on the surface incompatible with Newton's law of gravity, Einstein spent the next decade trying to reconcile the two theories. His effort resulted in the General Theory of Relativity in which he used the language and tools of differential geometry to explain how spacetime is really a geometrical four-dimensional "surface" where trajectories of bodies are curves on this surface. More importantly, the presence of energy curves this surface and in turn curvature affects the motion of bodies which carry energy.

The significant role that light played in the theory of relativity did not stop there. One of the most famous first test for general relativity was the gravitational deflection of starlight by the sun. Although Newton's law of gravity also predicts a deflection of starlight by the sun, the angular deflection predicted by Newton's gravity was half of the angular deflection calculated by Einstein using general relativity. In the first days following World War I, Arthur Eddington led an expedition to the island of Principe to observe the change in the position of stars that can be found near the sun during a solar eclipse. His results confirmed Einstein's prediction. Therefore, light is not only instrumental in the initial development of the theory of relativity, but observations made of light were the first confirmation of the General Theory of Relativity.

In the same spirit of these early light deflection experiments, this thesis will further explore other physical phenomena that can be explained by following—or "ray-tracing"—the path that light takes in curved spacetime.



Chapter 3 explores how the deflection of light can make the night sky appear distorted near the presence of one or more black holes. Then, Chapter 4 explores how the event horizon of a black hole can be found by following the path of light rays. However, before delving into the main results of our exploration of these physical phenomena, the theoretical framework needed to derive these results is presented in Chapter 2. Finally, conclusions are presented in Chapter 5.

Throughout this thesis, we will use the mathematical framework of tensor calculus and differential geometry. An excellent introduction to the subject may be found in Ref. [2] or [3], and we will assume that the reader is familiar with this formalism.

# 2

## Theoretical Foundations

### 2.1 THE ADM FORMALISM

One of the primary goals of numerical relativity is to approximately—but with sufficient accuracy—solve the Einstein’s field equations on a computer for a spacetime whose analytical form is either difficult to distill or does not exist. Some examples of such a spacetime includes the physical situations of perturbed black holes [4], neutron stars [5, 6], coalescence of black holes [7, 8, 9] coalescence of neutron stars [10, 11], as well as coalescence of a black hole-neutron star system [12, 13]. To achieve this goal, the Einstein’s field equations needs to be casted into a form that is suited for numerical integration.

Perhaps the most common approach is the Arnowitt, Deser, Misner (ADM) formalism that recasts spacetime into three dimensional space and one dimensional time [14, 15]. Such 3+1 formulation, in consequence, recasts the Einstein’s field equations in terms of a traditional initial value problem.

The ADM formalism considers the foliation of the spacetime  $(M, g_{\alpha\beta})$

into a family of non-intersecting spacelike 3-dimensional hypersurfaces  $\Sigma_t$  of constant scalar function  $t$ , which can be interpreted as some global time coordinate. Let  $n^\alpha$  be a vector normal to the hypersurface  $\Sigma_t$ , then the direction of increasing time is defined by<sup>1</sup>

$$t^\alpha = \alpha n^\alpha + \beta^\alpha, \quad (2.1)$$

where  $\alpha$  is the lapse function and  $\beta^\alpha \rightarrow (0, \beta^i)$  is the *spatial* shift vector. The lapse function  $\alpha$  measures how much proper time has elapsed between neighboring 3-surfaces  $\Sigma_t$  along the direction of the vector  $t^\alpha$ . On the other hand, the shift vector measures the amount by which the spatial coordinates are shifted within the neighboring 3-surfaces  $\Sigma_t$  along the direction of the vector  $t^\alpha$ . Both the lapse and shift functions can be arbitrarily specified according to the choice of coordinates. The freedom to choose the four functions  $\alpha$  and  $\beta^i$  corresponds to the four coordinate degrees of freedom in general relativity.

With the normal vector, the spatial metric that is induced by the spacetime metric  $g_{\alpha\beta}$  on the 3-dimensional hypersurface  $\Sigma_t$  is

$$\gamma_{\alpha\beta} = g_{\alpha\beta} + n_\alpha n_\beta. \quad (2.2)$$

---

<sup>1</sup>Throughout this thesis, we will adopt the conventions of Misner *et al.* [14], where the Greek alphabets ( $\alpha, \beta, \gamma, \dots$ ) will refer to the spacetime components (0, 1, 2, 3), and the Latin alphabets ( $a, b, c, \dots$ ) will indicate spatial components (1, 2, 3). We, however, reserve the alphabet  $t$  in the index to denote the time component, or the zeroth component. We will also adopt the  $(-, +, +, +)$  metric signature which is the convention in Misner *et al.*.

Along with the spatial metric, an extrinsic curvature that measures the rate at which the hypersurface deforms as it moves forward along the normal vector  $n^\alpha$  is <sup>2</sup>

$$\begin{aligned} K_{ij} &= -\gamma_i^j \gamma_k^l \nabla_j n_l \\ &= \frac{1}{2\alpha} \left( -\partial_t \gamma_{ij} + 2\gamma_{ik} \beta^k_{,j} + \gamma_{ij,m} \beta^m \right) \end{aligned} \quad (2.3)$$

The spacetime metric on  $M$  is therefore

$$g_{\alpha\beta} = \begin{pmatrix} -\alpha^2 + \beta_k \beta^k & \beta_i \\ \beta_j & \gamma_{ij} \end{pmatrix}, \quad (2.4)$$

and the inverse is

$$g^{\alpha\beta} = \begin{pmatrix} -1/\alpha^2 & \beta^i/\alpha^2 \\ \beta^j/\alpha^2 & \gamma^{ij} - \beta^i \beta^j/\alpha^2 \end{pmatrix}, \quad (2.5)$$

where the spatial indices are raised and lowered by the spatial metric  $\gamma_{ij}$  and its inverse  $\gamma^{ij}$ . Equivalently, the line element can be decomposed into the 3+1 form:

$$ds^2 = -\alpha^2 dt^2 + \gamma_{ij} (dx^i + \beta^i dt) (dx^j + \beta^j dt). \quad (2.6)$$

---

<sup>2</sup>In this thesis, we will also adopt the convenient conventions of Misner *et al.* with regards to derivatives. The symbol comma (,) in a tensor's index signifies partial derivative with respect to coordinate of the next index. For example,  $A_{\alpha,\beta} = \frac{\partial A_\alpha}{\partial x^\beta}$  and  $B^\alpha_{,\beta} = \frac{\partial B^\alpha}{\partial x^\beta}$ .

## 2.2 NULL GEODESIC EQUATIONS

Perhaps the most straightforward way of following the light rays—or photons—is by integrating the null geodesic equation [14]:

$$\frac{d^2 x^\mu}{d\lambda^2} + \Gamma^\mu_{\alpha\beta} \frac{dx^\alpha}{d\lambda} \frac{dx^\beta}{d\lambda} = 0, \quad (2.7)$$

where  $x^\mu = x^\mu(\lambda)$  is the position of the photon along the geodesic, and  $\lambda$  is an affine parameter for the photon.  $\Gamma^\mu_{\alpha\beta}$  is the Christoffel symbol, which can be computed from the metric  $g_{\alpha\beta}$  and its partial derivatives,

$$\Gamma^\mu_{\alpha\beta} = \frac{1}{2} g^{\mu\nu} (g_{\nu\alpha,\beta} + g_{\nu\beta,\alpha} - g_{\alpha\beta,\nu}). \quad (2.8)$$

As discussed previously in Sec. 2.1, the spacetime metric is commonly evolved as a function of an evolution time coordinate  $t$  instead of the affine parameter  $\lambda$ . It is, therefore, more convenient to rewrite Eq. (2.7) in terms of  $t$ . Defining

$$\dot{x}^\mu = \frac{dx^\mu}{dt} = a \frac{dx^\mu}{d\lambda}, \quad (2.9)$$

where  $a = \frac{d\lambda}{dt}$ , we obtain

$$\frac{dx^\mu}{d\lambda} = \frac{1}{a} \dot{x}^\mu, \quad (2.10a)$$

$$\frac{d^2 x^\mu}{d\lambda^2} = \frac{1}{a^2} \dot{x}^\mu - \frac{\dot{a}}{a^3} \dot{x}^\mu. \quad (2.10b)$$

Substituting these two expressions into Eq. (2.7) gives

$$\ddot{x}^\mu = \frac{\dot{a}}{a} \dot{x}^\mu - \Gamma_{\alpha\beta}^\mu \dot{x}^\alpha \dot{x}^\beta. \quad (2.11)$$

Note that if  $x^0$  is defined to be the time coordinate  $t$ , then  $\dot{x}^\mu \rightarrow (1, \dot{x}^i)$  and  $\ddot{x}^\mu \rightarrow (0, \ddot{x}^i)$ . Inserting these into Eq. (2.11) and solving for the  $\mu = 0$  component gives us the convenient expression:

$$\frac{\dot{a}}{a} = \Gamma_{\alpha\beta}^0 \dot{x}^\alpha \dot{x}^\beta. \quad (2.12)$$

Therefore, the null geodesic equation (Eq. (2.7)) can be recasted in terms of the more convenient evolution time coordinate  $t$  whose spatial components are

$$\ddot{x}^i = \left( \Gamma_{\alpha\beta}^0 \dot{x}^i - \Gamma_{\alpha\beta}^i \right) \dot{x}^\alpha \dot{x}^\beta. \quad (2.13)$$

(The evolution equation for the 0-th component is, of course, trivial:  $\dot{x}^0 = \dot{t} = 1$ ).

It is even more convenient to cast Eq. (2.13) into a system of first-order differential equations to facilitate the use of ODE integrators such as Runge-Kutta. By defining the four-momentum  $p^\mu = \frac{dx^\mu}{d\lambda} = p^0 \dot{x}^\mu$ ,

$$\frac{dx^i}{dt} = \frac{p^i}{p^0}, \quad (2.14a)$$

$$\frac{dp^i}{dt} = \left( \Gamma_{\alpha\beta}^0 p^i - \Gamma_{\alpha\beta}^i \right) \frac{p^\alpha p^\beta}{p^0}. \quad (2.14b)$$

The value of  $p^0 = \frac{dt}{d\lambda}$  can be calculated by simply enforcing that the four-momentum of a photon is null.

However, this naïve formulation has been shown to be susceptible to large growth of numerical errors that arise particularly from calculating the Christoffel symbols. It is almost always necessary to interpolate the values of the metric and its derivatives to the spacetime location of the photons—resulting in some numerical error [16]. The formulation described by Eq. (2.14) uses many metric terms in calculating the Christoffel symbols. Explicitly,

$$\begin{aligned}
\Gamma_{00}^0 &= \frac{1}{\alpha} \left( \alpha_{,t} + \beta^k \alpha_{,k} - K_{ij} \beta^i \beta^j \right), \\
\Gamma_{00}^k &= \gamma^{kj} \left[ \beta_{j,t} + \alpha \alpha_{,j} - \frac{1}{2} (\gamma_{mn} \beta^m \beta^n)_{,j} \right] - \beta^k \Gamma_{00}^0, \\
\Gamma_{i0}^0 &= \frac{1}{\alpha} \left( \alpha_{,i} - K_{ij} \beta^j \right), \\
\Gamma_{i0}^k &= -\alpha K_i^k + {}^{(3)}\nabla_i \beta^k - \Gamma_{i0}^0 \beta^k, \\
\Gamma_{ij}^0 &= -\frac{1}{\alpha} K_{ij}, \\
\Gamma_{ij}^k &= {}^{(3)}\Gamma_{ij}^k - \Gamma_{ij}^0 \beta^k,
\end{aligned} \tag{2.15}$$

where  ${}^{(3)}\nabla$  refers to covariant derivative using the spatial metric and

$${}^{(3)}\Gamma_{ij}^k = \frac{1}{2} \gamma^{kl} (\gamma_{li,j} + \gamma_{lj,i} - \gamma_{ij,l}). \tag{2.16}$$

An alternative formulation with fewer metric terms and their derivatives can be obtained if we evolve  $p_i = g_{i\alpha} p^\alpha$  instead of  $p^i$  [17]. To obtain this

formulation, one can express

$$\frac{dp^i}{dt} = \frac{d(g^{i\alpha}p_\alpha)}{dt} = \frac{d}{dt} \left( \gamma^{ij}p_j - \frac{\beta^i}{\alpha} \sqrt{\gamma^{ij}p_ip_j} \right), \quad (2.17)$$

and solving for  $\frac{dp_i}{dt}$ . In obtaining, Eq. (2.17) we made use of the relation:

$$p^0 = \frac{1}{\alpha} \sqrt{\gamma^{ij}p_ip_j}, \quad (2.18)$$

which is found by enforcing that the four-momentum of a photon is null, i.e.  $\mathbf{p} \cdot \mathbf{p} = 0$ . The alternative formulation is therefore

$$\frac{dx^i}{dt} = \gamma^{ij} \frac{p_j}{p^0} - \beta^i, \quad (2.19a)$$

$$\begin{aligned} \frac{dp_i}{dt} &= -\alpha \alpha_{,i} p^0 + \beta^k_{,i} p_k - \frac{1}{2} \gamma^{jk}_{,i} \frac{p_j p_k}{p^0} \\ &= -\frac{\partial}{\partial x^i} \left( -\beta^k p_k - \alpha \sqrt{\gamma^{jk} p_j p_k} \right) \end{aligned} \quad (2.19b)$$

This simpler formulation of the null geodesic equation was first presented by Hughes *et al.* in Ref. [17]. Notice that not only is this formulation require fewer metric components than the one described by Eq. (2.14), but it also does not require the time derivative of any metric component—making it a prime candidate for null geodesic integration.

However, the value of  $p^0$  blows up as one integrates Eq. (2.19) near the event horizon of a black hole. As a consequence, when using an adaptive time step integrator, the evolution of a null geodesic near a black hole is



considerably slower compared to geodesics located far from any black hole. In some cases, the blowing up of  $p^0$  can also cause the numerical simulation to crash when the geodesic is near the horizon. For example, integrating Eq. (2.19) backward in time in the conventional Schwarzschild coordinates, where  $\alpha = \sqrt{1 - 2M/r}$ , causes the value of  $\alpha$  to approach zero as  $r \rightarrow 2M$ . Consequently,  $p^0 = \sqrt{\gamma^{ij}p_i p_j}/\alpha \rightarrow \infty$  as  $r \rightarrow 2M$ . We have also found empirically that  $p^0$  approaches infinity near a black hole's event horizon when evolved in Kerr-Schild coordinates, as well as in binary black holes cases. Note that Eq. (2.14) is also plagued by the same problem, but can be easily fixed by letting  $p^i = \dot{x}^i$ , instead of  $p^i = \frac{dx^i}{d\lambda}$ .

One possible solution is to normalize the momentum equation such that  $p^0$  is absorbed into the variable being evolved. We choose to evolve  $\Pi_i = p_i/(\alpha p^0)$  where the lapse function is included in order to reduce the number of terms in the equation. The new evolution equations are

$$\frac{dx^i}{dt} = \alpha \Pi^i - \beta^i, \quad (2.20a)$$

$$\frac{d\Pi_i}{dt} = -\alpha_{,i} + \alpha_{,j}\Pi^j\Pi_i - \alpha K_{jk}\Pi^j\Pi^k\Pi_i + \beta^k_{,i}\Pi_k - \frac{\alpha}{2}\gamma^{jk}_{,i}\Pi_j\Pi_k. \quad (2.20b)$$

The formulation described by Eq. (2.20) is a compromise: while it does have more metric terms than the formulation in Eq. (2.19) along with a term (the extrinsic curvature  $K_{jk}$ ) involving the time derivative of the 3-metric, the absence of  $p^0$  ensures that the evolution remains consistent either near to or far from the black hole horizon.

## 2.3 THE EIKONAL EQUATION

An alternative approach to following the trails of light is to consider a surface  $S$  of all photons, instead of the worldline of individual photons. To begin, consider the Euler-Lagrange equation

$$\frac{d}{d\lambda} \left( \frac{\partial L}{\partial x'^{\alpha}} \right) - \frac{\partial L}{\partial x^{\alpha}} = 0, \quad (2.21)$$

where  $\lambda$  is, again, an affine parameter and  $x'^{\alpha} = \frac{dx^{\alpha}}{d\lambda}$ . Since the Lagrangian of a null geodesic motion,

$$L = \frac{1}{2} g_{\alpha\beta} x'^{\alpha} x'^{\beta} = 0, \quad (2.22)$$

has only kinetic terms, it is equal to the Hamiltonian—obtained using the Legendre transformation,

$$H = \frac{1}{2} g^{\alpha\beta} p_{\alpha} p_{\beta} = L = 0. \quad (2.23)$$

Therefore, the Hamiltonian for a null geodesic motion is just the requirement that the four-momentum of the photon must be null, i.e.  $\mathbf{p} \cdot \mathbf{p} = 0$ .

Every photon that makes up the null surface must follow Hamiltonian above. The equation that describes the evolution of a null surface, therefore, can be obtained by making simple direct substitutions  $p_t \rightarrow S_{,t}$  and  $p_i \rightarrow S_{,i}$ .

In particular, from Eq. (2.23),

$$g^{\alpha\beta} S_{,\alpha} S_{,\beta} = 0, \quad (2.24)$$

which can be solved for  $S_{,t}$ . The equation implies that the normal vector  $S_{,\alpha}$  of the null surface  $S$  must also be null. Using the 3+1 ADM variables, we obtain the following symmetric hyperbolic partial differential equation:

$$S_{,t} = \beta^i S_{,i} \pm \alpha \sqrt{\gamma^{ij} S_{,i} S_{,j}} = -\bar{H}, \quad (2.25)$$

which is the eikonal equation. The bar is used to distinguish the Hamiltonian used here from the Hamiltonian in Eq. (2.23).

Notice that  $\bar{H}$  is homogeneous of degree one in  $S_{,i}$ . The characteristic curves along which the level sets of  $S$  are propagated are therefore

$$\frac{dx^i}{dt} = -\beta^i \mp \alpha \frac{\gamma^{ij} p_j}{\sqrt{\gamma^{kl} p_k p_l}} = \frac{\partial \bar{H}}{\partial S_{,i}} \quad (2.26a)$$

$$\frac{dS_{,i}}{dt} = -\frac{\partial}{\partial x^i} \left( -\beta^k S_{,k} \mp \alpha \sqrt{\gamma^{jk} S_{,j} S_{,k}} \right) = -\frac{\partial \bar{H}}{\partial x^i}, \quad (2.26b)$$

which are identical to the null geodesic equations in Eq. (2.19), except for a choice of the sign of the root. The  $\mp$  is included to accommodate both ingoing and outgoing null surfaces, with the minus sign being the appropriate outgoing null surfaces if  $S_{,i}$  is outward pointing. In general, the propagation of the surface  $S$  describes the propagation of either ingoing or outgoing null

surfaces depending on:

1. the definition of the direction of time: forward or backward,
2. the choice of the sign of  $\alpha$  and  $\beta^i$ , and
3. the choice of the sign of the root.

In other words, a minus sign for the root is the appropriate choice for the propagation of the outgoing null surface backwards in time with positive  $\alpha$  and  $\beta^i$ . The eikonal equation, although identical to Eq. (2.19), does not encounter the problem of  $p^0$  blowing up near the event horizon of a black hole because it does not evolve the explicit position of the null geodesics.

A useful property of the solutions to the eikonal equation is that they fall into topologically equivalent classes. This means that any smooth function  $\psi(S)$ —topologically equivalent to  $S$ —is also a solution. Note that:

$$\psi_\alpha(S) = \frac{\partial \psi}{\partial S} \frac{\partial S}{\partial x^\alpha} = \lambda(S) S_{,\alpha}, \quad (2.27)$$

which is true because Eq. (2.25) is homogeneous of degree one in momentum. The above result guarantees that smoothly related initial surface  $S_0 = S(t = t_0, x^i)$  will generate smoothly related solutions.

The rest of the thesis will concentrate on the applications of the two different methods of tracking the paths of photons, the null geodesic equations and the eikonal equation. We will see how each method is more naturally appropriate for certain problems.

# 3

## Gravitational Lensing

### 3.1 BACKGROUND AND MOTIVATION

One of the most promising sources of gravitational waves for potential detection by the Laser Interferometer Gravitational Wave Observatory (LIGO) is the inspiral and merger of binary black holes. To predict the gravitational waveforms that LIGO should expect, the Einstein's field equations for a number of such binary black hole systems with varying mass ratios and spins have been numerically solved.

An interesting, novel way to investigate the structure of the spacetime curvature produced by these binary black holes is to directly visualize the two black holes. Because general relativity predicts that a strong gravitational field—such as the ones produced by black holes—can bend the paths of light rays, the black holes will in fact look distorted. To produce such images, one must then follow the paths of photons<sup>1</sup> through regions of strong gravita-

---

<sup>1</sup>The photon is the name given to a quanta of light which is indeed a measured particle by astronomical observations. However, our discussion is entirely classical and does not require a quantum theory of light as our goal is to understand the path classical light takes when in highly curved spacetime. We, nevertheless, shall borrow this terminology in our

tional field produced by the black holes.

Now, consider an observer taking a picture of the black holes and the night sky using a pinhole camera, as sketched by Fig. 3.1. The image seen by the observer holding the pinhole camera can then be found by tracing the paths of photons *backwards* in time from the observer through each pixel on the pinhole camera image screen. Some of these photons may trace back to the black holes' horizons. In which case the observer would see these pixels as black, since no light would have been emitted from the black hole horizon. In addition, some of the photons may also trace back to the background night sky, and these would be the parts of the night sky seen by the observer. Interestingly, because the gravitational field produced by black holes is extremely strong, some of the photons that the pinhole camera picks up may have originated from behind the observer.

To approach this problem, we will trace the path of each photon through a numerically-solved binary black hole spacetime. Although similar work making use of analytical expressions has already been done [18, 19, 20], what makes our approach novel is that the numerically-solved binary black hole spacetimes are dynamical. A recent numerical work using a similar idea to visualize a collapsing neutron star is presented in Ref. [21]. The work presented in this chapter was done in co-operation with the Caltech-Cornell Simulating eXtreme Spacetime (SXS) Collaboration and was funded by the LIGO Summer Undergraduate Research Fellowship (SURF).

---

discussion by imagining a photon as a particle taking the path that a classical light ray would trace.

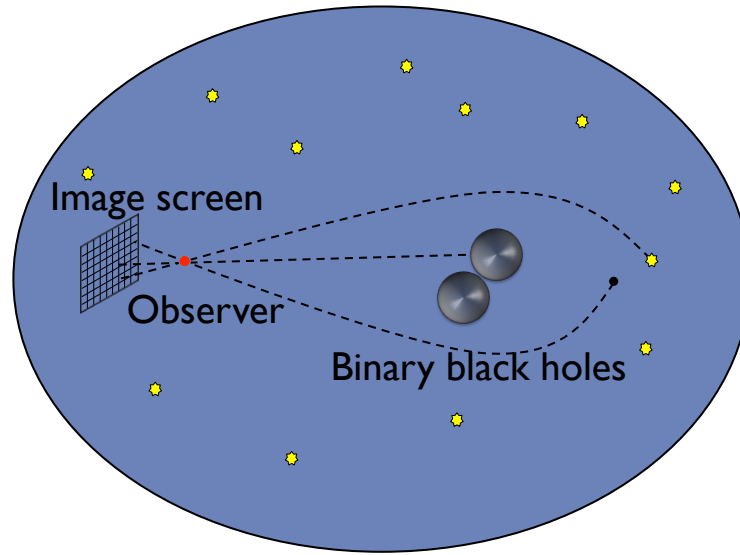


**Figure 3.1:** A schematic of tracking the paths of photons backwards in time from the observer to their supposed origin. The paths of the photons are bent because of the strong gravitational field produced by the black holes.

### 3.2 IMPLEMENTATION

The path of each photon is found by integrating the null geodesic equation backwards in time: from the observer back to the “source”. The uniqueness of the path of every single photon arriving at the observer allows us to do so. The null geodesic equation, which is a system of non-linear ordinary differential equations (ODEs), is integrated using the Dormand-Prince method, a member of the Runge-Kutta family. The method solves the system of ODEs by calculating the fourth and fifth order solutions using six functions; taking the difference between the two solutions as an error estimate; and if the error estimate is not within tolerance that we specify, it tries again with a re-

duced time step size until an acceptable error estimate is obtained. Because there exists huge variations in the strength of the gravitational field—and hence the values of the metric—in our computational domain, such adaptive time step integrator saves computational time by only taking small steps in regions of strong gravitational field near a black hole’s horizon.

We shall use either the normalized form of the null geodesic equation (Eq. (2.20)) because it avoids the problem of slowing down exponentially near a black hole when an adaptive time step integrator is used. For a more complete discussion between the different forms of null geodesic equation, please refer to Sec. 2.2.

### 3.2.1 INITIAL CONDITIONS

Since the null geodesic equation is a system of two first-order non-linear ordinary differential equations, two initial conditions—namely the photons’ final momenta and positions—are necessary to obtain a unique solution to the system of equations. (The initial conditions are the final momenta and positions because the photons are evolved backwards in time.)

The final positions of the photons are simply the camera’s position, because all the photons have to reach the camera simultaneously to form an image. The final momentum of each photon however is different from one another and is dependent on which pixel the photon has traveled to. Each pixel is colored by the color of the photon which has traveled to the center of the pixel. For example, if the photon has originated from a red star in the



background, then the pixel is colored red. To calculate the final momentum for a photon, we need to specify four different vectors:

1.  $\mathbf{e}_0$  which is a unit vector in the direction of time. Usually,  $\mathbf{e}_0 = \mathbf{U}$ , which is the four-velocity of the camera.
2.  $\mathbf{e}_1$  which is a unit vector in the direction where the camera is pointing.
3.  $\mathbf{e}_2$  which is a unit vector in the upwards direction of the camera.
4.  $\mathbf{e}_3 = \mathbf{e}_1 \times \mathbf{e}_2$  which is a unit vector in the rightwards direction of the camera.

Fig. 3.2 shows the orientation of the spatial vectors— $\mathbf{e}_1, \mathbf{e}_2, \mathbf{e}_3$ —with respect to the pinhole camera.

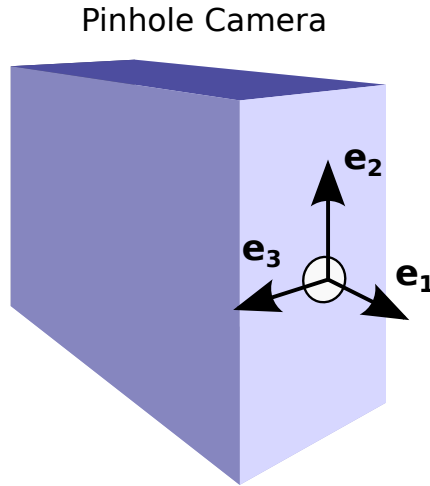


**Figure 3.2:** Schematic of the spatial orthonormal vectors in relation to the pinhole camera.

If the camera is not moving with respect to the computational frame, then  $\mathbf{e}_0 = (1, 0, 0, 0)$ ,  $\mathbf{e}_1 = (0, 1, 0, 0)$ , and so on. We call this computational frame, the *inertial frame*, because its spatial geometry asymptotically approaches Euclidian at spatial infinity (far from any black hole). The spacetime metric components for the code also happen to be expressed in this frame. If, however, the camera has some velocity with respect to the inertial frame, we can ensure that all the vectors are orthogonal to each other by means of successive Gram-Schmidt processes. We shall discuss these Gram-Schmidt processes below.

Let us start by defining  $v^i = \frac{dx^i}{dt}$  to be the three-velocity of the camera with respect to the inertial frame. The four-velocity of the camera  $U^\alpha = \frac{dx^\alpha}{d\tau}$  can be found by

$$\mathbf{U} \cdot \mathbf{U} = g_{\alpha\beta} U^\alpha U^\beta = \left( U^0 \right)^2 \left( g_{\alpha\beta} v^\alpha v^\beta \right) = -1, \quad (3.1)$$

where  $U^0 = \frac{dt}{d\tau}$  relates the time coordinate  $t$  in the inertial frame and the proper time  $\tau$  of the camera. The zeroth component of the vector  $v^\alpha$  is just  $v^0 = \frac{dt}{dt} = 1$ .

Let us then consider where the camera is pointing at. The camera direction is also the direction of three-momentum  $\pi^i$  of the photon going through the center pixel. We specify the value of  $\pi^i$  in the inertial frame. The four-momentum  $\pi^\alpha$  of the photon can then be simply determined by ensuring that the four-momentum is null, i.e.  $\pi \cdot \pi = 0$ .

We also define  $\xi^i$  as the direction in which the upwards direction is point-

ing at in the inertial frame. The zeroth component of this vector,  $\xi^0 = 0$  in the inertial frame.

From the three vectors that we have specified in the inertial frame:

1.  $U^\alpha$  which is the four-velocity of the camera,
2.  $\pi^\alpha$  which is the four-momentum of the photon that goes through the center pixel, and
3.  $\xi^\alpha$  which is the upwards direction of the camera,

we can proceed to calculate the photons' final momenta.

First we construct the vector  $r^\alpha$  using a Gram-Schmidt process:

$$r^\alpha = \pi^\alpha + (\pi \cdot \mathbf{U}) U^\alpha. \quad (3.2)$$

Notice that  $\mathbf{r} \cdot \mathbf{U} = 0$ , which means that the vector  $r^\alpha$  is a purely spatial vector in the camera's instantaneously co-moving inertial reference frame (CMRF), because  $U^\alpha \rightarrow (1, 0, 0, 0)$  in this frame.  $r^\alpha$  is then the proper direction that the camera is pointing at in the CMRF.

We then also construct  $\zeta^\alpha$ —the upwards direction of the camera in the CMRF—by a similar Gram-Schmidt process:

$$\bar{\zeta}^\alpha = \xi^\alpha + (\xi \cdot \mathbf{U}) U^\alpha, \quad (3.3)$$

and

$$\zeta^\alpha = \bar{\zeta}^\alpha - (\bar{\zeta} \cdot \hat{\mathbf{r}}) \hat{r}^\alpha, \quad (3.4)$$

where  $\hat{\mathbf{r}} = \mathbf{r}/\sqrt{\mathbf{r} \cdot \mathbf{r}}$  is the normalized vector  $\mathbf{r}$ . The above two relations ensure that  $\zeta \cdot \mathbf{U} = 0$  and  $\zeta \cdot \mathbf{r} = 0$ . Similarly, the vector  $\zeta$  can be normalized to  $\hat{\zeta} = \zeta/\sqrt{\zeta \cdot \zeta}$ .

Notice that with  $U^\alpha$ ,  $r^\alpha$ , and  $\zeta^\alpha$ , we can form an orthonormal tetrad:<sup>2</sup>

$$\begin{aligned} \mathbf{e}_0^\alpha &= U^\alpha, \\ \mathbf{e}_1^\alpha &= \hat{r}^\alpha, \\ \mathbf{e}_2^\alpha &= \hat{\zeta}^\alpha, \\ \mathbf{e}_3^\alpha &= (\mathbf{e}_1 \times \mathbf{e}_2)^\alpha = \varepsilon_{\beta\gamma\delta}^\alpha U^\beta \hat{r}^\gamma \hat{\zeta}^\delta. \end{aligned} \tag{3.5}$$

The orthonormal tetrad gives the four spacetime directions in the camera's CMRF, i.e.  $\mathbf{e}_0^\alpha \rightarrow (1, 0, 0, 0)$ ,  $\mathbf{e}_1^\alpha \rightarrow (0, 1, 0, 0)$ , and so on. It is therefore convenient to calculate the final momentum of the photon that passes through the pixel  $\{a, b\}$  using the orthonormal tetrad construction,

$$p_{(a)(b)}^\alpha = c \mathbf{e}_0^\alpha + \mathbf{e}_1^\alpha - \left(b - \frac{1}{2}\right) \mathbf{e}_2^\alpha + \left(a - \frac{1}{2}\right) \mathbf{e}_3^\alpha, \tag{3.6}$$

where  $a, b \in [0, 1]$  give the pixel location in terms of fraction of the image's horizontal and vertical lengths with  $\{a, b\} = \{0, 0\}$  at the top left corner of the image. Also,  $c = \sqrt{1 + (b - 1/2)^2 + (a - 1/2)^2}$ , which is found by

---

<sup>2</sup>We are using the Levi-Civita tensor convention as defined by Misner *et al.* [14], where  $\varepsilon_{\alpha\beta\gamma\delta} = \sqrt{-g}[\alpha\beta\gamma\delta]$ , and

$$[\alpha\beta\gamma\delta] = \begin{cases} +1 & \text{if } \alpha\beta\gamma\delta \text{ is an even permutation of } 0123, \\ -1 & \text{if } \alpha\beta\gamma\delta \text{ is an odd permutation of } 0123, \\ 0 & \text{if } \alpha\beta\gamma\delta \text{ are not all different.} \end{cases}$$

demanding that the momentum is null.

Notice that when using this method to calculate the photons' final momenta, there is no need to boost any of the vectors from the inertial frame to the camera's CMRF and back. We have simply calculated all the vectors and the photons' momenta in the inertial frame.

### 3.2.2 BACKGROUND IMAGE

For the purpose of determining which part of the resulting image corresponds to which part of the night sky, we choose a grid with a gradient color map as shown in Fig. 3.3. This two-dimensional image represents a cylindrical Plate Carée projection of the observer's celestial sphere [22]. The Plate Carée projection is an equirectangular projection that neither stretches nor compresses the north-south distance. The horizontal position  $x$  and the vertical position  $y$  along the map are related to the longitude  $\phi$  and the latitude  $\theta$  by the following simple relations:

$$\begin{aligned} x &= -\phi, \\ y &= -\theta, \end{aligned} \tag{3.7}$$

where the negative signs are because the observer is viewing this background image from inside the sphere. (Contrast this with cartography where the globe is viewed from outside—not inside.) Therefore, the Plate Carée projection casts the lines of constant latitude to horizontal grid lines (lines of constant  $\theta$  in the spherical coordinate system) and the lines of constant lon-

gitude to vertical grid lines (lines of constant  $\phi$  in the spherical coordinate system).

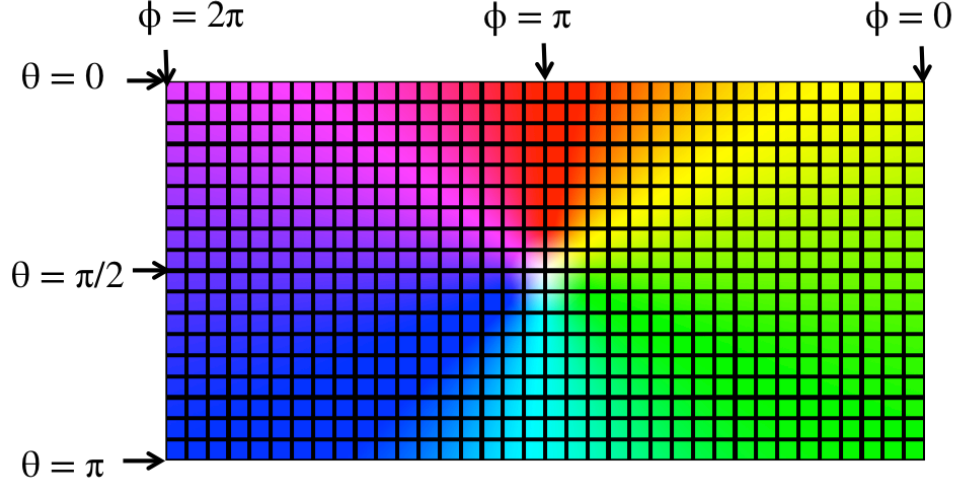


**Figure 3.3:** A grid with the gradient color map. The projected angular positions of some lines are denoted, where  $\theta$  is the latitude and  $\phi$  is the longitude.

### 3.3 SINGLE BLACK HOLE CASES

#### 3.3.1 THE KERR-SCHILD METRIC

In this section, we explore images of the night sky that have been distorted by a single black hole. All the single black hole images in this thesis are made by integrating the normalized form of the null geodesic equation (Eq. (2.20)) with the Kerr spacetime expressed in Kerr-Schild coordinates  $(t, x, y, z)$ . For a Kerr black hole with angular momentum  $aM$  in the  $z$ -direction, the 3+1

decomposition of the spacetime in Kerr-Schild coordinates is <sup>3</sup>

$$\gamma_{ij} = \delta_{ij} + 2Hl_i l_j, \quad (3.10a)$$

$$\alpha = \frac{1}{\sqrt{1 + 2Hl^t l^t}}, \quad (3.10b)$$

$$\beta^i = -\frac{2Hl^t l^i}{1 + 2Hl^t l^t}, \quad (3.10c)$$

$$K_{ij} = -\frac{\sqrt{1 + 2Hl^t l^t} \left[ l_i l_j \partial_t H + 2Hl_{(i} \partial_t l_{j)} \right] + 2 \left[ \partial_{(i} (l_{j)} H l^t) + 2H^2 l^t l^k l_{(i} \partial_{|k|} l_{j)} + H l^t l_i l_j l^k \partial_k H \right]}{\sqrt{1 + 2Hl^t l^t}}, \quad (3.10d)$$

where  $H$  and  $l_\alpha$  are given in terms of the black hole's mass  $M$  and angular momentum  $aM$  by

$$H = \frac{Mr_{BL}^3}{r_{BL}^4 + a^2 z^2}, \quad (3.11)$$

and

$$l_\alpha \rightarrow \left( 1, \frac{x r_{BL} + a y}{r_{BL}^2 + a^2}, \frac{y r_{BL} - a x}{r_{BL}^2 + a^2}, \frac{z}{r_{BL}} \right). \quad (3.12)$$

The quantity  $r_{BL}$  is the Boyer-Lindquist coordinate which can be found by solving

$$r_{BL}^4 - (x^2 + y^2 + z^2 - a^2) r_{BL}^2 - a^2 z^2 = 0. \quad (3.13)$$

---

<sup>3</sup>The braces in the tensor indices indicate symmetrization. Generally, for a tensor  $T_{a_1 \dots a_n}$  of type  $(0, n)$ ,

$$T_{(a_1 \dots a_n)} = \frac{1}{n!} \sum_{\pi} T_{a_{\pi(1)} \dots a_{\pi(n)}}. \quad (3.8)$$

For example,

$$T_{(ij)} = \frac{1}{2!} (T_{ij} + T_{ji}); \quad T_{(abc)} = \frac{1}{3!} (T_{abc} + T_{acb} + T_{bac} + T_{cab} + T_{bca} + T_{cba}) \quad (3.9)$$

This is in contrast with the Kerr-Schild radial coordinate  $r$  which does not depend on spin,

$$r^2 = x^2 + y^2 + z^2. \quad (3.14)$$

### 3.3.2 COMPARISON AGAINST ANALYTICAL INTEGRATION

Here we shall compare the results of our numerical scheme against those from analytical scheme for a non-spinning Schwarzschild black hole. We place the Schwarzschild black hole at the center of the domain, i.e.  $(x, y, z) \rightarrow (0, 0, 0)$  with mass  $M = 1$ . We also place the observer  $r = 50M$  away from the hole in Kerr-Schild coordinates at the positive  $x$ -axis, i.e.  $(x, y, z) \rightarrow (50, 0, 0)$ , with a camera pointing in the negative  $x$ -axis direction. The upwards direction of the camera is the positive  $z$ -direction. The resulting distorted image, with a resolution of  $300 \times 300$ , is shown in Fig. 3.4.

The small black circle in the middle of the distorted image is the black hole, i.e. the set of photons that end up on the event horizon of the hole when integrated backwards in time from the camera. The large black circular-like grid line is the Einstein ring. The Einstein ring is composed of photons originating from a single point directly behind the black hole (the point at the center of Fig. 3.3) and bent around the black hole to produce a circular image. Interestingly, inside the Einstein ring, the image is not only distorted but also reflected in the sense that photons that have originated from the right is seen by the observer as if they have originated from the left. Similarly, photons that originate from the top is seen by the observer originating



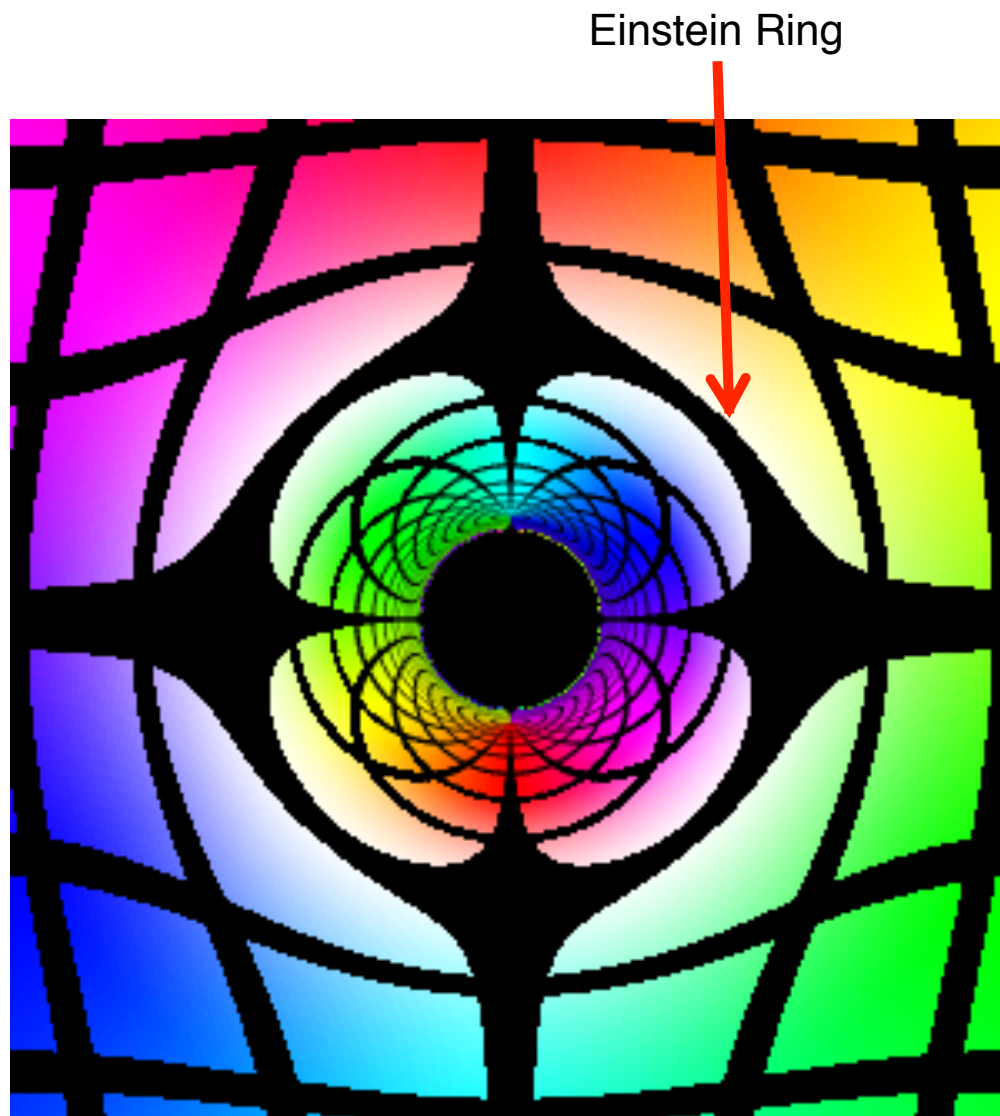


**Figure 3.4:** A gradient color map grid distorted by a non-spinning black hole. The arrow indicates the location of the Einstein ring in the image. The resolution of the pinhole camera is 300 x 300 in this case.

from the bottom. Outside the Einstein ring, no such reflection is apparent although the grid lines are distorted.

As a check of the integrity of our result, we shall compare the geodesic trajectory in this Schwarzschild spacetime obtained by numerically integrating the normalized form of the null geodesic equation (Eq. (2.20)) to the trajectory obtained by integrating the analytical expressions. In this Schwarzschild spacetime—when the black hole is not spinning ( $a = 0$ )—the metric is greatly simplified. In Kerr-Schild coordinates,

$$g_{\alpha\beta} = \eta_{\alpha\beta} + 2Hl_{\alpha}l_{\beta}, \quad (3.15)$$

where  $\eta_{\alpha\beta} = \text{diag}(-1, 1, 1, 1)$  is the Minkowski metric,

$$H = \frac{M}{r}, \quad (3.16)$$

since  $r_{BL} = r = \sqrt{x^2 + y^2 + z^2}$  in the non-spinning case, and

$$l_{\alpha} \rightarrow \left(1, \frac{x}{r}, \frac{y}{r}, \frac{z}{r}\right). \quad (3.17)$$

The 3+1 decomposition of this spacetime is

$$\alpha = \frac{1}{\sqrt{1 + 2M/r}}, \quad (3.18a)$$

$$\beta^i = -\frac{2M/r}{1 + 2M/r} x^i, \quad (3.18b)$$

$$K_{ij} = \frac{2M}{r^4 \sqrt{1 + 2M/r}} \left[ r^2 \delta_{ij} - \left( 2 + \frac{M}{r} \right) x_i x_j \right], \quad (3.18c)$$

where  $x^i \rightarrow (x, y, z)$  is the Kerr-Schild spatial coordinates. We integrate the null geodesic equation using this spacetime metric.

The trajectory obtained using the Schwarzschild metric above will then be compared with the trajectory obtained by integrating the analytical expressions of the equations of motion. We use the results of Ref. [14], where the study of the equations of motion are done in the conventional Schwarzschild coordinates because they are much simpler. Also, without loss of generality we shall only consider photons that are traveling in a polar orbit at the equator ( $\theta = \pi/2$ ), because Schwarzschild spacetime exhibits spherical symmetry.

The equations of motion for a photon traveling in an equatorial orbit ( $\theta = \pi/2$ ), expressed in the conventional Schwarzschild coordinates  $(\bar{t}, r, \theta, \phi)$  is

$$p^{\bar{t}} = \frac{d\bar{t}}{d\lambda} = \frac{1}{b(1 - 2M/r)}, \quad (3.19a)$$

$$p^r = \frac{dr}{d\lambda} = \pm \sqrt{\frac{1}{b^2} - \left(\frac{1 - 2M/r}{r^2}\right)}, \quad (3.19b)$$

$$p^\theta = \frac{d\theta}{d\lambda} = 0, \quad (3.19c)$$

$$p^\phi = \frac{d\phi}{d\lambda} = \frac{1}{r^2}, \quad (3.19d)$$

where  $b = \pm p_\phi / p_{\bar{t}}$  is the impact parameter. These equations of motion casted in Schwarzschild coordinates can be simply related to the spherical Kerr-Schild coordinates  $(t, r, \theta, \phi)$  by

$$d\bar{t} = \pm \left( dt - \frac{2M/r}{1 - 2M/r} dr \right), \quad (3.20)$$

because areal coordinate  $r$  and the angular coordinates  $(\theta, \phi)$  for both Kerr-Schild and Schwarzschild coordinates are identical. The relationship between the Kerr-Schild time and the Schwarzschild time allows us to recast the equations of motion in terms of the Kerr-Schild time instead of the affine parameter  $\lambda$ .

We then proceed by choosing the direction of time in both coordinate to be in the same direction of the affine parameter. This implies the choice of positive signs in the impact parameter  $b$  and in Eq. (3.20). Because we are integrating backwards in time, the choice of sign in  $p^r$  is positive initially when the photon approaches the hole. After the photon has reached its distance of

closest approach, the sign of  $p^r$  will then switch to negative indicating that the photon is traveling away from the hole. This distance of closest approach  $R$  can be found by solving for  $r$  when  $p^r = 0$ , written in implicit form,

$$\frac{R^2}{1 - 2M/R} = b^2. \quad (3.21)$$

Obtaining the analytical expression for  $r(t)$  and  $\phi(t)$  is generally difficult. The alternative is, of course, to integrate the equations of motion using numerical means; and, we shall do so using the Dormand-Prince method.

Figs. 3.5 and 3.6 show the comparison of trajectories of two photons: one that has originated from the night sky and one that has originated from infinitesimally outside the black hole horizon.

In Fig. 3.6, we can see that the error shot up at around  $t \approx -50M$  for the photon that has originated from the night sky. The increase in error was caused by the sign change in  $p^r$  just as the photon reached its distance of closest approach. The change in the sign of  $p^r$  was not made at exactly the right time causing the drastic increase in errors. Nevertheless, the absolute errors are still very small—less than  $\mathcal{O}(10^{-5})$ —despite the large fractional increase in errors. The difference between the two results then plateaus right after this turning point. Considering that both independent results were obtained using numerical integration, the small difference between the two results implies that they agree well with each other.

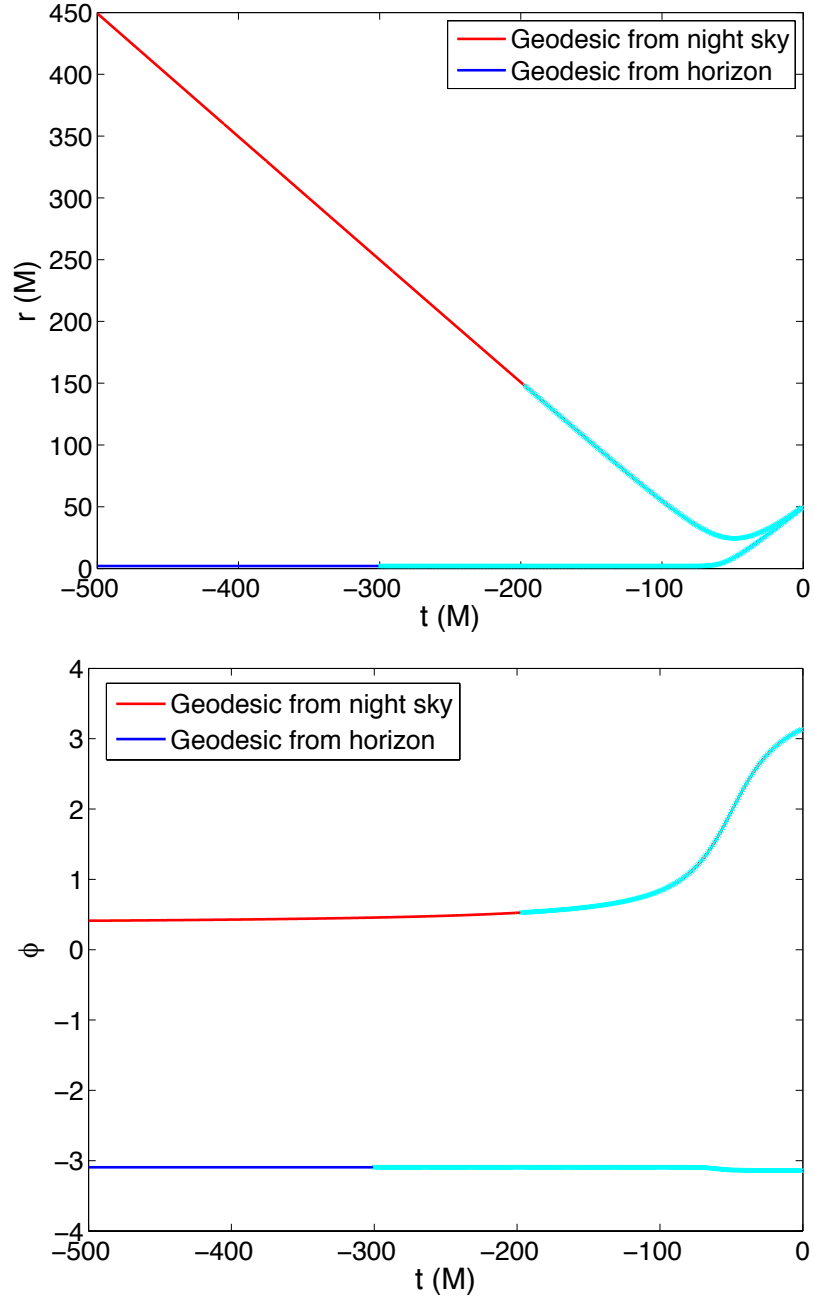


**Figure 3.5:** Plots comparing the trajectories of two photons: one that has originated from the night sky (red) and one that has originated from just outside the black hole (blue). The cyan points are those that are obtained from integrating the normalized form of the null geodesic equation backwards in time, and they are truncated earlier than the lines of trajectories obtained from analytical integration (red and blue).

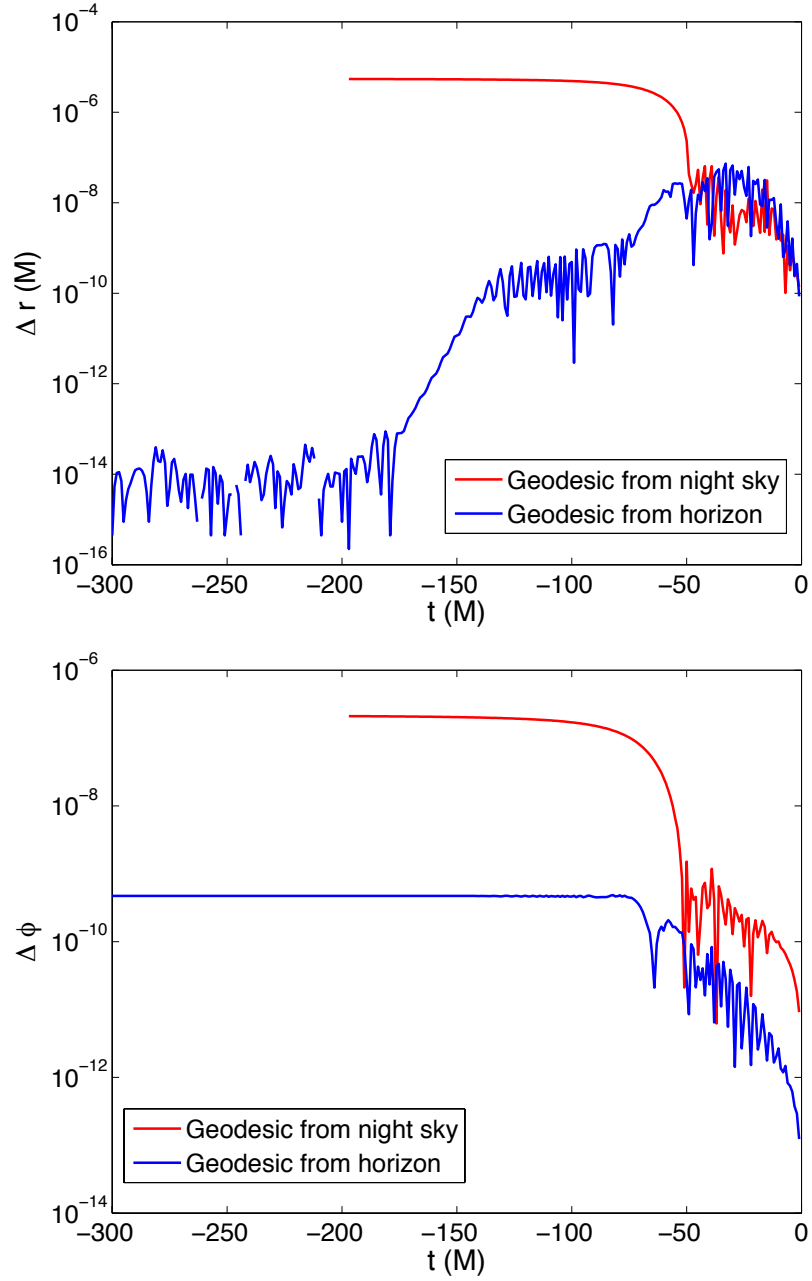


**Figure 3.6:** Plots comparing the difference in trajectories obtained from integrating the null geodesic equation and those obtained from integrating the photons' equations of motion. The photon that has originated from the night sky is red and the photon that has originated from just outside the black hole is blue.

### 3.3.3 RESULTS

Figs. 3.7–3.11 and 3.12–3.16 are side and top-down views of a single black hole with different spins, ranging from zero spin to nearly maximal spin. (The sudden transition between the blue and green color in Figs. 3.12–3.16 is not a physical artifact; it was caused by the way the background image, Fig. 3.3, is projected.) The figures are created by integrating the normalized form of the null geodesic equation (Eq. (2.20)) with Kerr-Schild metric input as described in Sec. 3.3.1, where the spin of the black hole is pointing in the positive  $z$ -direction.

Similar to what we have done to produce Fig. 3.4, we place the hole at the center of the domain and the observer is placed  $50M$  away in Kerr-Schild coordinates. For the side view images, the observer is placed at the positive  $x$ -axis, i.e.  $(x, y, z) \rightarrow (50, 0, 0)$ , and is pointing the pinhole camera in the negative  $x$ -direction. On the other hand, for the top-down view images, the observer is placed in the positive  $z$ -axis, i.e.  $(x, y, z) \rightarrow (0, 0, 50)$ , and is pointing the pinhole camera down in the negative  $z$ -direction.

The effects of rotational frame-dragging (also known as Lense-Thirring effect) due to the spin of the black hole are evident in these figures. In the side view images (Figs. 3.7–3.11), frame-dragging causes the black hole to shift slightly to the right. Inside the Einstein ring, since the spin of the black hole is pointing upwards, the photons that make up the image to the right side of the hole have to travel for a larger amount of affine parameter  $\lambda$  than those that make up the image to the left side of the hole. As a consequence,



the geodesic trajectories for the photons that make up the image to the right side of the hole are bent at larger angles.

Moreover, in the top-down view images (Figs. 3.12–3.16), the rotational frame dragging causes a distortion of the longitudinal lines in the same sense as the spin, which is out of the page. It is also interesting to note the bright red ring just right outside of the hole is produced by photons that have originated from behind the observer because red is the color of the background image at the north pole and cyan is the color of the background image at the south pole.

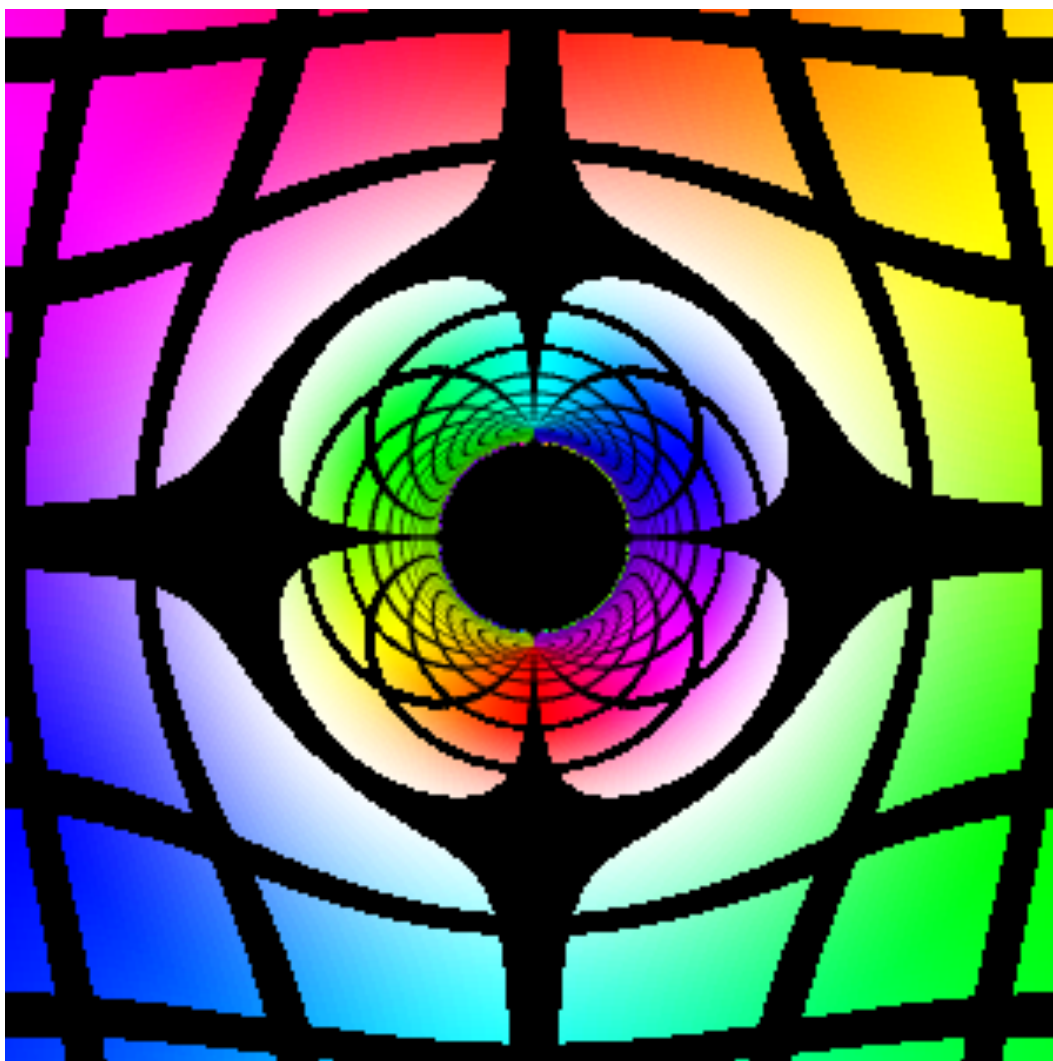


**Figure 3.7:** Side view image of the gradient color map distorted by a single black hole with no spin at camera resolution of 300 x 300.



**Figure 3.8:** Side view image of the gradient color map distorted by a single black hole with a spin of  $0.2510M$  at camera resolution of  $300 \times 300$ .

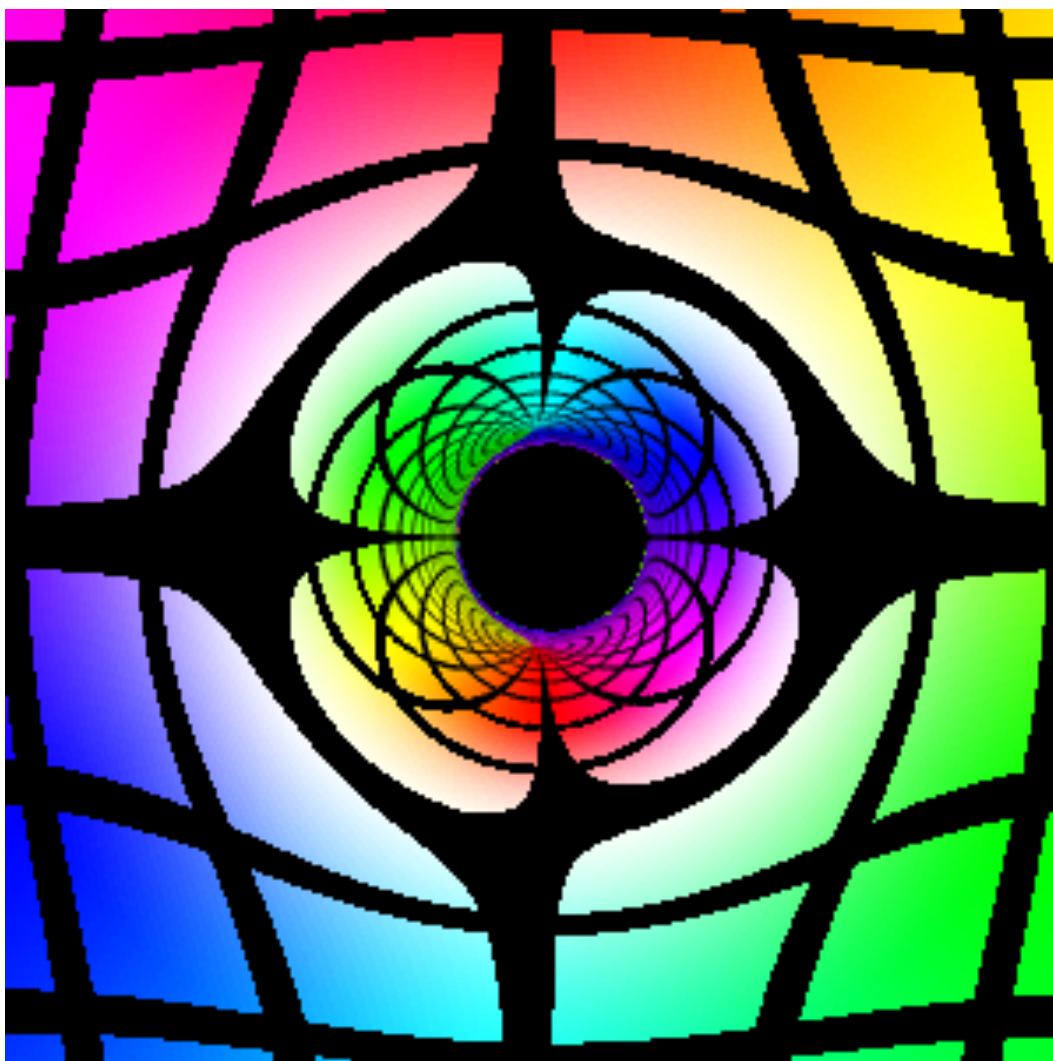


**Figure 3.9:** Side view image of the gradient color map distorted by a single black hole with a spin of  $0.5035M$  at camera resolution of  $300 \times 300$ .

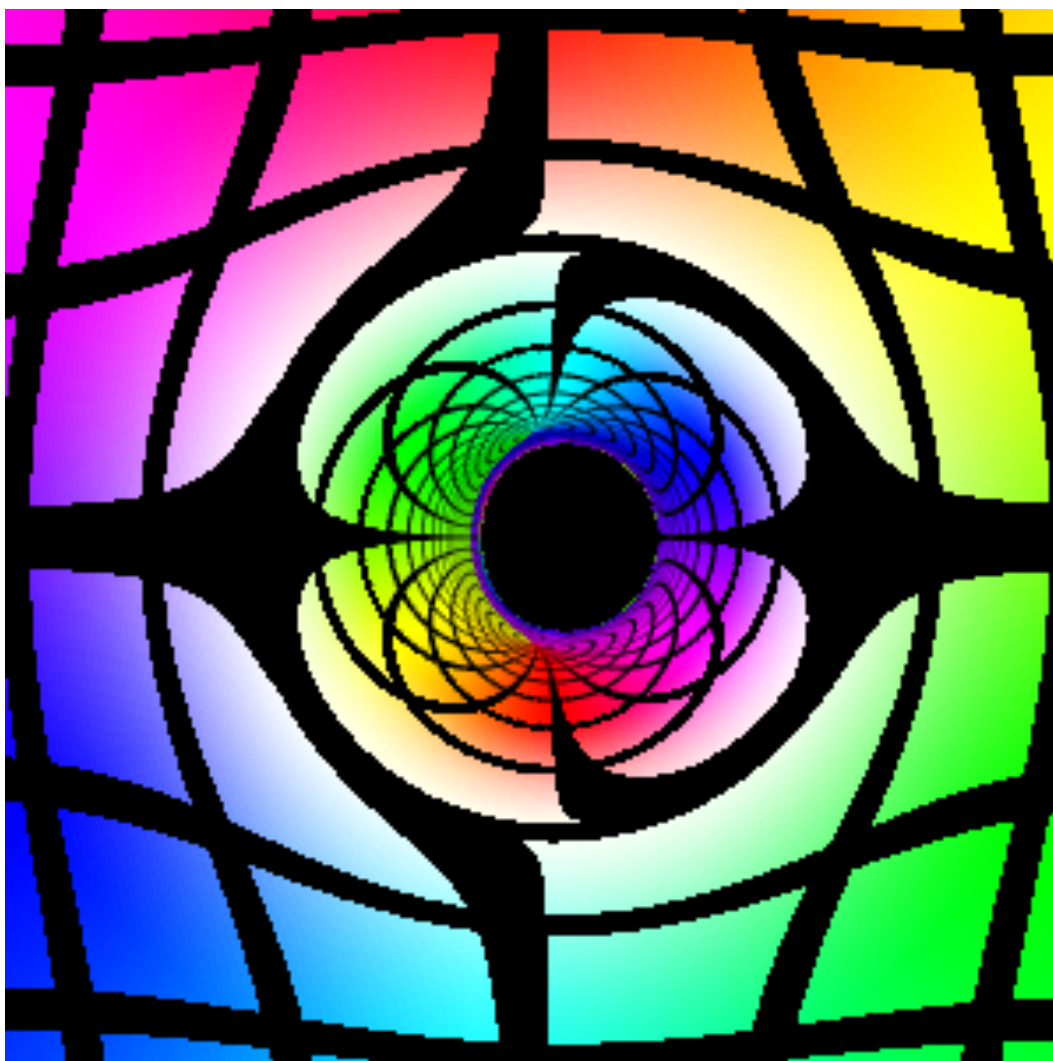


**Figure 3.10:** Side view image of the gradient color map distorted by a single black hole with a spin of  $0.7478 M$  at camera resolution of  $300 \times 300$ .

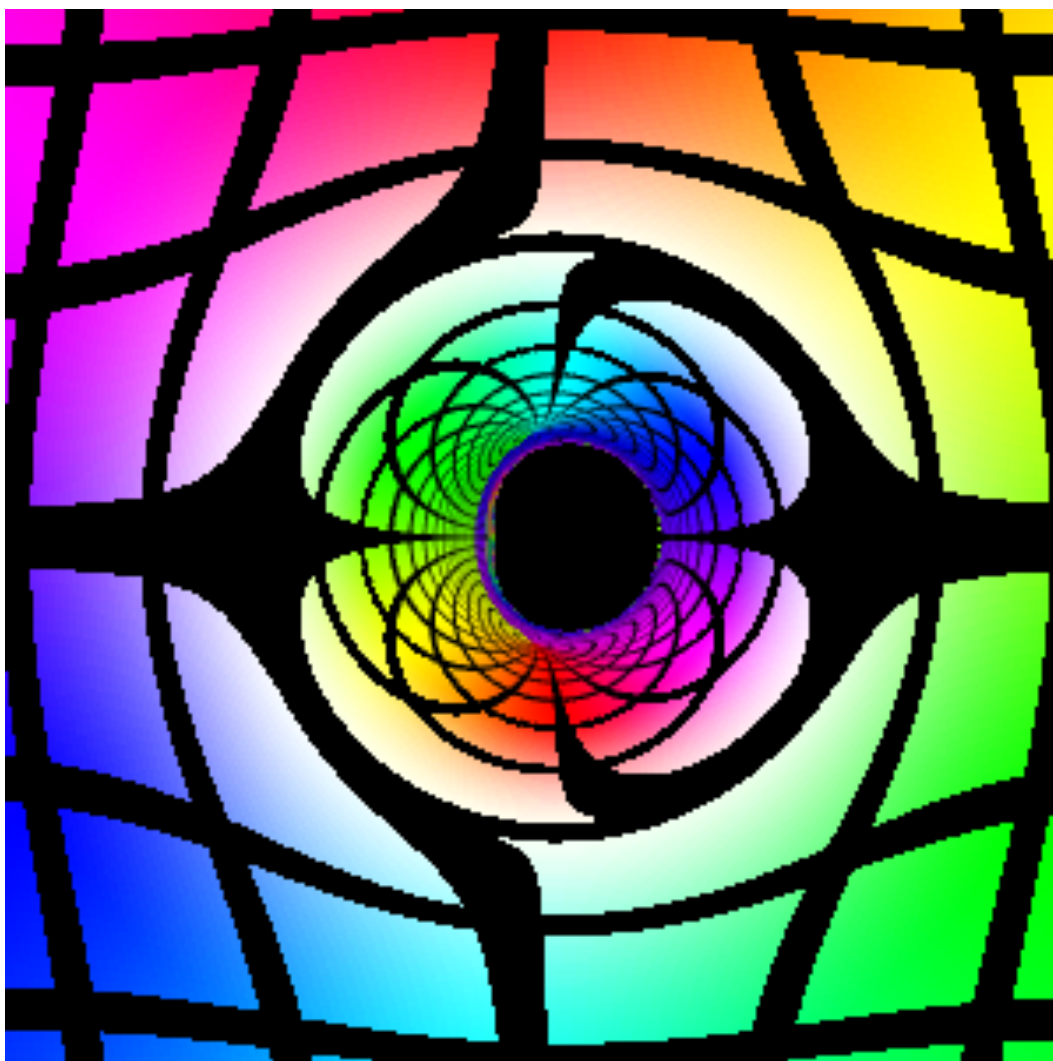


**Figure 3.11:** Side view image of the gradient color map distorted by a single black hole with a spin of  $0.9999M$  (nearly maximal spin) at camera resolution of  $300 \times 300$ .

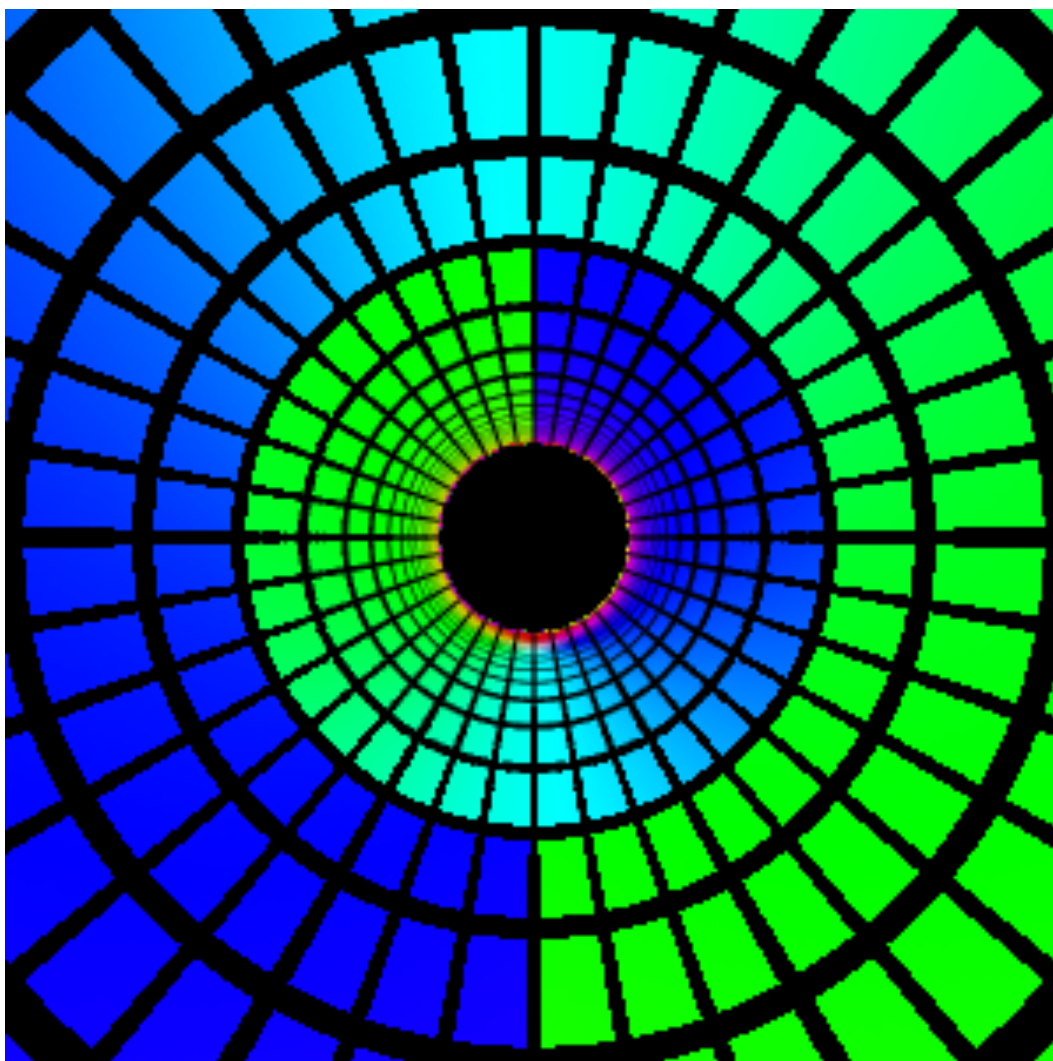


**Figure 3.12:** Top-down view image of the gradient color map distorted by a single black hole with no spin at camera resolution of 300 x 300.

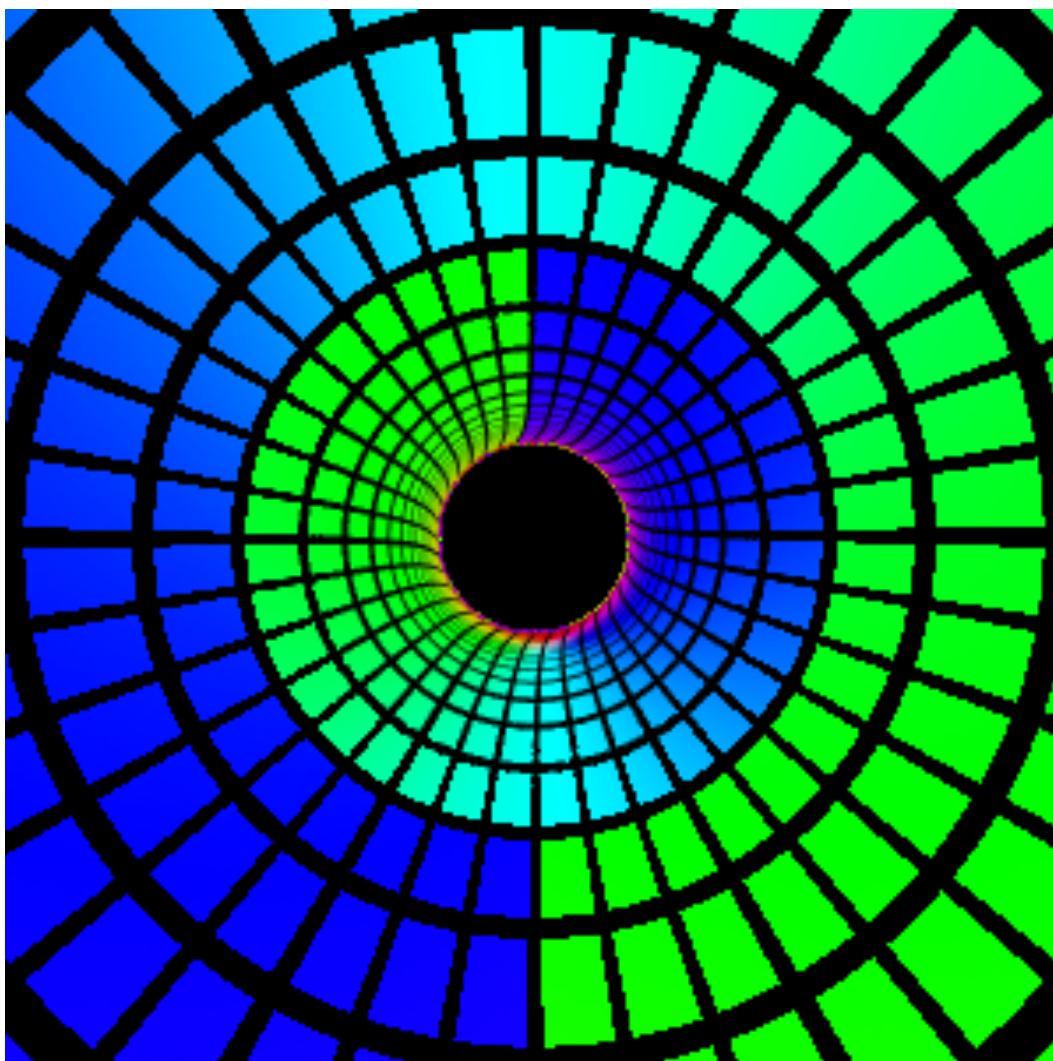


**Figure 3.13:** Top-down view image of the gradient color map distorted by a single black hole with a spin of  $0.2510M$  at camera resolution of  $300 \times 300$ .



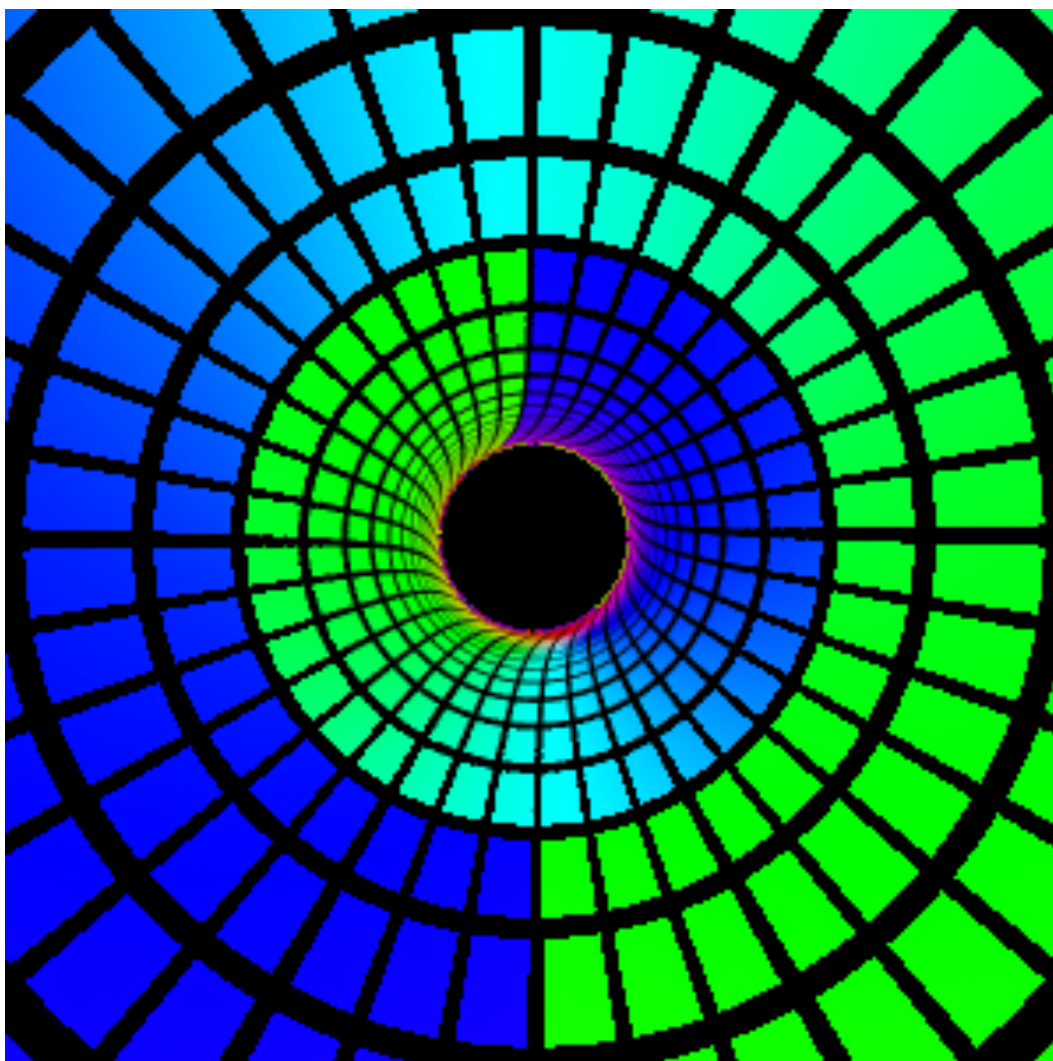


**Figure 3.14:** Top-down view image of the gradient color map distorted by a single black hole with a spin of  $0.5035M$  at camera resolution of  $300 \times 300$ .

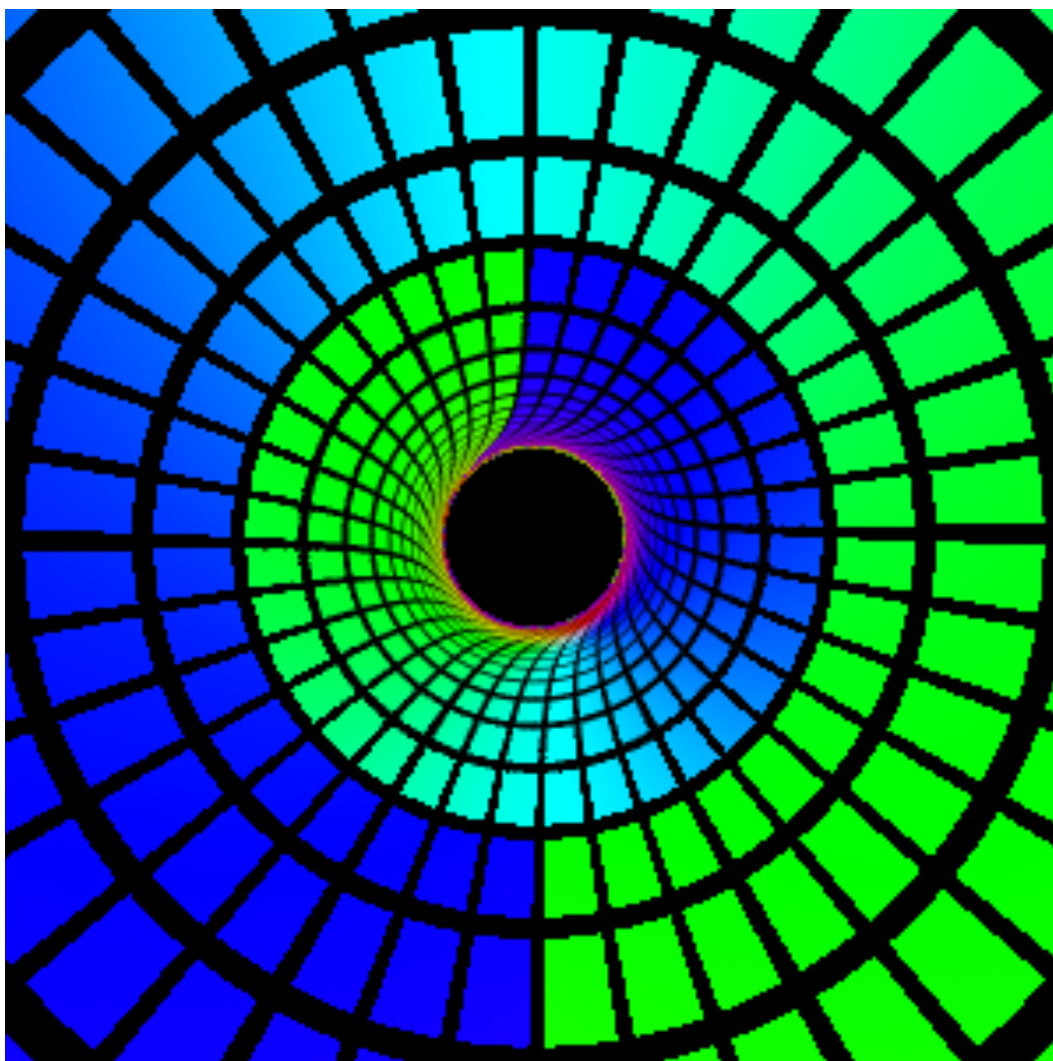


**Figure 3.15:** Top-down view image of the gradient color map distorted by a single black hole with a spin of  $0.7478M$  at camera resolution of  $300 \times 300$ .

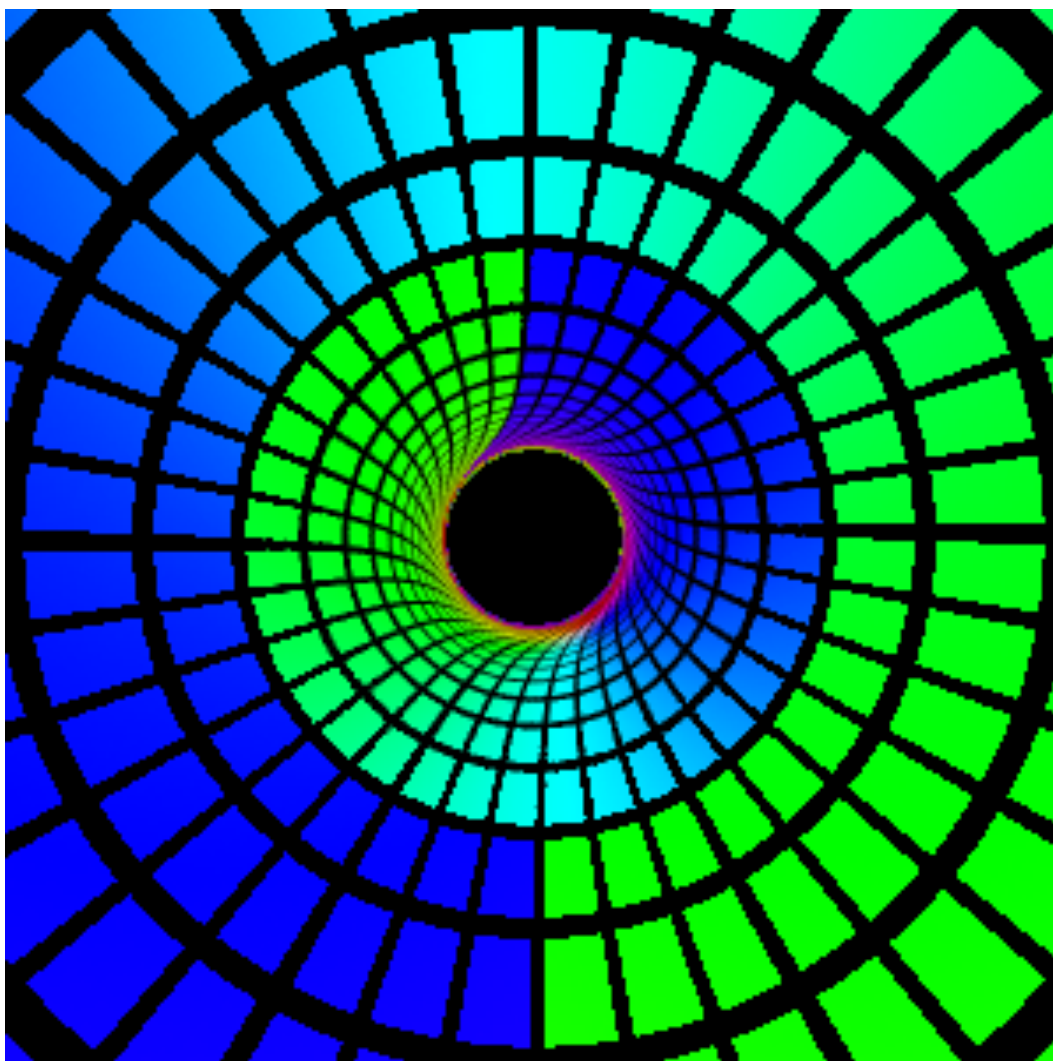


**Figure 3.16:** Top-down view image of the gradient color map distorted by a single black hole with a spin of  $0.9999M$  (nearly extremal spin) at camera resolution of  $300 \times 300$ .

### 3.4 EQUAL MASS BINARY BLACK HOLES

The simulation of binary black hole inspiral and coalescence has been one of the most important achievements of numerical relativity. As of now, there is no analytical expression for the dynamical spacetime produced by a binary black hole merger yet—especially for equal mass binary black holes.

Figs. 3.17–3.22 show the side view images of an equal mass non-spinning binary black hole system from  $t = 3937M$ – $3961M$  separated by  $\Delta t = 4.812M$ . Although each of the black hole is not spinning on its own axis, the system has an orbital angular momentum which is pointing in the positive  $z$ -direction. Similar to the single black hole cases, we place the observer at  $r = 50M$  away from the origin—on the positive  $x$ -axis.  $M$  in the binary black hole case refers to the total mass of the binary black hole system. The pinhole camera is similarly directed in the negative  $x$ -direction with an upwards direction in the positive  $z$ -direction. Although a common horizon between the two black holes—signifying a merger—is found at  $t \approx 3910M$ , the pinhole camera did not yet record any merger approximately  $50M$  after.

The equal mass non-spinning binary black hole system exhibits a few interesting features. First, the Einstein ring is distorted in the same manner as in the case of a Kerr hole with spin pointing in the  $z$ -axis even though none of the two black holes is spinning on its own axis. The distortion must then be caused by the angular momentum of the system that points in the positive  $z$ -direction. Secondly, we observe “eyebrow” features in the outer

region of the black hole that are caused by one black hole being gravitationally lensed by the other black hole. Such eyebrow feature is strongly evident in Fig. 3.17. Lastly, there seems to always be a small slit of separation between the two black holes even when one hole is directly in front of the other (refer to Fig. 3.22). The small slit of separation is produced by geodesics that have traveled between the two black holes.

To understand the eyebrow structure more closely, let us plot the paths of three photons which are observed at  $t = 3937M$ . Fig. 3.23 shows a side view image of the two black holes at this time, which is equivalent to Fig. 3.17, but the approximate locations of the three photons in the image are labeled. Let us name the one outside the Einstein ring photon  $A$ , the one inside the Einstein ring photon  $B$ , and the one inside the slit between the two black holes photon  $C$ .

Fig. 3.24 shows that the trajectory of photon  $A$ , which is the farthest away from the black holes among the three, does not show much deviation from a straight line. On the other hand, the trajectory of photon  $B$ , which creates an image inside the Einstein ring, is bent at larger angles than photon  $A$ . As a result, while the photon has originated on the left-hand side of the binary black holes, the observer sees it on the right hand side (see Figs. 3.17–3.22). Photon  $C$  travels close to the binary black holes. At  $t \approx 3870M$ , the photon travels in between of the two black holes—making up the slit in between the black holes. Being close to the horizon of the red black hole, photon  $C$  is bent at an even larger angle than that of photon  $B$ . Photon  $C$  eventually escapes

to make up the green color slit seen in Fig. 3.23.

In addition to the side view images, Fig. 3.25 shows a top-down view of the binary black hole system at an earlier time of  $t = 3167M$ . The observer is again placed  $50M$  away on the positive  $z$ -axis. The pinhole camera is pointed to the negative  $z$ -direction. At this time, merger between the two holes are yet to occur, the Einstein rings of the two black holes interestingly form a single oval Einstein ring. In addition, even though the black holes are orbiting each other with an orbital angular momentum pointing out of the page, we do not clearly see a significant tangential twisting of the lines inside the Einstein ring—unlike what happens in the case of spinning Kerr black holes.

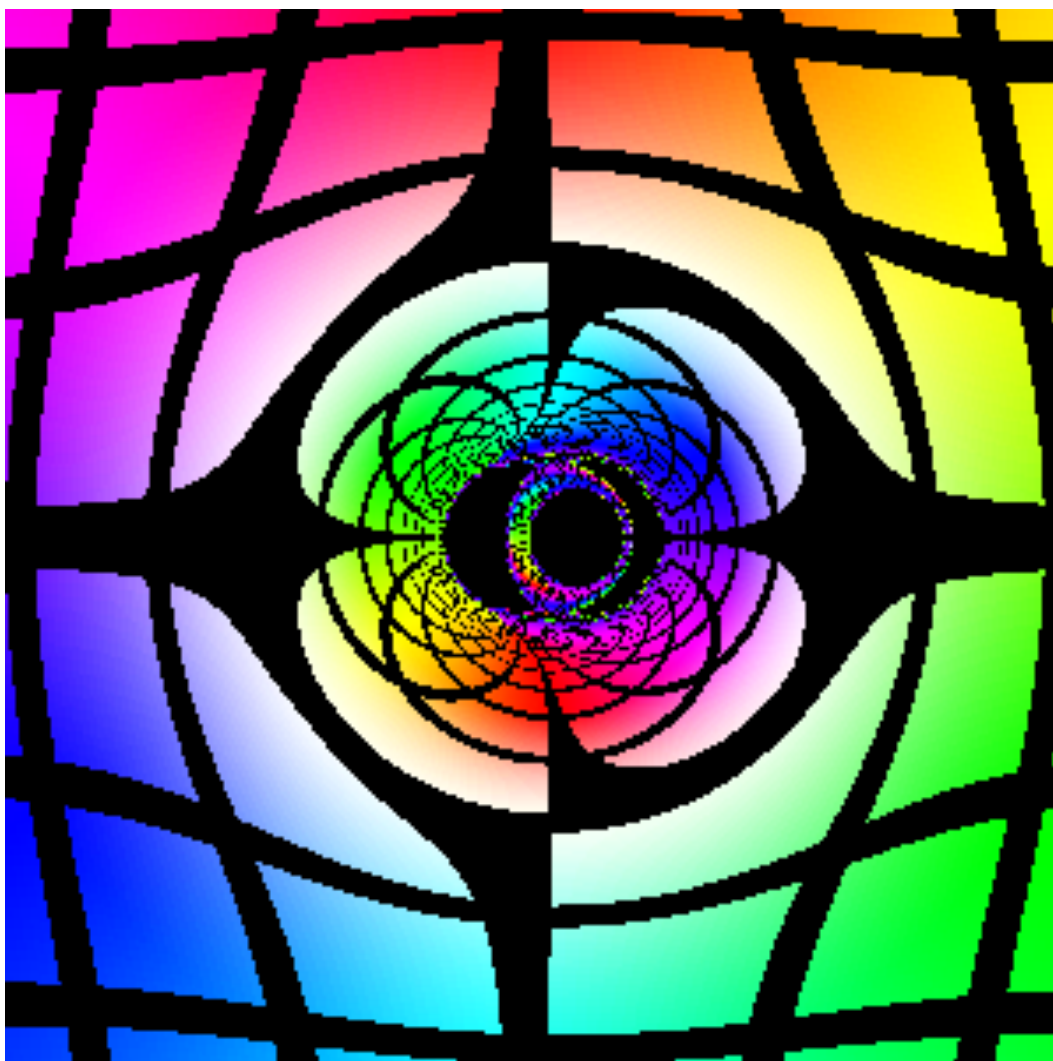


**Figure 3.17:** Side view image of the gradient color map distorted by equal mass binary black holes at  $t = 3937M$  at camera resolution of 300 x 300.

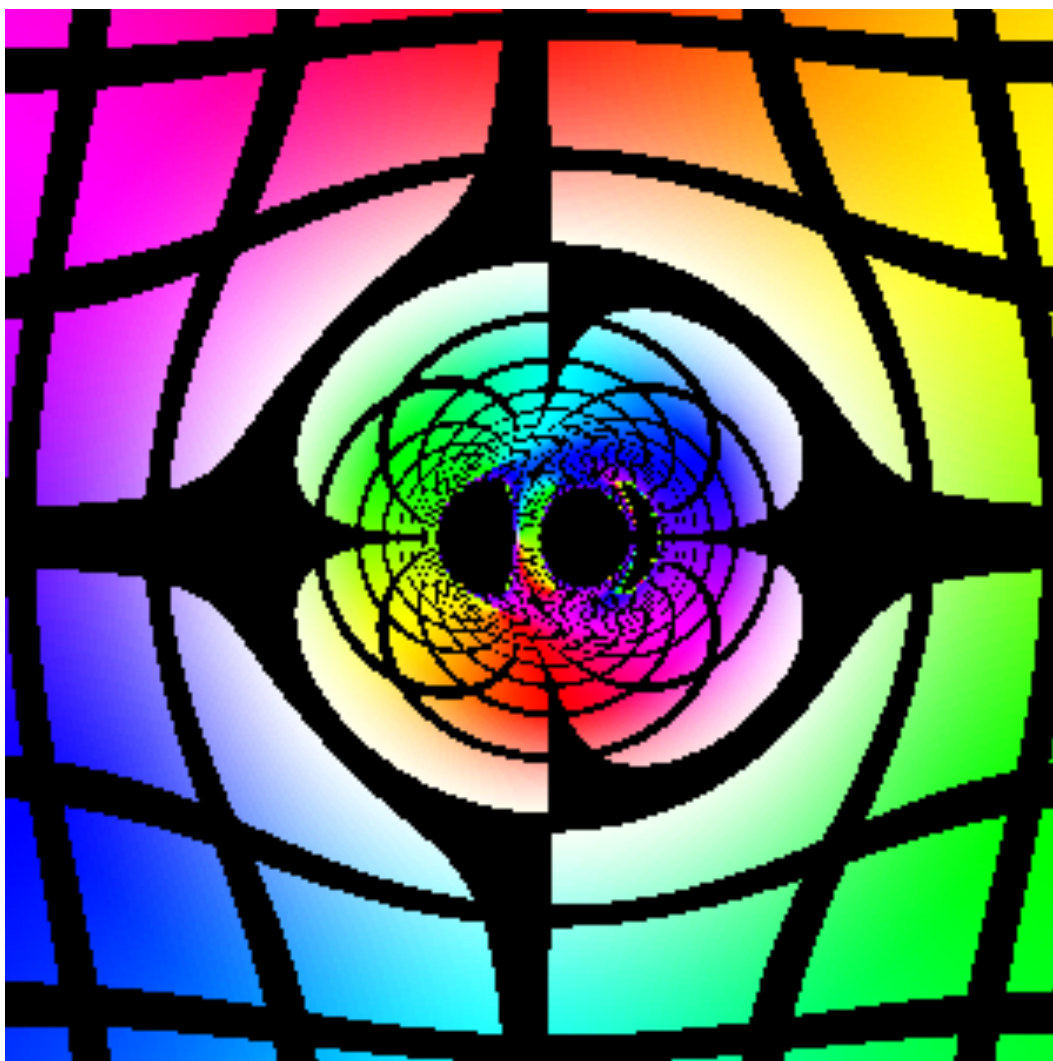


**Figure 3.18:** Side view image of the gradient color map distorted by equal mass binary black holes at  $t = 3941M$  at camera resolution of  $300 \times 300$ .



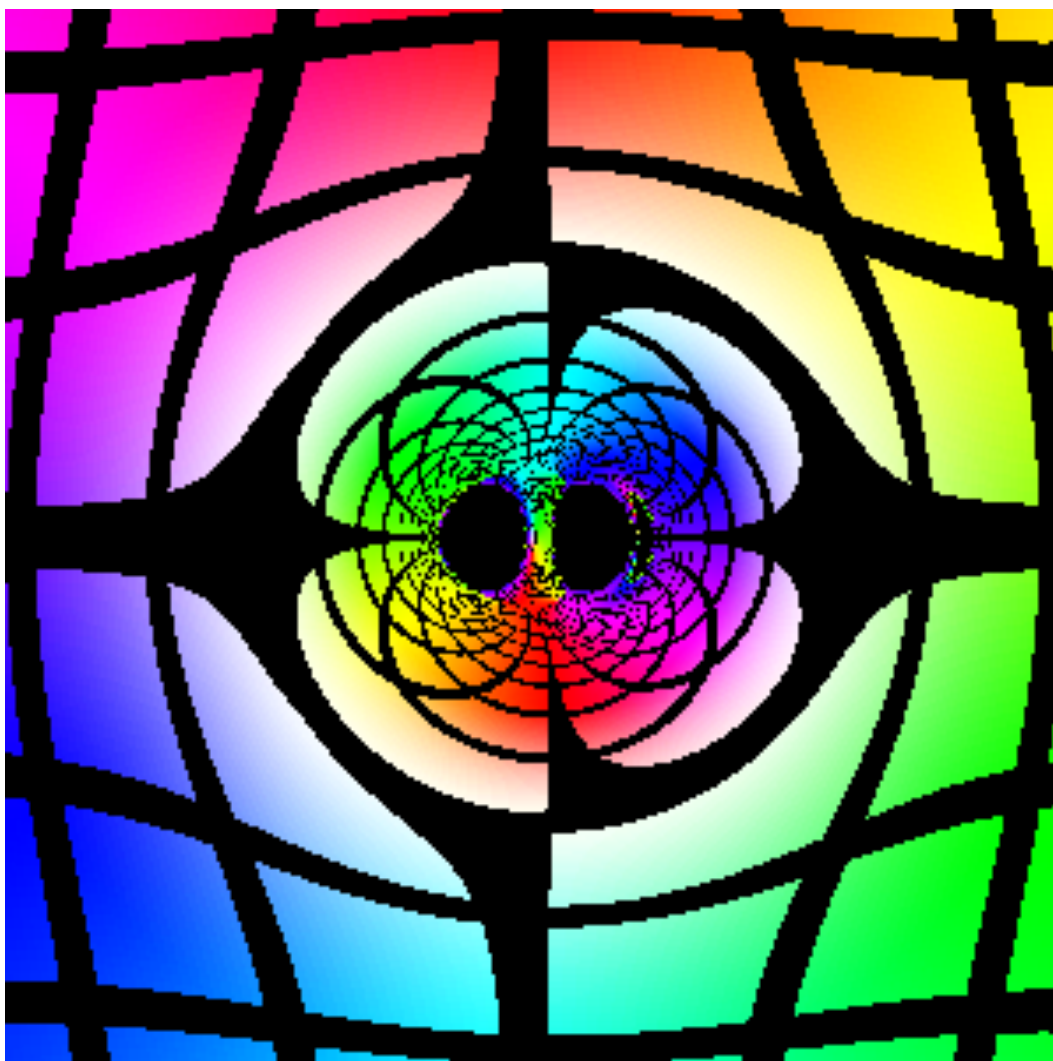


**Figure 3.19:** Side view image of the gradient color map distorted by equal mass binary black holes at  $t = 3946M$  at camera resolution of  $300 \times 300$ .

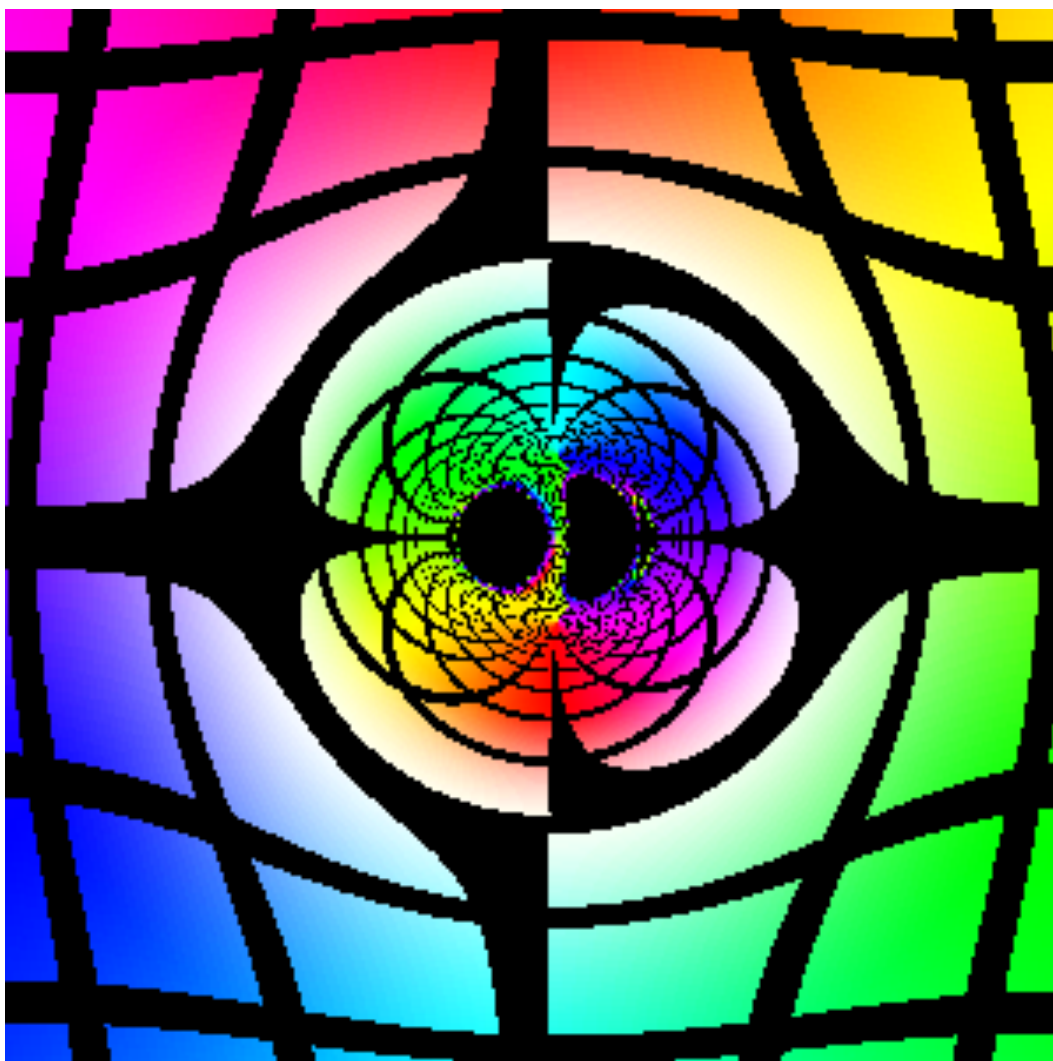


**Figure 3.20:** Side view image of the gradient color map distorted by equal mass binary black holes at  $t = 3951M$  at camera resolution of  $300 \times 300$ .

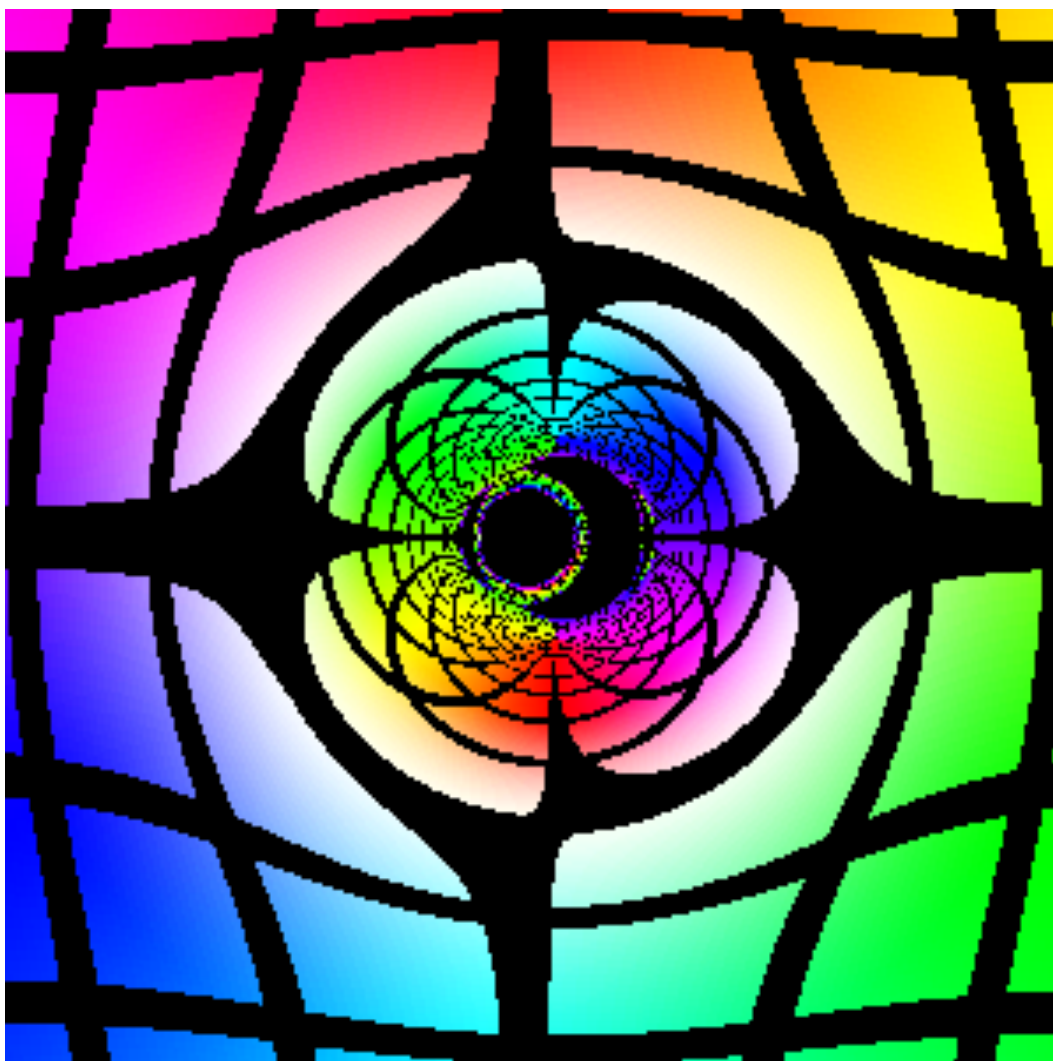


**Figure 3.21:** Side view image of the gradient color map distorted by equal mass binary black holes at  $t = 3956M$  at camera resolution of  $300 \times 300$ .

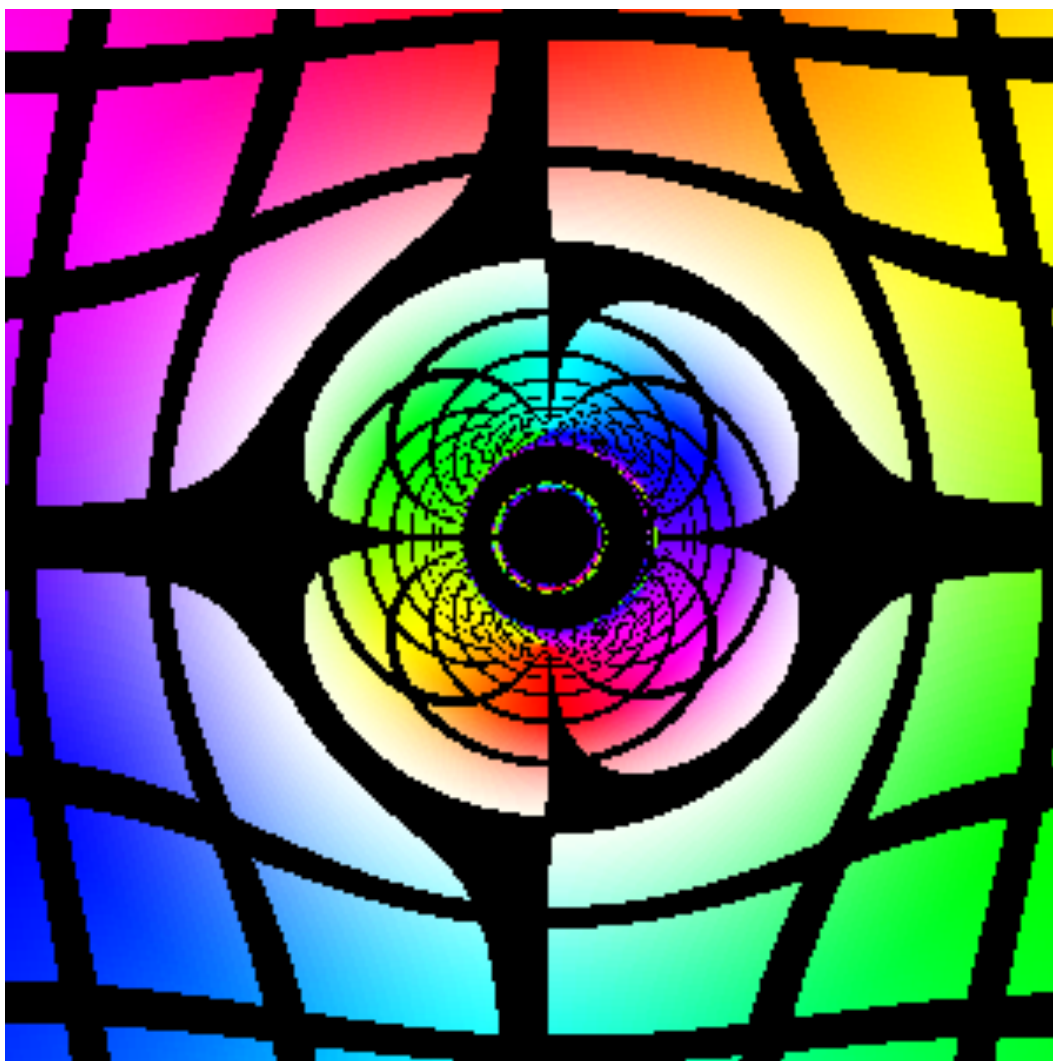


**Figure 3.22:** Side view image of the gradient color map distorted by equal mass binary black holes at  $t = 3961M$  at camera resolution of  $300 \times 300$ .

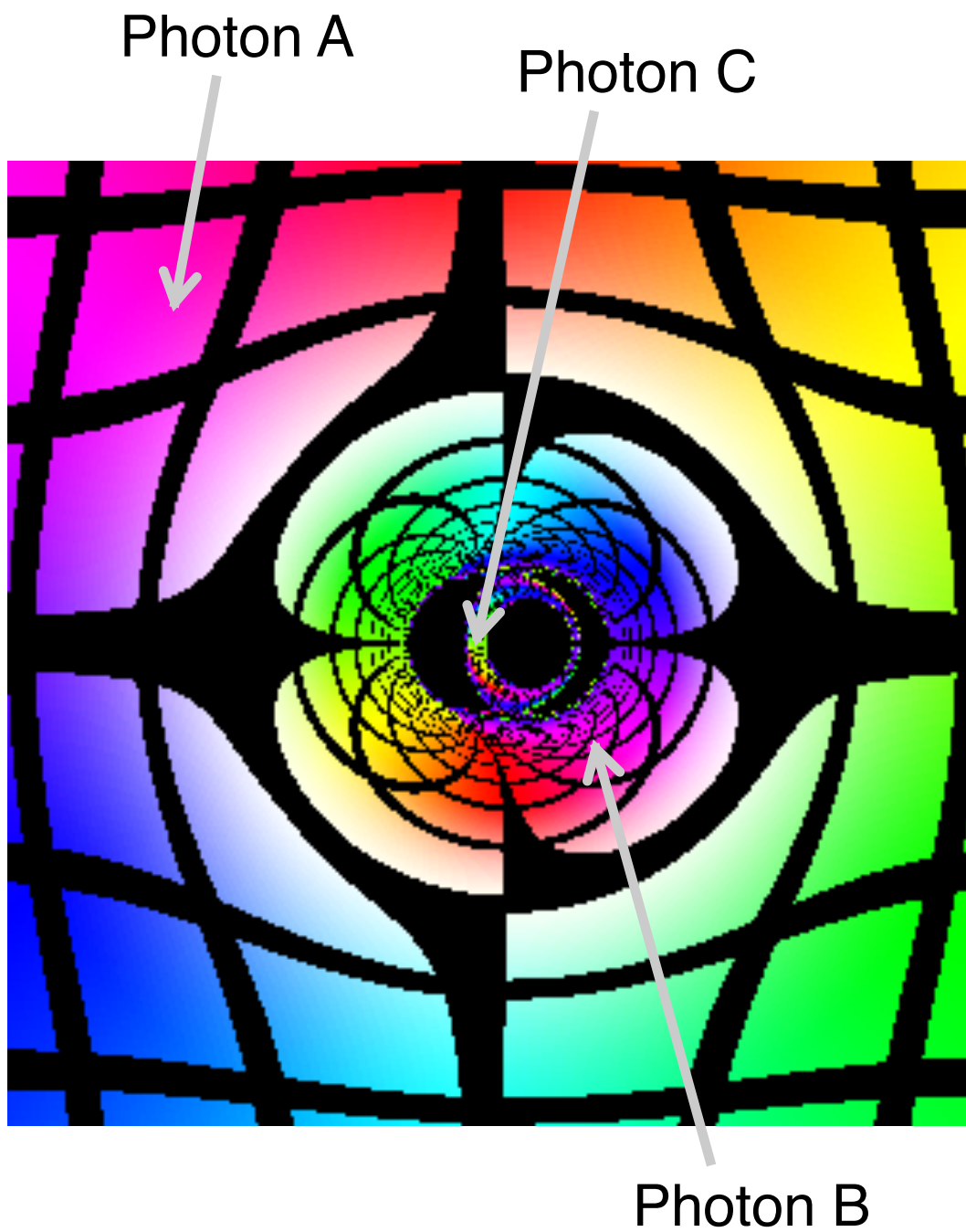


**Figure 3.23:** Side view image of an equal mass binary black hole inspiral observed at  $t = 3937M$ . The trajectories of three labeled photons—one outside the Einstein ring, one inside the Einstein ring, and one inside the slit between the two black holes—are plotted in Fig. 3.24

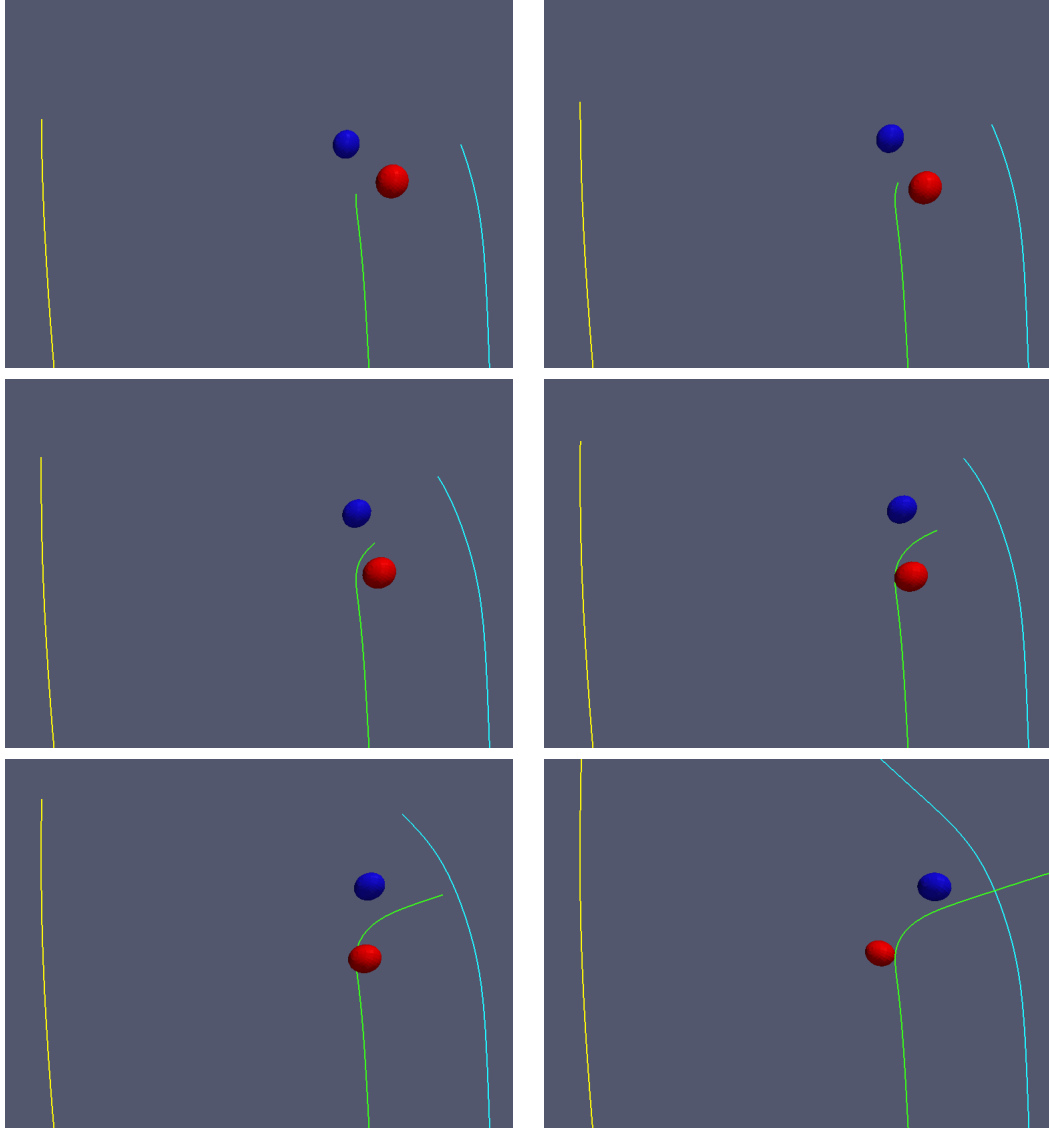


**Figure 3.24:** Trajectories of three photons labeled in Fig. 3.23, started at  $t = 3937M$  and evolved backwards in time. The yellow trajectory corresponds to photon A, the cyan trajectory corresponds to photon B, and the green trajectory corresponds to photon C. The blue and red spheres are the apparent horizons of the two equal mass black holes. From top to bottom, left to right, the snapshots are taken at times  $t = 3874M$ ,  $t = 3872M$ ,  $t = 3870M$ ,  $t = 3867M$ ,  $t = 3860M$ , and  $t = 3855M$ .

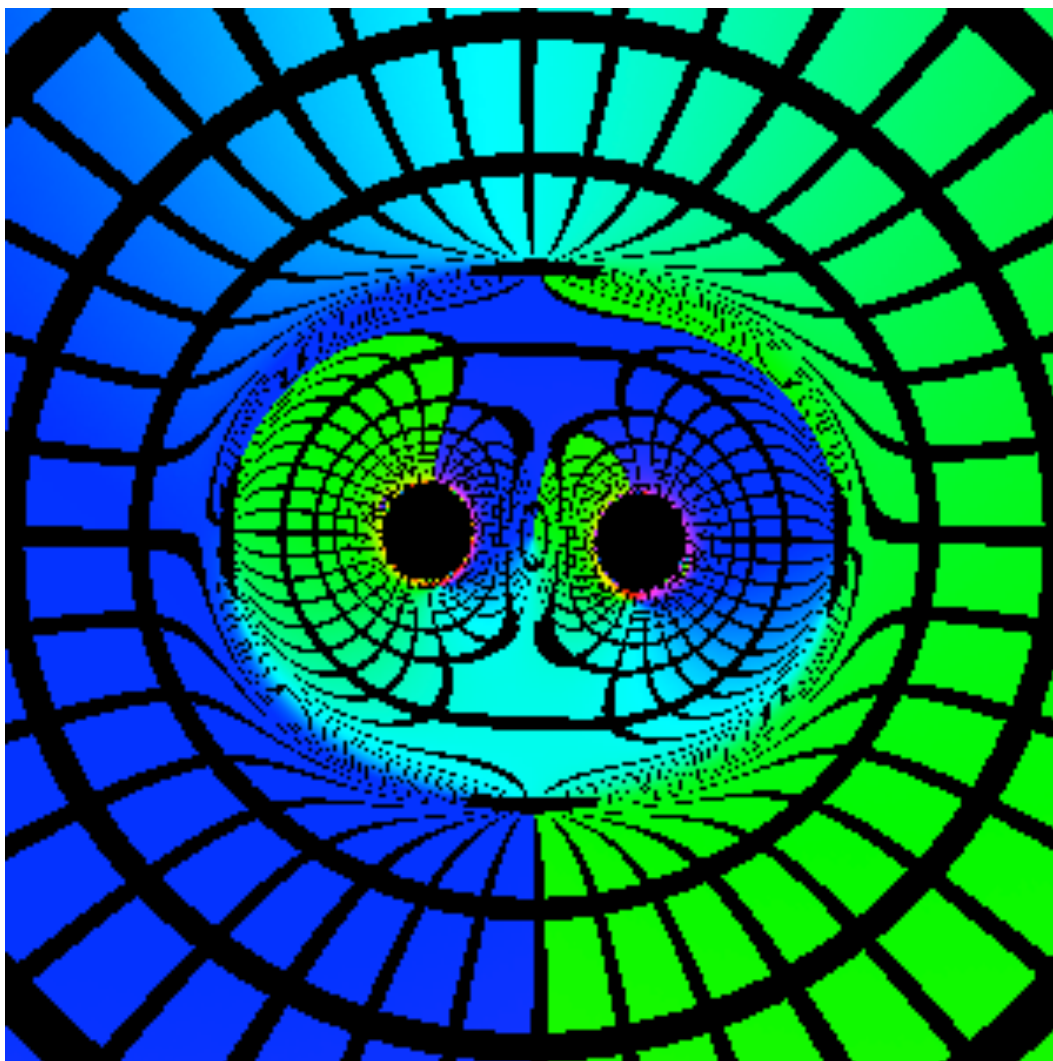


**Figure 3.25:** Top-down view image of the gradient color map distorted by equal mass binary black holes at  $t = 3167M$  at camera resolution of  $300 \times 300$ .

### 3.5 SUMMARY AND FUTURE CONSIDERATIONS

In this chapter, we have explored a robust method of visualizing images that have been distorted by one or more black holes by simply following the trails of photons from the observer back to their sources. The method is robust in the sense that it is able to admit not only static spacetime produced by single black holes, but also dynamical spacetime produced by a binary black hole system. The method involves numerically integrating the normalized form of the null geodesic equation, and it has been shown to agree well with direct integration from analytical equations of motion. The resulting images show strong spacetime distortions both in the single black hole cases and in the binary black hole cases. The amount of the distortion is indicative of the strength of the curvature in the region.

Most importantly, the images that have been distorted by black holes are fascinating in their own right; beyond their scientific application, they would be appealing to the public. These images can certainly be used as pedagogical tools for stimulating scientific interests among school-going children, as well as publicity tools for attracting future science students towards astrophysics.

While the results presented in this chapter serve as a proof that our method is robust, more work is needed to produce high-resolution images with computational cost that is as low as possible. Currently, to produce a  $300 \times 300$  image in a completely dynamical spacetime, such as the equal mass binary



black hole case, we need to use 48 Intel x5650 2.66 GHz Hex Core Processors for roughly 24 hours. The most economical way of improving the resolution of the image, therefore, is to have an adaptive camera that evolves more photons only around under-resolved regions, such as around the black holes. Image interpolation may be sufficient to improve the resolution around the over-resolved regions, such as far away from the black holes.

Moreover, some astrophysically relevant quantities, such as redshift or brightness curves, can also be computed along our method.

# 4

## Finding the Event Horizon

### 4.1 BACKGROUND AND MOTIVATION

The event horizon is a defining feature of a spacetime containing one or more black holes. It is named such because it separates a region in spacetime that can communicate with the future null infinity and a region that cannot. The center of a black hole, which is a location with infinite curvature according to the predictions of general relativity, lies within the event horizon. It has been hypothesized that all such locations—appropriately named as singularities—must be enveloped by an event horizon, hence disconnecting them from the rest of the universe.

The Kerr spacetime, which describes an isolated spinning black hole, has a bound on its maximum allowed spin. If the magnitude of its spin  $J \leq M^2$ , where  $M$  is the mass, then the Kerr spacetime describes a single isolated black hole with an event horizon surrounding its singularity. On the other hand, if the magnitude of the spin  $J > M^2$ , the spacetime will not have an event horizon and a naked singularity exists. A Kerr spacetime with a spin

of  $J > M^2$  is called superextremal, and therefore, the requirement of  $J \leq M^2$  for a Kerr black hole to exist is called the extremality condition.

Unfortunately, most black holes that exist in our universe will not be isolated [23]. They will exist with the presence of other matter, gravitational radiation, or even electromagnetic fields. Therefore, there have been attempts to generalize such extremality condition on a general non-Kerr black hole spacetime [24, 25]. Particularly, Bode *et al.* explored how the generalized extremality conditions can characterize a black hole that has swallowed a spherically symmetric cloud of negative energy density [26]. As the black hole accretes the cloud, its mass decreases and by the conservation of angular momentum, the specific spin  $J/M^2$  increases. Bode *et al.* also showed that as the black hole accretes the cloud, it undergoes severe pancake deformation and loses axisymmetry. If enough negative energy cloud is accreted, the black hole will reach an unstable superextremal state that triggers the emission of gravitational radiation which carries away angular momentum. We, therefore, plan to explore the event horizon of such a black hole in this chapter.

Perhaps the most straightforward way to locate an event horizon in any general black hole spacetime is by evolving outgoing photons or null geodesics backwards in time. Because all outgoing null geodesics that are located outside of the horizon will eventually diverge away from it, they will then approach the horizon when evolved backwards in time. However, instead of tracing the path of individual null geodesics, the eikonal equation allows us

to trace the path of an entire null surface.

In this chapter, we will explore how to locate the event horizon of a black hole that has accreted some negative energy density by solving the eikonal equation using the pseudospectral collocation method.

## 4.2 BLACK HOLES

A black hole is a region in spacetime from which nothing, including null geodesics or photons, can escape to infinity. A black hole is characterized by the presence of an event horizon: a boundary between the region of spacetime that is causally connected to null infinity and the region that is not. In other words, the event horizon is a  $2 + 1$  dimensional hypersurface in spacetime formed by outward-going, future-directed null geodesics that neither escape to infinity nor fall toward the center of the black hole [3]. The event horizon is a coordinate invariant object, and it contains valuable information regarding the black hole spacetime. Therefore, locating the event horizon of a black hole is synonymous to locating the black hole itself.

### 4.2.1 EVENT HORIZON

There are two primary ways that event horizons are located in numerical relativity:

1. The null geodesic method, and
2. The eikonal surface method.

(There is also another method of finding the event horizon dubbed *the surface method*, which is distinct from the eikonal surface method. For a recent review of the surface method and the null geodesic method, please see Ref. [27].)

The null geodesic method locates the event horizon by using the fact that outgoing null geodesics located on the horizon will eventually diverge from it, either toward the center of the black hole or to future null infinity. Conversely, outgoing null geodesics that are located outside of the horizon, if evolved backwards in time, will converge on the horizon. The event horizon, thus, serves as an attractor to the null geodesics [3]. Therefore, to find the event horizon of a black hole using the null geodesic method, one would evolve a large number of null geodesics backwards in time and reconstruct a surface out of the geodesics.

An obvious approach to propagate null geodesics backwards in time is by solving the null geodesic equation:

$$\frac{d^2 x^\mu}{d\lambda^2} + \Gamma^\mu_{\alpha\beta} \frac{dx^\alpha}{d\lambda} \frac{dx^\beta}{d\lambda} = 0, \quad (4.1)$$

as discussed previously in Sec. 2.2. This null geodesic equation can be casted into more appropriate formulations for integration using standard numerical integration schemes such as the Runge-Kutta method. Please refer to Sec. 2.2 for a more complete discussion of the different formulations to the null geodesic equation. The null geodesic method has been successfully implemented to find the horizon of binary black holes by Hughes *et al.* [17].

One of the major disadvantages to the null geodesic method is that the spacetime metric data has to be interpolated to the different locations where the null geodesics are located, and such interpolation can be costly when there are a large number of null geodesics. There have also been concerns that, in a full three-dimensional implementation, the null geodesics may have slight tangential velocities due to numerical errors. The tangential drift may result in unphysical formation of caustics: regions where the event horizon folds onto itself [28]. Concerns with regards to caustics have been the primary reason the null geodesic method has been abandoned in favor of the eikonal surface method. However, Cohen *et al.* found no evidence of such tangential drift when using this method to find the horizon of a equal mass head-on binary black hole collision in Ref. [27].

Instead of propagating individual null geodesics, perhaps a better method is to evolve a 2+1 null hypersurface  $\Gamma$ . The null hypersurface  $\Gamma$  can be defined as a level surface of some function  $S$ , say  $S(t, x^i) = 0$ . The evolution of such a surface is dictated by the eikonal equation:

$$S_{,t} = \beta^i S_{,i} \pm \alpha \sqrt{\gamma^{ij} S_{,i} S_{,j}}. \quad (4.2)$$

For a more complete discussion of the eikonal equation, please refer to Sec. 2.3.

While this surface method alleviates the problem of interpolating and the problem of tangential drift that plague the null geodesic method, this method also has a certain fundamental difficulty. The eikonal function  $S$

can be singular in certain cases, for example in the case of equal mass binary black hole collision. A careful choice of finite-difference stencils may be needed so as not to differentiate across the singularity [27]. Nevertheless, such singularity has only been encountered when locating the event horizon of multiple black holes [29]. Caveny *et al.* has located the event horizon of single black holes as well as binary black holes by solving the eikonal equation using finite difference methods [30].

#### 4.2.2 APPARENT HORIZON

In principle, to locate the event horizon—the true surface of a black hole—requires knowledge of the entire future evolution of the spacetime. This difficulty has led to development of the concept of apparent horizons. The apparent horizon is defined as the outermost smooth, closed 2-surface  $\sigma$ , in a spatial slice  $\Sigma$ , where the outgoing null geodesics have zero expansion everywhere. To elaborate on this point, consider the vector  $s^\alpha$  which is an outward pointing normal vector to  $\sigma$  lying on  $\Sigma$ . Therefore,  $s^\alpha s_\alpha = -1$  and  $s^\alpha n_\alpha = 0$ , where  $n^\alpha$  is the normal vector to  $\Sigma$ .

Just as the spacetime metric  $g_{\alpha\beta}$  induces a spatial metric  $\gamma_{\alpha\beta}$  on the time slice  $\Sigma_t$  in the ADM formalism (see 2.1), the spatial metric  $\gamma_{\alpha\beta}$  induces a 2-dimensional metric  $m_{\alpha\beta}$  on the 2-surface  $\sigma$ ,

$$m_{\alpha\beta} = \gamma_{\alpha\beta} - s_\alpha s_\beta. \quad (4.3)$$

Let  $k^\alpha$  be the tangent vector to all the outgoing future null geodesics whose

projection on  $\Sigma$  is orthogonal to  $\sigma$ . We then have, up to an overall factor,

$$k^\alpha = s^\alpha + n^\alpha, \quad (4.4)$$

on the 2-surface  $\sigma$ .

The expansion of the outgoing null geodesics is therefore,

$$\Theta = \nabla_\alpha k^\alpha, \quad (4.5)$$

where  $\nabla_\alpha$  is the covariant derivative associated with the spacetime metric  $g_{\alpha\beta}$ . The 2-surface  $\sigma$  is marginally trapped if the expansion of the outgoing null geodesics vanishes everywhere on  $\sigma$ , i.e.

$$\Theta = 0. \quad (4.6)$$

Therefore, the apparent horizon is the outermost of a family of such marginally trapped surfaces.

As a consequence from this construction, the apparent horizon can be located from a single spatial slice  $\Sigma$  without any prior knowledge of the future evolution of spacetime. With the addition of the cosmic censorship conjecture that tells us that an apparent horizon—if it exists—must exist within the event horizon, the apparent horizon can often be a practical reliable substitute to the event horizon. In addition, in a stationary spacetime, the apparent horizon—if it exists—will coincide with the event horizon.



However, sometimes using the apparent horizon to locate a black hole is not appropriate because the apparent horizon depends on the choice of spatial slice  $\Sigma$  which makes it a coordinate-dependent object. The event horizon, on the other hand, is the true surface of a black hole and is a coordinate invariant object. For example, the Schwarzschild spacetime can be sliced such that no apparent horizon exists [31]. Therefore, the existence of apparent horizon implies the existence of event horizon (and a black hole), but the converse is not true, the non-existence of apparent horizon does not imply the non-existence of event horizon (and a black hole). In conclusion, it is important to understand the distinction between the apparent horizon and the event horizon.

#### 4.2.3 NOTIONS OF EXTREMALITY

The maximum allowed spin of a Kerr black hole has been well studied. An uncharged, stationary, isolated Kerr black hole with mass  $M$  can only have spin  $J \leq M^2$ . Kerr solutions that have  $J > M^2$  are known as superextremal, and they contain naked singularities instead of black holes. It is, therefore, natural to introduce a dimensionless quasilocal spin parameter

$$\chi = \frac{J}{M^2}, \tag{4.7}$$

so that when  $\chi > 1$ , the Kerr solution is known to be superextremal.

For a general black hole spacetime, the mass  $M$  is known as the Christodoulou Mass, and it is usually obtained by Christodoulou's formula relating spin,

area, and mass of a the black hole,

$$M^2 = M_{irr}^2 + \frac{J^2}{4M_{irr}^2}, \quad (4.8)$$

where the irreducible mass  $M_{irr} = \sqrt{A/16\pi}$  is computed with area  $A$  of the event horizon.

Eq. (4.8) above can be rearranged into

$$\left( \frac{2M_{irr}^2}{M^2} - 1 \right)^2 = 1 - \frac{J^2}{M^4} = 1 - \chi^2. \quad (4.9)$$

The equation, therefore, places a bound on the value of  $\chi \leq 1$ . However, some models of black-hole accretion predict that most black holes will not be isolated from matter or gravitational radiation; most black holes will also have nearly extremal spins [23, 32]. The Kerr notion of extremality with dimensionless spin parameter  $\chi$  is therefore not a useful quantity to diagnose most black holes, simply because they are not isolated Kerr black holes. Following the suggestions of Refs. [24, 25, 26], a better extremality parameter is  $\zeta$  where

$$\zeta = \frac{J}{2M_{irr}^2} = \frac{8\pi J}{A}, \quad (4.10)$$

and then rewriting  $\chi$  into

$$\chi = 1 - \frac{(1 - \zeta)^2}{1 + \zeta^2}. \quad (4.11)$$

The quantity  $\zeta$  is then allowed to exceed 1, but  $\chi \leq 1$  even when  $\zeta > 1$ .

To understand what the quantity  $\zeta$  measures, consider the surface gravity  $\kappa$  that measures the acceleration of gravity at the horizon of a stationary black hole [26]. For an axisymmetric, stationary black hole, the surface gravity  $\kappa$  can be obtained by solving  $\xi^\beta \nabla_\beta \xi^\alpha = \kappa \xi^\alpha$ , where  $\xi^\alpha$  is the Killing vector that is null at the horizon. For example, the surface gravity of a Kerr black hole is

$$\kappa = \frac{1}{2M_{irr}} \frac{\sqrt{1-\chi^2}}{[1 + \sqrt{1-\chi^2}]} = \frac{1-\zeta^2}{4M}. \quad (4.12)$$

The common notion of extremality  $\chi \leq 1$  in Kerr spacetimes is then synonymous to  $\zeta \leq 1$  and  $\kappa \geq 0$ . Therefore, we can relate the quantity  $\zeta$  with the sign of the surface gravity  $\kappa$ .

The new and more general notion of extremality using  $\zeta$  allows us to define

1. a subextremal black hole where  $\zeta < 1$  and  $\kappa > 0$ ,
2. an extremal black hole where  $\zeta = 1$  and  $\kappa = 0$ , and
3. a superextremal black hole where  $\zeta > 1$  and  $\kappa < 0$ ,

all with the dimensionless spin parameter  $\chi \leq 1$ . This definition is applicable to general black hole spacetimes, even those that are non-Kerr. Therefore, a subextremal black hole is one that accelerates a free-particle on the horizon towards the center of the hole, and a superextremal black hole is one that accelerates a free-particle on the horizon away from the hole. An extremal black hole, however, does not accelerate a free-particle on the horizon at all.

## 4.3 NUMERICAL METHOD

### 4.3.1 PSEUDOSPECTRAL COLLOCATION METHOD

We shall use the eikonal surface method of locating the event horizon (see Sec. 4.2.1). In this method, we define null hypersurface  $\Gamma$  to be a level surface of an eikonal function  $S$ , which is evolved by the eikonal equation: Eq. (4.2). Because we are locating the event horizon of only a single black hole, there should not be any concern about  $S$  being singular.

The eikonal equation (Eq. (4.2)) is a hyperbolic partial differential equation (PDE) of the form

$$\partial_t S = \mathcal{L}[\partial_i S]. \quad (4.13)$$

Since this non-linear PDE has been solved using finite-difference method with artificial viscosity [30], we will numerically solve this non-linear PDE using the pseudospectral collocation method. The pseudospectral collocation method approximates the solution to the PDE *globally* within the entire numerical domain. In contrast, the popular finite difference scheme approximates the solution locally [33].

The idea of pseudospectral collocation method is that we approximate the solution  $S$  by a truncated sum of orthogonal basis function  $\phi_k$ ,

$$S_N(t, x^a) = \sum_{k=0}^N c_k(t) \phi_k(x^a). \quad (4.14)$$

The spectral coefficients  $c_k(t)$  are determined such that the residual

$$R_N = \partial_t S_N - \mathcal{L}[\partial_i S_N], \quad (4.15)$$

vanishes at a fixed set of collocation points  $x_i^a$ , leading to

$$\partial_t S_N|_{x_i^a} = \mathcal{L}[\partial_i S_N]|_{x_i^a}, \quad (4.16)$$

with the proper boundary conditions applied. From here, Eq. (4.16) can be transformed, using an appropriate quadrature or a Fast-Fourier Transform (FFT) algorithm (denoted by  $\mathcal{F}$ ), from the spatial basis to the spectral basis such that

$$\frac{dc_k(t)}{dt} = \mathcal{F} \left( \mathcal{L}[\partial_i S_N]|_{x_i^a} \right). \quad (4.17)$$

The ordinary differential equation above can be solved for  $c_k(t + \Delta t)$  using standard time integration routines, such as the forward Euler method.

The main advantage of the pseudospectral collocation method when compared to other spectral methods is that all the non-linear terms, such as the radical in the eikonal equation, are evaluated in the spatial basis—at the collocation points. In the following discussion, we will be making specific choices with regards to the domain, basis functions, collocation points, time evolution routine.

### 4.3.2 CHOICE OF DOMAIN AND BASIS FUNCTIONS

Let us choose to solve the eikonal equation in the spherical coordinate system because the shape of the horizon of a single black hole is usually axisymmetric. It is convenient to pair the spherical coordinate system with a spherical shell domain in which the radial coordinate  $r \in [r_{min}, r_{max}]$ .

We then approximate the solution of the eikonal equation as a truncated sum of our choice of orthonormal polynomial basis functions. With the choice of a spherical shell domain, it is natural to choose to expand the approximate solution in terms of Chebyshev polynomials in the radial direction and in terms of spherical harmonics in the angular directions. This approximate eikonal solution is

$$S_N(t, \rho, \theta, \phi) = \sum_{n=0}^{N_r} \sum_{l=0}^L \sum_{m=-l}^{+l} a_{nlm}(t) T_n(\rho) Y_l^m(\theta, \phi), \quad (4.18)$$

where  $T_n(\rho)$  is the Chebyshev polynomial,

$$T_n(\rho) = \cos \left( n \cos^{-1} \rho \right). \quad (4.19)$$

$\rho \in [-1, 1]$  is the canonical interval for Chebyshev polynomials, and it can be related to the radial coordinate  $r$  by a simple linear mapping:

$$\rho = \frac{2r - (r_{max} + r_{min})}{r_{max} - r_{min}}. \quad (4.20)$$

Also,  $Y_l^m(\theta, \phi)$  is the orthonormal spherical harmonics,

$$Y_l^m(\theta, \phi) = \sqrt{\frac{2l+1}{4\pi} \frac{(l-|m|)!}{(l+|m|)!}} P_l^m(\cos \theta) e^{im\phi}, \quad (4.21)$$

where  $P_l^m$  are the associated Legendre polynomials defined by

$$P_l^m(x) = \frac{(-1)^{l+m}}{2^l l!} (1-x^2)^{m/2} \frac{d^{l+m}}{dx^{l+m}} (1-x^2)^l. \quad (4.22)$$

An advantage of the pseudospectral collocation method is that the spatial derivatives can be computed analytically in the spectral basis. We make use of recurrence relations of the polynomial basis functions when evaluating the derivatives.

The partial derivative with respect to  $\rho$  is

$$\frac{\partial S_N}{\partial \rho}(t, \rho, \theta, \phi) = \sum_{n=0}^{N_r} \sum_{l=0}^L \sum_{m=-l}^{+l} a_{nlm}(t) \frac{dT_n(\rho)}{d\rho} Y_l^m(\theta, \phi), \quad (4.23)$$

where  $\sum a_{nlm} \frac{dT_n}{d\rho}$  can be rewritten in terms of another sum over Chebyshev polynomials,

$$\frac{\partial S_N}{\partial \rho}(t, \rho, \theta, \phi) = \sum_{n=0}^{N_r} \sum_{l=0}^L \sum_{m=-l}^{+l} a'_{nlm}(t) T_n(\rho) Y_l^m(\theta, \phi), \quad (4.24)$$

by using the recurrence relation

$$c_n a'_{nlm} = a'_{(n+2)lm} + 2(n+1)a_{(n+1)lm}, \quad (4.25)$$

where

$$c_n = \begin{cases} 2 & \text{if } n = 0 \\ 1 & \text{if } n \geq 1 \end{cases}. \quad (4.26)$$

From here, it is trivial to obtain the partial derivative with respect to  $r$ ,

$$\frac{\partial S_N}{\partial r} = \frac{\partial \rho}{\partial r} \frac{\partial S_N}{\partial \rho} = \frac{2}{r_{\max} - r_{\min}} \frac{\partial S_N}{\partial \rho}. \quad (4.27)$$

Similarly, the partial derivative with respect to  $\theta$  is

$$\frac{\partial S_N}{\partial \theta}(t, \rho, \theta, \phi) = \sum_{n=0}^{N_r} \sum_{l=0}^L \sum_{m=-l}^{+l} a_{nlm}(t) T_n(\rho) \frac{\partial Y_l^m(\theta, \phi)}{\partial \theta}, \quad (4.28)$$

where  $\sum a_{nlm} \frac{\partial Y_l^m}{\partial \theta}$  can be rewritten in terms of another sum over spherical polynomials by using the recurrence relation

$$\frac{\partial Y_l^m}{\partial \theta} = m \cot \theta Y_l^m + \sqrt{(l-m)(l+m+1)} e^{-i\phi} Y_l^{m+1}. \quad (4.29)$$

Note the singularity at the poles ( $\theta = 0, \pi$ ), this means that we need to choose collocation points that avoid the poles.

Moreover, the partial derivative with respect to  $\phi$  is

$$\begin{aligned} \frac{\partial S_N}{\partial \phi}(t, \rho, \theta, \phi) &= \sum_{n=0}^{N_r} \sum_{l=0}^L \sum_{m=-l}^{+l} a_{nlm}(t) T_n(\rho) \frac{\partial Y_l^m(\theta, \phi)}{\partial \phi} \\ &= \sum_{n=0}^{N_r} \sum_{l=0}^L \sum_{m=-l}^{+l} a'_{nlm}(t) T_n(\rho) Y_l^m(\theta, \phi), \end{aligned} \quad (4.30)$$



where

$$a'_{nlm} = (im)a_{nlm}. \quad (4.31)$$

#### 4.3.3 CHOICE OF COLLOCATION POINTS

The choice of collocation points should not only ease the computation of quadrature for transformation from spatial basis to spectral basis, but it should also prevent the onset of Runge phenomenon. The Runge phenomenon is the tendency for interpolation using the polynomial basis functions to oscillate wildly near the boundaries of a domain caused by numerical truncation of the basis functions [34].

We shall choose the Chebyshev-Gauss-Lobatto collocation points in the radial direction,

$$\rho_i = -\cos\left(\frac{\pi}{N_r}i\right), \quad \forall i \in [0, \dots, N_r], \quad (4.32)$$

with the Chebyshev-Gauss-Lobatto quadrature:

$$\int_{-1}^{+1} \frac{T_n(\rho)f(\rho)}{\sqrt{1-\rho^2}} d\rho \approx \sum_{i=0}^{N_r} T_n(\rho_i)f(\rho_i)w_i, \quad (4.33)$$

where

$$w_i = \frac{\pi}{c_i N_r}, \quad c_i = \begin{cases} 2 & \text{if } i = 0, N_r \\ 1 & \text{if } i \in [1, \dots, N_r - 1] \end{cases}. \quad (4.34)$$

In the  $\theta$ -direction, since we are expanding  $\cos \theta$  in terms of Legendre polynomials, we shall use the Legendre-Gauss collocation points where  $\cos \theta_j$

are the roots of Legendre polynomial of order  $L + 1$ . On the other hand, since the  $\phi$  direction is expanded in terms of complex Fourier functions  $e^{im\phi}$ , we shall choose the Fourier collocation points which are equispaced,

$$\phi_k = \frac{2\pi}{2L+1}, \quad \forall k \in [0, \dots, 2L]. \quad (4.35)$$

Spectral transformation from the spatial basis to the spectral basis in the angular direction is done by using SHTOOLS ([shtools.ipgp.fr](http://shtools.ipgp.fr)), which is a spherical harmonics FFT library. In the library, we choose the Legendre-Gauss algorithm that makes use of Legendre-Gauss quadrature in the  $\theta$ -direction and conventional FFT in the  $\phi$ -direction.

#### 4.3.4 TIME EVOLUTION AND BOUNDARY CONDITIONS

We evolve the hyperbolic eikonal equation using the method of lines, where we cast the equation into similar to Eq. (4.17) and use a standard ODE solver to integrate the equation in time. Even though any standard choice of ODE solver such as fourth-order explicit Runge-Kutta would work, we choose to integrate using the five-stage fourth-order Strong Stability Preserving Runge-Kutta (SSPRK{5,4})—outlined in Appendix A. The SSPRK method is an extension of the common Runge-Kutta method.

We use the SSPRK{5,4} mainly because its time discretization is similar to that of forward Euler method and we only need to obtain the spacetime metric data at a single time  $t$ . This is a significant advantage because the metric data have to be interpolated in time, and thus obtaining the metric data at a

single time will reduce computational costs. In fact, most of our computational time is spent on reading in metric data and interpolating. On the other hand, if we decide to use the fourth-order explicit Runge-Kutta, we will need to obtain the metric data at three different times:  $t, (t + 1/2\Delta t), (t + \Delta t)$ .

When using the pseudospectral collocation method, boundary conditions are more easily imposed than when using a finite difference scheme. In a finite difference scheme, derivatives are approximated by differences between neighboring grid points. The pattern of grid points must then be modified at the boundaries of the numerical grid. On the other hand, the approximate solution is given globally over the entire computational domain in pseudospectral collocation method. This allowed us to compute the derivatives analytically and nothing special needs to be done to compute the derivatives at the boundary. In addition, since there are collocation points on the boundary, we can simply demand that the approximate solution satisfy the exact boundary condition at the boundary collocation point.

Our boundary condition is Neumann,

$$\frac{\partial S}{\partial r} = 0 \tag{4.36}$$

at  $r = r_{max}$  and  $r = r_{min}$ . We simply demand that this condition is satisfied at these two radial boundary collocation points, which are also equivalent to  $\rho = -1$  and  $\rho = +1$ .

Nevertheless, it is important to note that the pseudospectral collocation method places a more severe Courant stability limit  $\Delta t \sim \mathcal{O}(N_r^{-2})$  on a

wave equation than for finite difference scheme, where  $\Delta t \sim \Delta r \sim \mathcal{O}(N_r^{-1})$  [33]. This severe Courant stability limit is caused by the placement of the collocation points that are clustered near the domain boundaries to prevent the onset of Runge phenomenon. Therefore, the time step in pseudospectral collocation method may be smaller than that of the finite difference method.

#### 4.3.5 EXTRACTION OF NULL SURFACE AND INITIAL CONDITIONS

The null surface  $\Gamma$ , at any time level, can be extracted from the level set section of the eikonal function at, say,  $S = 1$ . The problem of extraction is an inverse problem, since it requires the points  $(r, \theta, \phi)$  to be found such that  $S(r(\rho), \theta, \phi) = 1$ . Because we are expanding  $S_N$  in terms of spherical harmonics which are complex functions while we know that  $S$ , physically, is a real function, we therefore extract the null surface from  $|S_N| = \sqrt{S_N^* S_N}$ . A combination of ordinary bisection and interpolation methods prove to be sufficient to extract the approximate null surface  $\Gamma_N$ . Because all the radial points of  $S$  are already on the Chebyshev-Gauss-Lobatto grid, it is convenient to interpolate using Chebyshev spectral interpolation. The surface  $\Gamma_N$  can then be represented as a surface function  $r = u(\theta, \phi)$ . For example,  $r = \text{constant}$  for a Schwarzschild black hole and  $r = u(\theta)$  for a Kerr black hole due to axisymmetry.

Initial data for the solution of the eikonal equation are set in the following form

$$S_N(t = t_0, r(\rho), \theta, \phi) = 1 + \tanh \left( \frac{r_0(\theta, \phi) - r}{c} \right), \quad (4.37)$$

where  $r_0(\theta, \phi)$  is the radial extent of the initial null surface  $\Gamma$  at angular direction  $(\theta, \phi)$ . We choose  $r_0(\theta, \phi)$  such that it is as close as possible to the event horizon of the black hole that we are dealing with. For example, if we are dealing with a non-spinning Schwarzschild black hole, we would specify  $r_0 = \text{constant}$  for all  $(\theta, \phi)$ , and if we are dealing with a Kerr black hole, we would specify an axisymmetric  $r_0(\theta, \phi)$ . A good rule of thumb is to specify  $r_0(\theta, \phi)$  such that the radial extent in all the angular directions, are slightly larger than that of the apparent horizon.

In Eq. (4.37),  $c$  controls the steepness of the hyperbolic tangent function and is chosen such that the Chebyshev spectral expansion can resolve the steep jump well enough. We find that  $c = 0.1$  is appropriate for  $N_r \geq 40$ .

#### 4.3.6 REINITIALIZATION

There are two major sources of error in pseudospectral collocation method that need to be controlled—truncation error and aliasing error [33]. Truncation error is caused by the fact that we are neglecting the higher order polynomial basis functions in our series expansion. Aliasing error, on the other hand, occurs because each neglected higher order term is indistinguishable from some lower order terms which are not neglected when we are sampling only at the collocation points. As a result, contribution from the higher order terms—instead of being completely neglected—contributes to some lower order modes.

The truncation and aliasing errors will inevitably limit the numerical ac-

curacy of the pseudospectral collocation method, but the aliasing error also affects the stability of the algorithm. Therefore, it is imperative that we control the aliasing error.

Most numerical simulations that use pseudospectral collocation method implement some kind of smooth filtering such as an exponential filter to reduce aliasing error [33]. However, due to the nature of our problem where we are only interested in a level set section of the solution, we can reinitialize the data after a number of iterations instead,

$$S_N(t, r(\rho), \theta, \phi) = 1 + \tanh \left( \frac{u(t, \theta, \phi) - r}{c'} \right). \quad (4.38)$$

We do so after every 15 iterations. Here  $c'$  denotes a new steepness of the hyperbolic tangent function and our simulation uses  $c' = c$ . Recall that  $u(t, \theta, \phi)$  is the surface function that describes the approximate null surface  $\Gamma_N$ .

#### 4.3.7 AREA CALCULATION

Perhaps, one of the most important result from finding the event horizon of a black hole is the horizon's proper surface area  $A$ .

Consider the spatial line element in spherical coordinates,

$$^{(3)}ds^2 = \gamma_{ij} dx^i dx^j, \quad (4.39)$$

where  $x^i \rightarrow (r, \theta, \phi)$ . We can find the induced two-metric  $h_{ij}$  for a 2-surface

of constant  $r$  from the spatial metric  $\gamma_{ij}$  by realizing that

$$dr = \frac{\partial r}{\partial \theta} d\theta + \frac{\partial r}{\partial \phi} d\phi, \quad (4.40)$$

since on the null surface  $\Gamma$ , we have  $r = u(\theta, \phi)$ . Therefore,

$$h_{ab} = \gamma_{ij} x^i_{,a} x^j_{,b}. \quad (4.41)$$

The area of this 2-surface is then given by

$$A(t) = \oint dA = \oint \frac{\sqrt{h(t, \theta, \phi)}}{\sin \theta} \sin \theta d\theta d\phi, \quad (4.42)$$

where

$$h = |h_{ab}| = \det \begin{pmatrix} \gamma_{ij} x^i_{,\theta} x^j_{,\theta} & \gamma_{ij} x^i_{,\theta} x^j_{,\phi} \\ \gamma_{ij} x^i_{,\phi} x^j_{,\theta} & \gamma_{ij} x^i_{,\phi} x^j_{,\phi} \end{pmatrix}, \quad (4.43)$$

is evaluated on the extracted null surface  $\Gamma$ , i.e. at  $r = u(\theta, \phi)$ .

In (4.42), by explicitly dividing  $\sqrt{h}$  by  $\sin \theta$ , we allow the integration to be done over the solid angle on a unit 2-sphere. Since all the values of  $r = u(\theta, \phi)$  are on a Legendre-Gauss grid with no collocation point at the poles ( $\theta = 0$  or  $\pi$ ), we can compute the derivatives in (4.43) spectrally and the integral in (4.42) by Legendre-Gauss quadrature.

### 4.3.8 OBTAINING METRIC DATA

All the black holes in this chapter are numerically evolved in Cartesian coordinates, but because the event horizon finder uses spherical coordinates, we need to perform coordinate transformation on the metric data.

The coordinate transformation is perhaps most easily done by considering the line element

$$ds^2 = \bar{g}_{\alpha\beta} d\bar{x}^\alpha d\bar{x}^\beta = g_{\mu\nu} dx^\mu dx^\nu, \quad (4.44)$$

where the barred variables are in Cartesian coordinates, i.e.  $\bar{x}^\alpha \rightarrow (t, x, y, z)$ , and the unbarred variables are in the spherical coordinates, i.e.  $x^\mu \rightarrow (t, r, \theta, \phi)$ .

Since  $d\bar{x}^\alpha = \frac{\partial \bar{x}^\alpha}{\partial x^\mu} dx^\mu$ , we can rewrite the line element to be:

$$\bar{g}_{\alpha\beta} \frac{\partial \bar{x}^\alpha}{\partial x^\mu} \frac{\partial \bar{x}^\beta}{\partial x^\nu} dx^\mu dx^\nu = g_{\mu\nu} dx^\mu dx^\nu. \quad (4.45)$$

Let us define  $\frac{\partial \bar{x}^\alpha}{\partial x^\mu} = J^\alpha_\mu$  be the Jacobian matrix to transform a one-form in Cartesian coordinates to a one-form in spherical coordinates. With Eq. (4.45) and the Jacobian matrix, we can then obtain the metric data in spherical coordinates,

$$g_{\mu\nu} = \bar{g}_{\alpha\beta} J^\alpha_\mu J^\beta_\nu, \quad (4.46)$$

or in the matrix form

$$\mathbf{g} = \mathbf{J}^T \bar{\mathbf{g}} \mathbf{J}. \quad (4.47)$$

Moreover, because the event horizon finder evolves the surface  $S$  backwards in time, it cannot run concurrently with the black hole evolution.



We, therefore, dump the spacetime metric data containing the black hole on some grid, at some regular time interval. Since the spacetime metric data might not be dumped at the time and the spatial collocation points desired by the event horizon finder, interpolation is necessary. We interpolate using 4th-order Lagrange interpolation temporally [35], and we interpolate using tricubic interpolation spatially [36].

The event horizon finder, when reading the metric data, therefore performs the following operations:

1. interpolates the Cartesian metric data  $\bar{g}_{\alpha\beta}$  spatially to the desired collocation points,
2. performs coordinate transformation on the metric from Cartesian coordinates to spherical coordinates, and
3. interpolates the metric data  $g_{\mu\nu}$  temporally to the desired time.

#### 4.4 APPLICATION TO PUNCTURE BLACK HOLES

We characterize the performance of our event horizon finder by applying it to black holes that have been numerically evolved using the puncture method, where a puncture singularity representing the singularity of the black hole is placed in the computational domain with the caveat that the singularity is never placed on a grid point. The puncture method is evolved by the MAYA code using the Baumgarte-Shapiro-Shibata-Nakamura (BSSN) [37, 38] evolution equations, which are a modification from the conventional

ADM evolution equations. In these simulations, we start with metric data in the isotropic or quasi-isotropic coordinates. This choice of coordinates is not stationary in the BSSN formalism, and the metric quantities behave dynamically for a brief period—settling down to a new, time-independent solution that is different than the initial data. (For a more complete review of this formalism, see Ref. [3]).

#### 4.4.1 NON-SPINNING PUNCTURE BLACK HOLE

For our tests on a spacetime with a non-spinning puncture black hole, we choose an initial surface of a coordinate sphere of radius  $r_0(\theta, \phi) = 0.98$  because this black hole is spherically symmetric. This choice of initial surface radius is slightly larger than the apparent horizon, which is a sphere of radius  $r_{AH} = 0.9757$  at  $t_0 = 50M$ . (All our radial coordinates are presented in arbitrary units dictated by the MAYA code.) The event horizon finder begins at  $t_0 = 50M$  and proceeds backwards in time towards  $t = 0M$ .

We then choose the orders ( $N_r$  and  $L$ ) at which we wish to truncate our spectral expansion of  $S$  as a measure of resolution. With a spherically symmetric spacetime, we expect the choice of  $L$  will not affect the performance of the event horizon finder because only the  $Y_0^0(\theta, \phi)$  term will be non-zero. We, therefore, choose  $N_r = 30, 40, 50, 60, 70$ , and  $L = 30$ .

In order to test our event horizon finder's performance, we shall use two different measures of error. The first is the error in the coordinate location  $r_{EH}$  of the approximate null surface  $\Gamma_N$  relative to the coordinate location

$r_{AH}$  of the apparent horizon:

$$\Delta r(t) = r_{EH}(t) - r_{AH}(t). \quad (4.48)$$

Because the spacetime is spherically symmetric, the value of the radial coordinates of  $r_{EH}$  and  $r_{AH}$  are independent of  $(\theta, \phi)$ . The non-spinning puncture black hole in this case is a different, time-dependent, coordinate representation of the Schwarzschild spacetime, which is a stationary spacetime. As a result, even though the metric is dynamical, it is always (to numerical accuracy) the spherical, physically static black hole. Therefore, the apparent horizon—when it exists—and the event horizon always coincide for this spacetime, regardless of slicing.

The second measure of error is the deviation of the area  $A$  of the approximate null surface  $\Gamma_N$  from the area  $A_{AH}$  of the apparent horizon:

$$\Delta A(t) = A(t) - A_{AH}(t), \quad (4.49)$$

where  $A(t)$  is calculated using Eq. (4.42).

Fig. 4.1 shows how the radial coordinate  $r_{EH}$  of the null surface  $\Gamma_N$  behaved throughout the evolution relative to the radial coordinate  $r_{AH}$  of the apparent horizon. Fig. 4.2 shows how the area of the null surface  $\Gamma_N$  compares to the area of the apparent horizon. Fig. 4.3 shows the absolute difference in the radial coordinate locations (Eq. (4.48)). The figure suggests that the value of  $|\Delta r|$  oscillates at  $\mathcal{O}(10^{-4})$  for all different orders of  $N_r$ .

Therefore, the value of  $|\Delta r|$  does not depend significantly on the choice of  $N_r$  within the range that we have chosen (between  $N_r = 30$  to  $N_r = 70$ ). Fig. 4.4, on the other hand, shows the normalized absolute difference in the areas (Eq. (4.49)). Similarly, the figure suggests that the value of  $|\Delta A|/A(t)$  also does not depend significantly on the choice of  $N_r$ , within the range that we have chosen—oscillating at  $\mathcal{O}(10^{-5})$ .

The fact that these two error measures are independent of our choices of  $N_r$  suggests that the resolution of our event horizon finder is limited by the resolution of the dumped metric data, which is 0.0125 (finest) spatially and  $0.00625M$  temporally. In this particular case of non-spinning black hole, we find the event horizon with  $|\Delta r| \sim \mathcal{O}(10^{-4})$  shows that the event horizon finder has performed well.

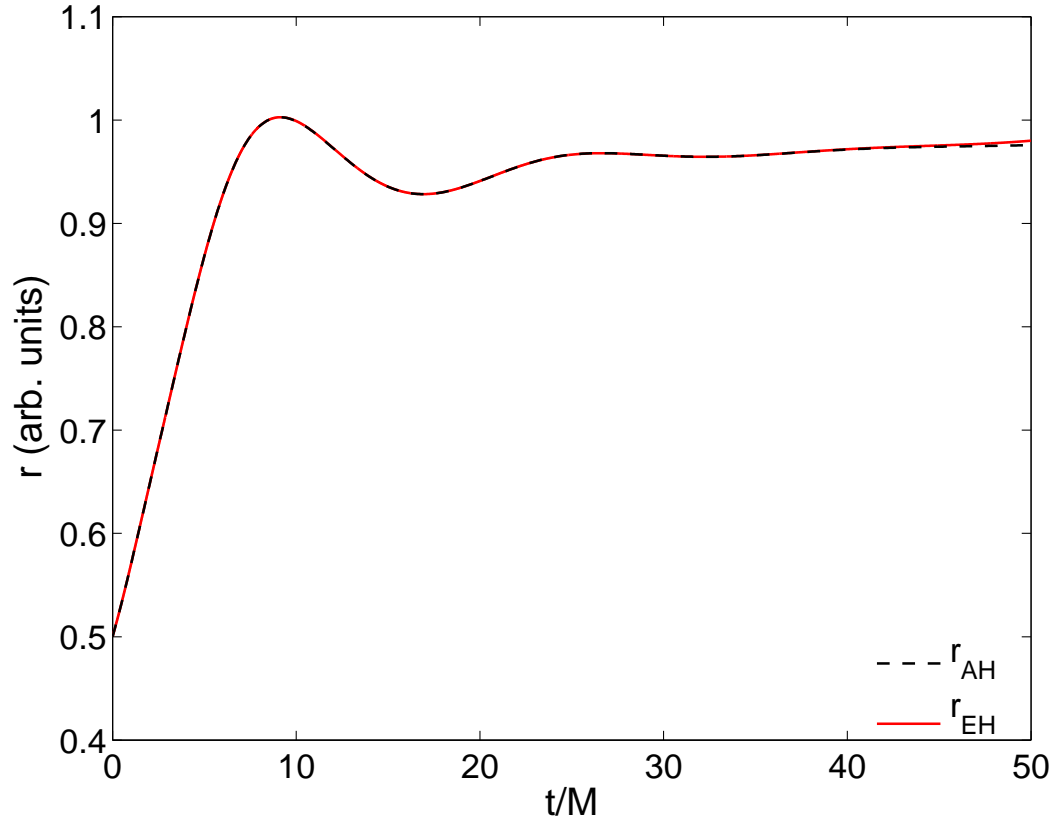


**Figure 4.1:** A comparison between the maximum and minimum radial coordinate locations for both the null surface  $\Gamma_N$  and the apparent horizon. In this case,  $N_r = 40$  and  $L = 30$ . The black hole is a non-spinning puncture black hole. The event horizon finder starts at  $t = 50M$  and evolves backwards in time.

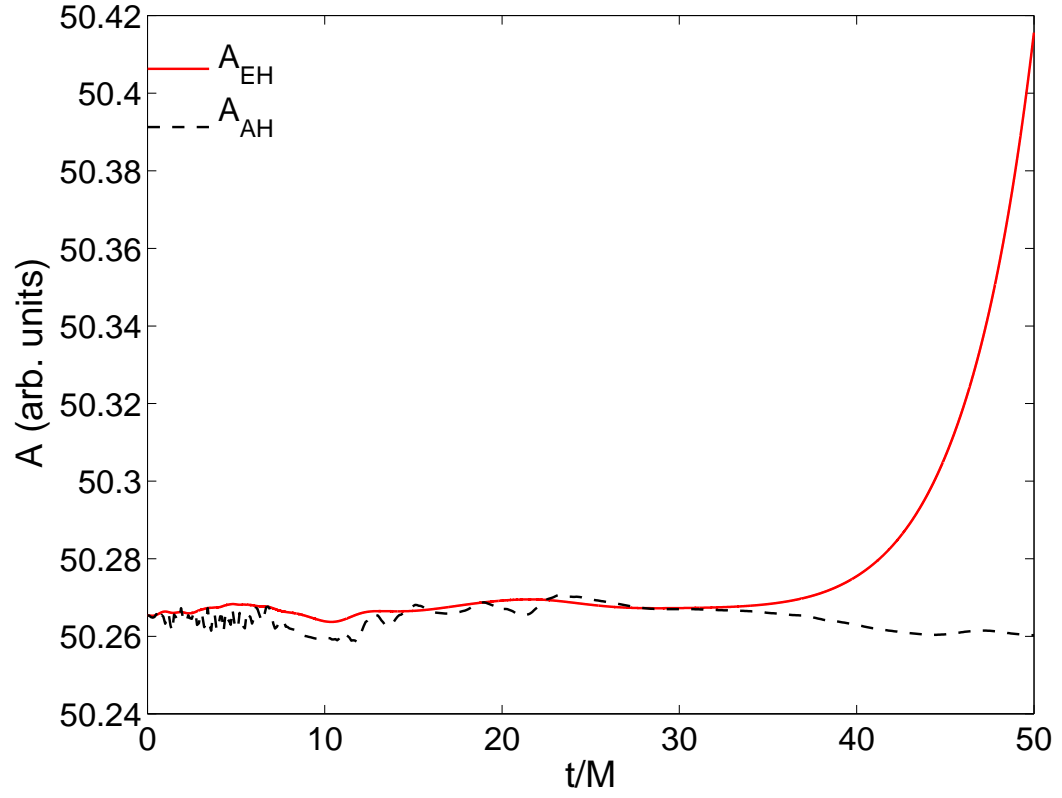


**Figure 4.2:** A comparison between the area of the null surface  $\Gamma_N$  and the area of the apparent horizon. In this particular case  $N_r = 40$  and  $L = 30$ . The black hole is a non-spinning puncture black hole. The event horizon finder starts at  $t = 50M$  and evolves backwards in time.

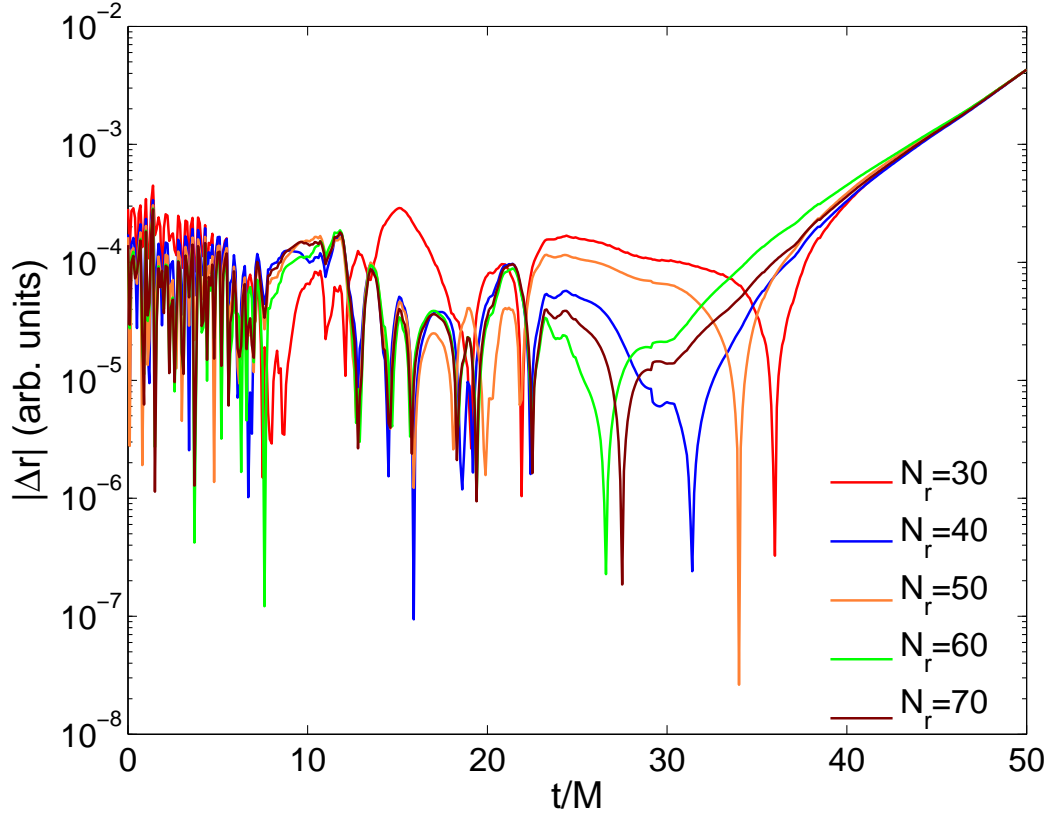


**Figure 4.3:** Absolute difference in the radial coordinate location between the null surface  $\Gamma_N$  and the apparent horizon, for different orders of Chebyshev expansion:  $N_r = 30, 40, 50, 60, 70$ . The black hole is a non-spinning puncture black hole. The order of spherical harmonic expansion is kept fixed at  $L = 30$ . The event horizon finder starts at  $t = 50M$  and evolves backwards in time. The growing difference at late times reflects the event horizon tracker's exponential approach to the horizon, as it is evolved backwards in time.

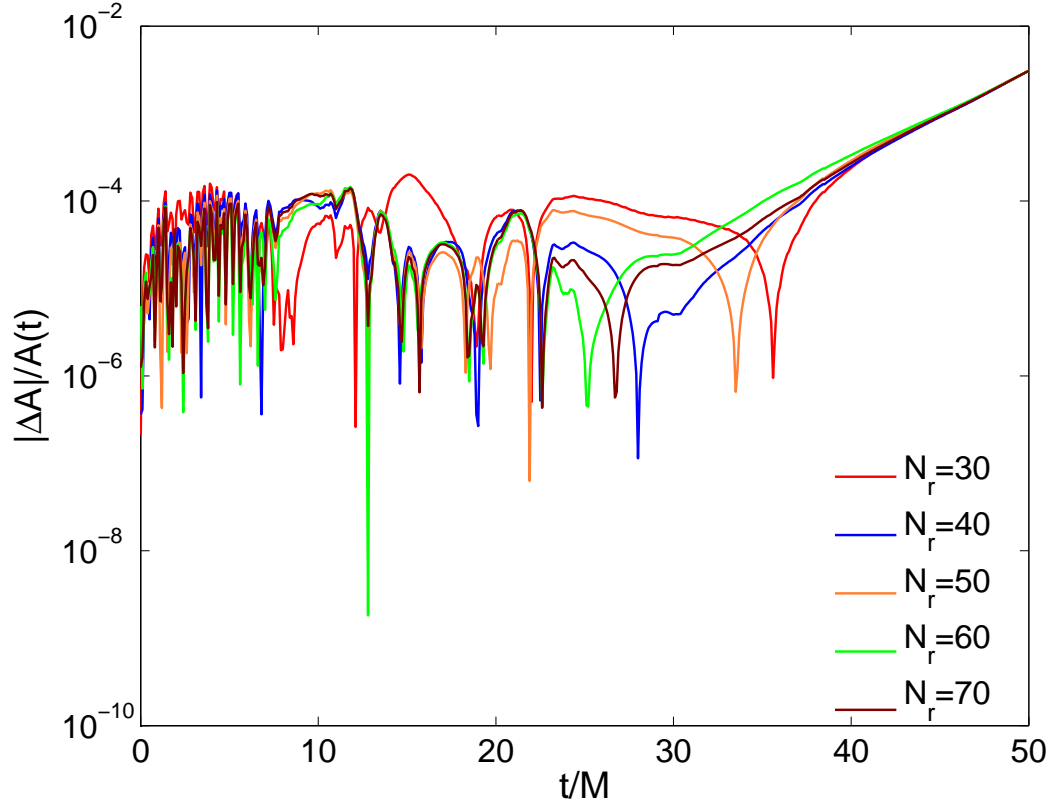


**Figure 4.4:** Normalized absolute area difference between the null surface  $\Gamma_N$  and the apparent horizon, for different orders of Chebyshev expansion:  $N_r = 30, 40, 50, 60, 70$ . The black hole is a non-spinning puncture black hole. The order of spherical harmonic expansion is kept fixed at  $L = 30$ . The event horizon finder starts at  $t = 50M$  and evolves backwards in time. The growing difference at late times reflects the event horizon tracker's exponential approach to the horizon, as it is evolved backwards in time.



#### 4.4.2 PUNCTURE BLACK HOLE WITH $a = 0.8M$

For our tests on a spacetime with a puncture black hole spinning at  $a = J/M = 0.8M$ , we choose a spheroidal initial surface:

$$r_0(\theta, \phi) = \sqrt{(x_0 \sin \theta \cos \phi)^2 + (y_0 \sin \theta \sin \phi)^2 + (z_0 \cos \theta)^2}, \quad (4.50)$$

with  $x_0 = y_0 = 0.65$  and  $z_0 = 0.55$ , which is axisymmetric. Similar to the non-spinning puncture black hole case, this choice of initial surface is slightly larger than the apparent horizon. The event horizon, however, runs for a longer time. It begins at  $t_0 = 75M$  and proceeds backwards in time towards  $t = 0M$ .

We again choose the orders at which we wish to truncate the spectral expansion of  $S$  as a measure of resolution. Because the event horizon of a significantly spinning black hole is expected to be axisymmetric but not spherically symmetric, we expect both the choices of  $N_r$  and  $L$  will affect the performance of the event horizon finder in this case. We choose  $N_r = 30, 40, 50, 60, 70$  and  $L = 16, 20, 24, 28, 30$ .

The two error measures that we will use again are Eq. (4.48) and Eq. (4.49). They are appropriate for this case because the spinning puncture black hole is the Kerr spacetime represented in a different coordinate system. However, in this case, because the event horizon is not spherically symmetric, the value of  $r_{EH}$  and  $r_{AH}$  are not independent of  $(\theta, \phi)$ . Therefore, we will measure the error in the maximum coordinate location  $r_{EH,max} = \max[r_{EH}(\theta, \phi)]$

relative to the maximum coordinate location of the apparent horizon:

$$\Delta r_{max}(t) = r_{EH,max}(t) - r_{AH,max}(t), \quad (4.51)$$

as well as the minimum coordinate location  $r_{EH,min} = \min [r_{EH}(\theta, \phi)]$  relative to the minimum coordinate location of the apparent horizon:

$$\Delta r_{min}(t) = r_{EH,min}(t) - r_{AH,min}(t). \quad (4.52)$$

There is an additional complication with the data representing a spinning puncture. It is well-known that although the data represent a vacuum solution, it is not initially a black hole. The data eventually evolve to a Kerr black hole, by ejecting an initial burst of axisymmetric gravitational radiation. Thus, in contrast to the non-spinning case, the apparent and event horizons are initially different but eventually evolve together. (The apparent horizon grows outward towards the event horizon.) Furthermore, because the spin of the black hole is chosen to be pointing in the  $z$ -axis, the maximum coordinate locations  $r_{EH,min}$  and  $r_{AH,min}$  will be found at the poles ( $\theta = 0, \pi$ ) while the minimum coordinate locations  $r_{EH,max}$  and  $r_{AH,max}$  will be found on the equator ( $\theta = \pi/2$ ).

Fig. 4.5 shows how the maximum and minimum radial coordinate locations  $r_{EH,max}$  and  $r_{EH,min}$  of the null surface  $\Gamma_N$  compare to those of the apparent horizon, throughout the evolution for  $N_r = 40$  and  $L = 30$ .

Fig. 4.6 compares the area of the null surface  $\Gamma_N$  to that of the apparent

horizon. The large deviation between the two at late times is due to the choice of initial spheroidal surface that is slightly larger than the apparent horizon. At  $t \approx 55M$ , we see that the two areas match which suggest that the event horizon finder has found the event horizon. The oscillations at times earlier than  $t \approx 55M$  are therefore not numerical artifacts, but are in fact physical effects caused by the evolution of the puncture hole.

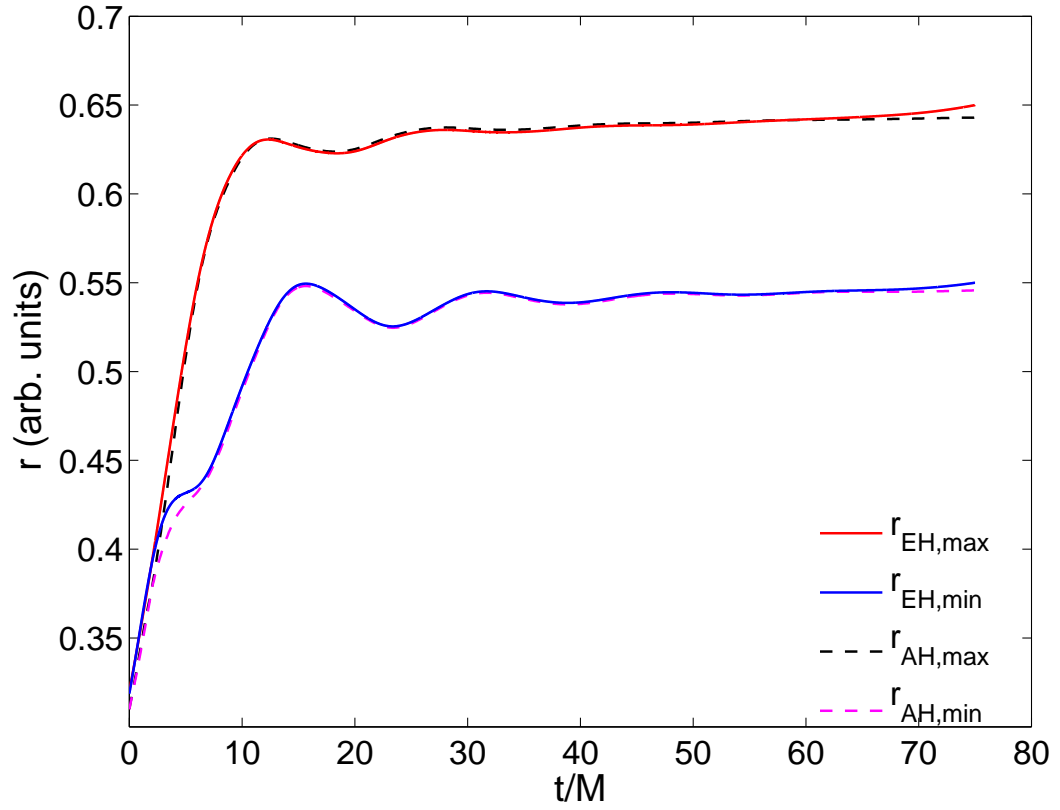
Fig. 4.7 shows how the normalized area difference changes with different choices of Chebyshev expansion  $N_r$ , and Fig. 4.8 shows how it changes with different choices of spherical harmonic expansion  $L$ . The two plots show that there is no obvious significant difference in the area for all the different choices of  $N_r$  and  $L$ .

Fig. 4.9 and Fig. 4.10 show how the absolute difference in the maximum radial coordinate locations change with different choices of  $N_r$  and  $L$ , respectively. While there is an obvious pattern that  $|\Delta r_{max}|$  is smaller for larger choices of  $L$  throughout most of the evolution ( $t \approx 10M$ – $t \approx 60M$ ), we do not see an obvious pattern for the different choices of  $N_r$ .

Similarly, Fig. 4.11 and Fig. 4.12 show how the absolute difference in the minimum radial coordinate locations change with different choices of  $N_r$  and  $L$ , respectively. We again do not find any obvious pattern for the different choices of  $N_r$  and  $L$ . However, notice that there are a number of sharp troughs for the choice of  $L = 16$ . These troughs represents the moments when the null surface and the surface of apparent horizon cross each other on the equator. As we crank up the value of  $L$ , at  $L = 30$ , the null sur-

face never crosses the surface of apparent horizon on the equator at all— $\Gamma_N$  is continually outside of the apparent horizon. For a black hole spacetime, due to the cosmic censorship conjecture, the null surface  $\Gamma_N$  should never cross the apparent horizon at all. Nevertheless, these crossings might be acceptable in numerically evolved spacetime due to numerical inaccuracies.

To sum up, with the almost negligible variation in the value of normalized  $|\Delta A|$  as we change  $N_r$  and  $L$ , we therefore conclude that the event horizon finder has performed admirably. But, we are once again limited by the resolution of the spacetime metric data. The resolution of the spacetime metric data for this spinning black hole case is equivalent to the resolution of the spacetime metric data for the non-spinning puncture black hole, which is 0.0125 (finest) spatially and  $0.00625M$  temporally. To prove this point further, the evolution in the case of  $N_r = 40$  and  $L = 32$  was unstable because of insufficient resolution in the spacetime metric data. Furthermore, because there is no significant difference in results from any of the choice of  $N_r$ , we should then choose some small  $N_r$  because of the restrictive CFL condition in the pseudospectral methods.



**Figure 4.5:** A comparison between the maximum and minimum radial coordinate locations for both the null surface  $\Gamma_N$  and the apparent horizon. In this particular case  $N_r = 40$  and  $L = 30$ . The black hole is a puncture black hole with a spin of  $J/M = a = 0.8M$ . The event horizon finder starts at  $t = 75M$  and evolves backwards in time.

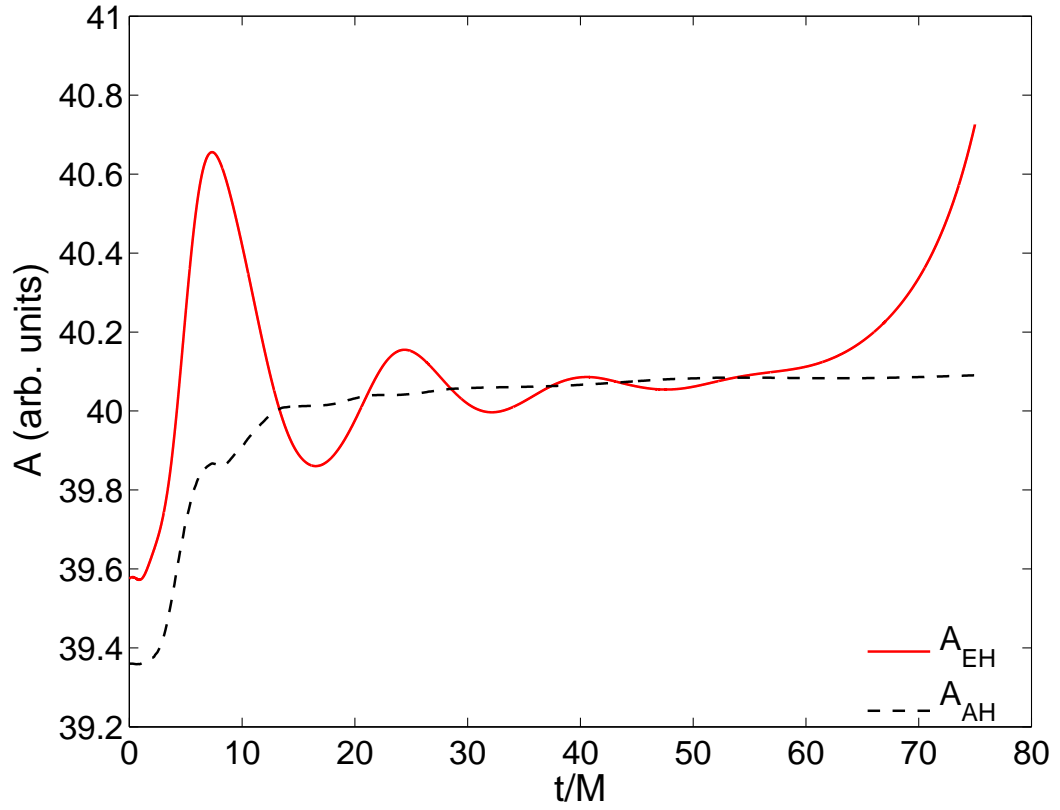


**Figure 4.6:** A comparison between the area of the null surface  $\Gamma_N$  and the area of the apparent horizon. In this particular case  $N_r = 40$  and  $L = 30$ . The black hole is a puncture black hole with a spin of  $J/M = a = 0.8M$ . The event horizon finder starts at  $t = 75M$  and evolves backwards in time.

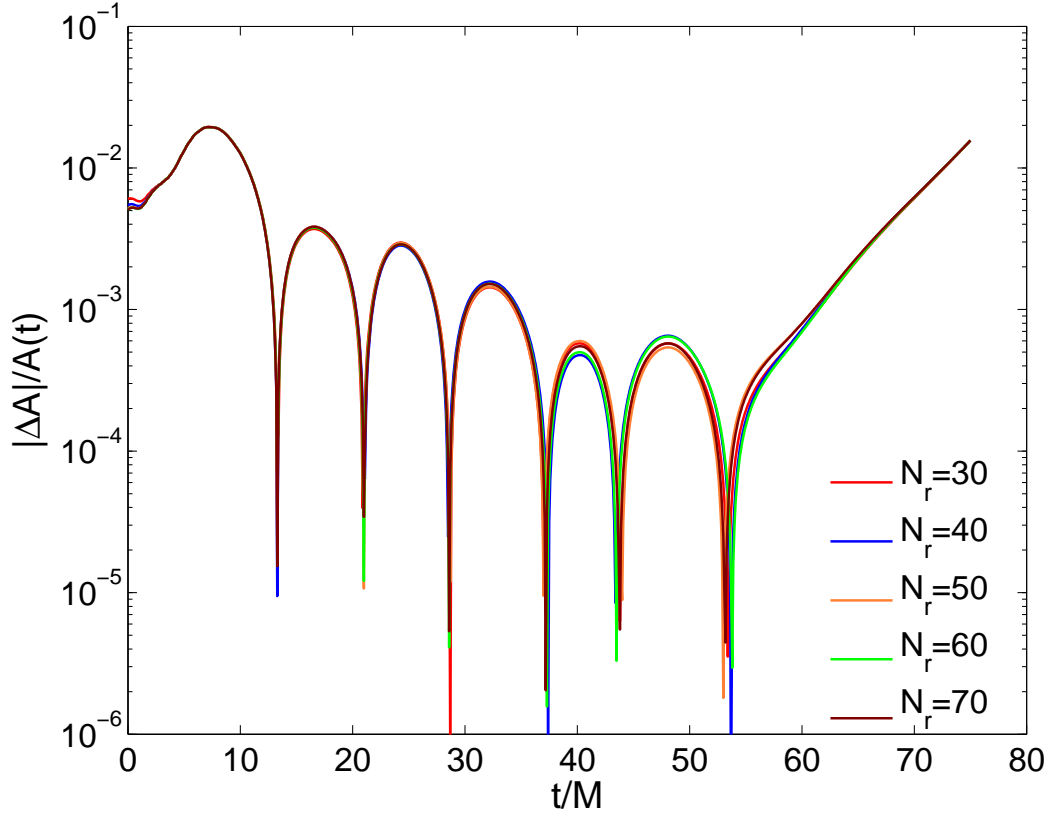


**Figure 4.7:** Normalized absolute area difference between the null surface  $\Gamma_N$  and the apparent horizon, for different orders of Chebyshev expansion:  $N_r = 30, 40, 50, 60, 70$ . The black hole is a puncture black hole with a spin of  $J/M = a = 0.8M$ . The order of spherical harmonic expansion is kept fixed at  $L = 30$ . The event horizon finder starts at  $t = 75M$  and evolves backwards in time. The growing difference at late times reflects the event horizon tracker's exponential approach to the horizon, as it is evolved backwards in time.

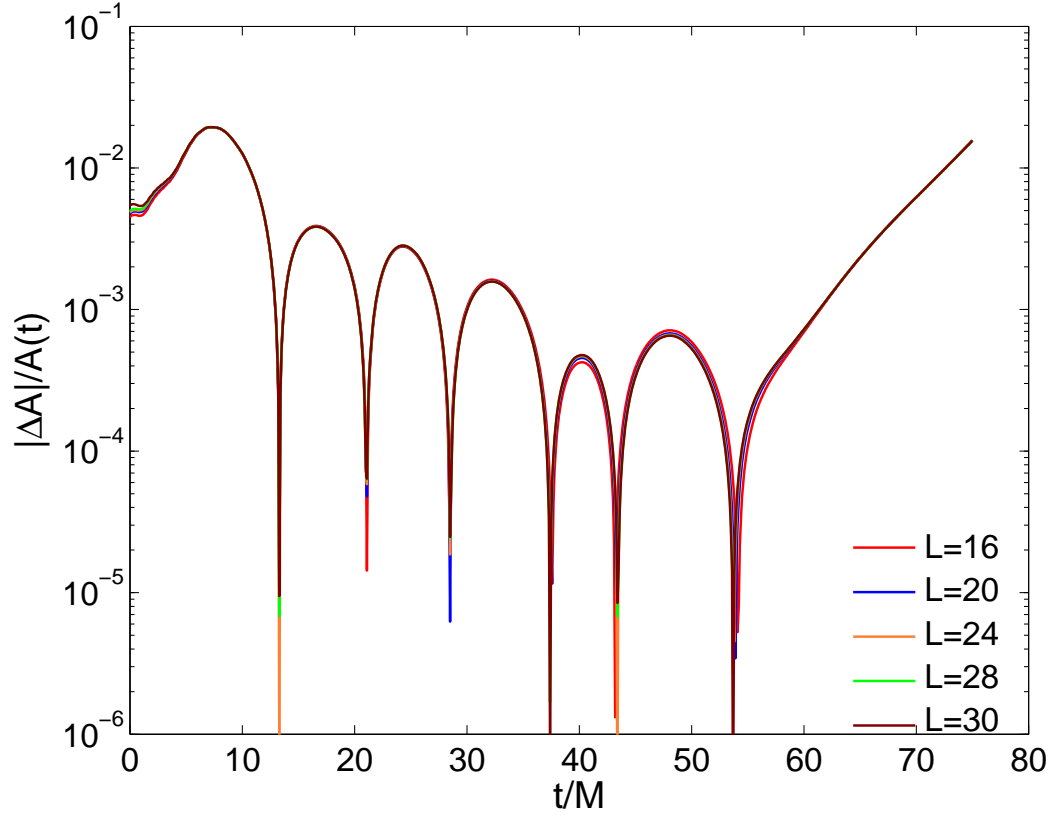


**Figure 4.8:** Normalized absolute area difference between the null surface  $\Gamma_N$  and the apparent horizon, for different orders of spherical harmonic expansion:  $L = 16, 20, 24, 28, 30$ . The black hole is a puncture black hole with a spin of  $J/M = a = 0.8M$ . The order of Chebyshev expansion is kept fixed at  $N_r = 40$ . The event horizon finder starts at  $t = 75M$  and evolves backwards in time. The growing difference at late times reflects the event horizon tracker's exponential approach to the horizon, as it is evolved backwards in time.



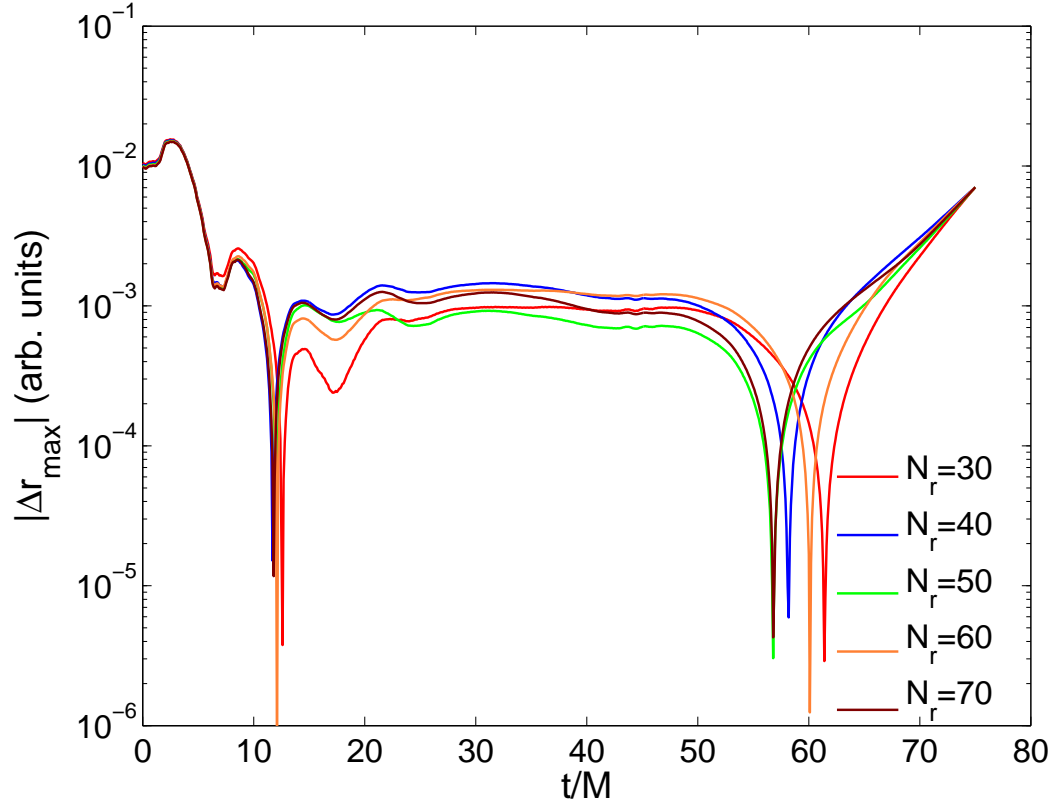


**Figure 4.9:** Absolute difference in the *maximum* radial coordinate location between the null surface  $\Gamma_N$  and the apparent horizon, for different orders of Chebyshev expansion:  $N_r = 30, 40, 50, 60, 70$ . The black hole is a puncture black hole with a spin of  $J/M = a = 0.8M$ . The order of spherical harmonic expansion is kept fixed at  $L = 30$ . The event horizon finder starts at  $t = 75M$  and evolves backwards in time. The growing difference at late times reflects the event horizon tracker's exponential approach to the horizon, as it is evolved backwards in time.

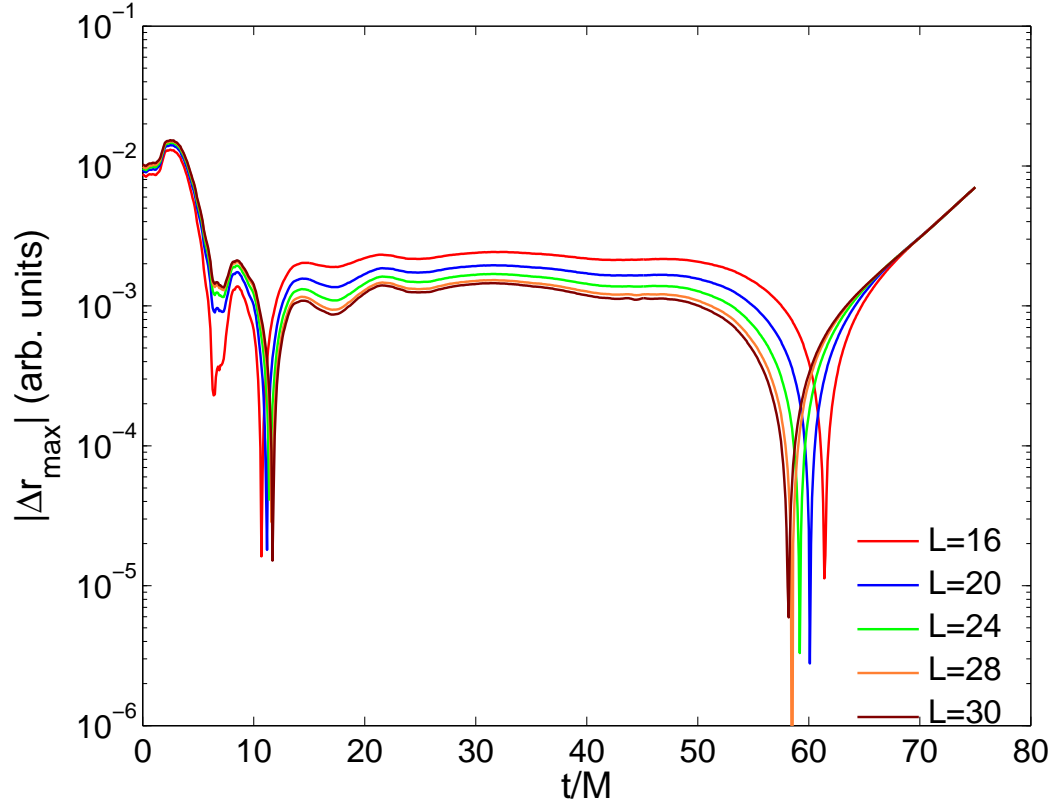


**Figure 4.10:** Absolute difference in the *maximum* radial coordinate location between the null surface  $\Gamma_N$  and the apparent horizon, for different orders of spherical harmonic expansion:  $L = 16, 20, 24, 28, 30$ . The black hole is a puncture black hole with a spin of  $J/M = a = 0.8M$ . The order of Chebyshev expansion is kept fixed at  $N_r = 40$ . The event horizon finder starts at  $t = 75M$  and evolves backwards in time. The growing difference at late times reflects the event horizon tracker's exponential approach to the horizon, as it is evolved backwards in time.

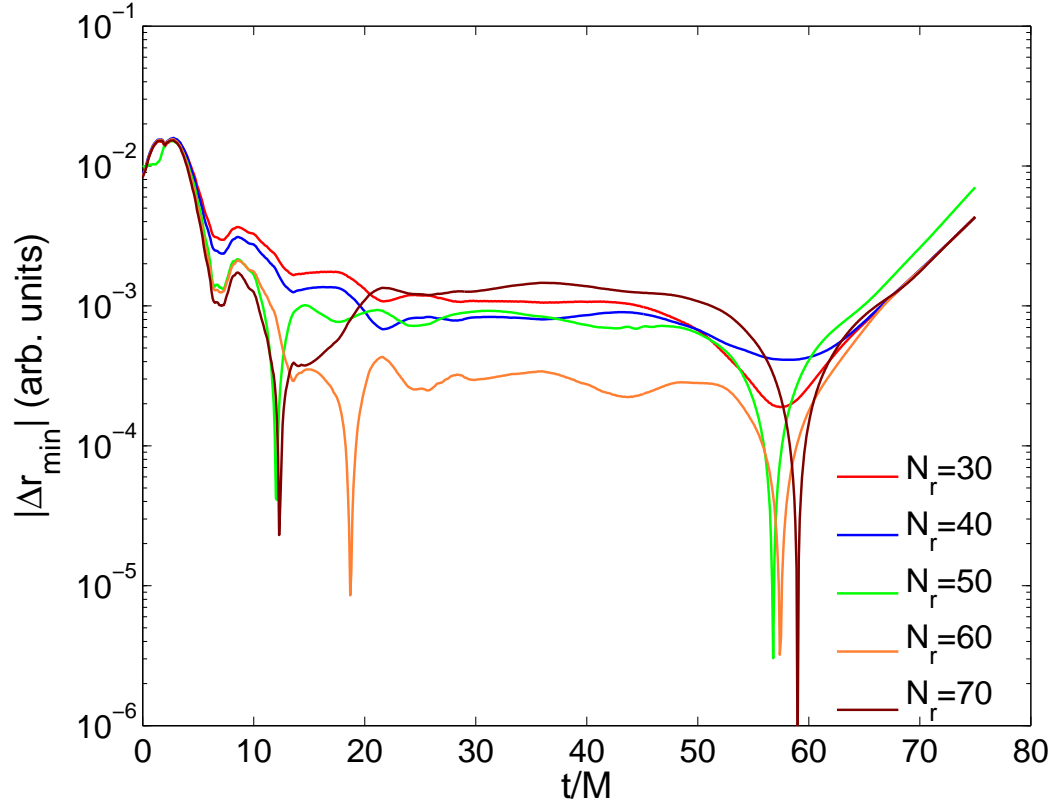


**Figure 4.11:** Absolute difference in the *minimum* radial coordinate location between the null surface  $\Gamma_N$  and the apparent horizon, for different orders of Chebyshev expansion:  $N_r = 30, 40, 50, 60, 70$ . The black hole is a puncture black hole with a spin of  $J/M = a = 0.8M$ . The order of spherical harmonic expansion is kept fixed at  $L = 30$ . The event horizon finder starts at  $t = 75M$  and evolves backwards in time. The anomalously small differences found for  $L = 16$  is probably due to an intersection between the specific values of  $L$  and  $N_r$ . The growing difference at late times reflects the event horizon tracker's exponential approach to the horizon, as it is evolved backwards in time.

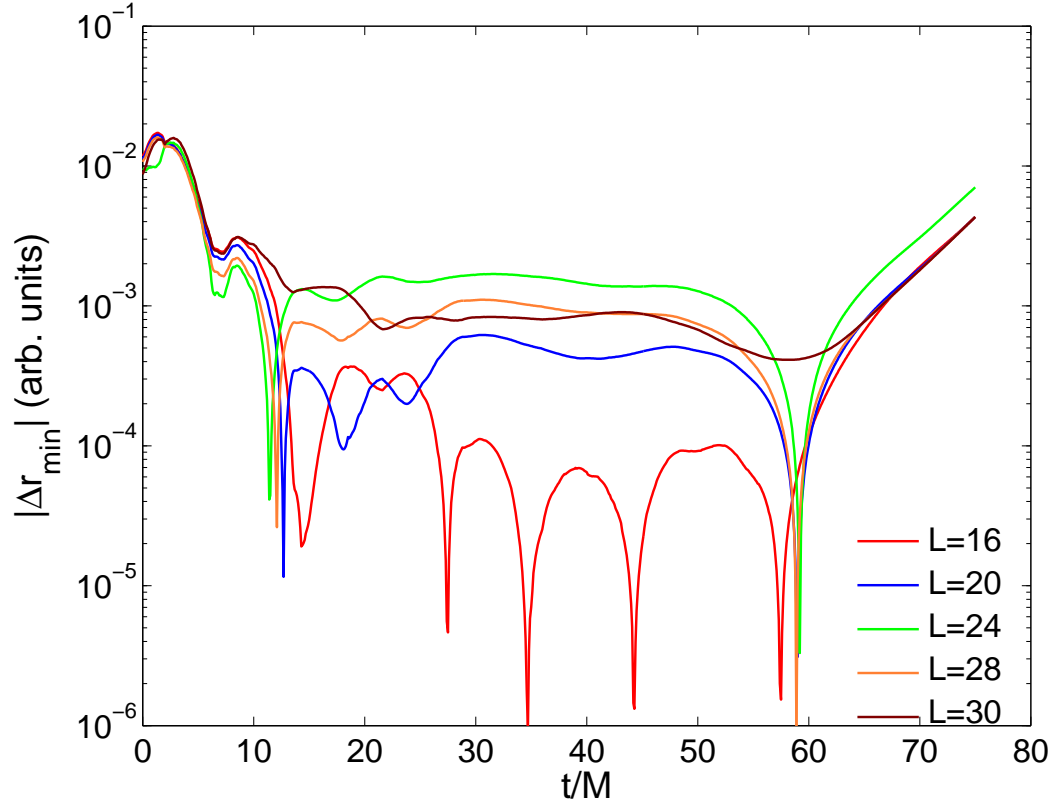


**Figure 4.12:** Absolute difference in the *minimum* radial coordinate location between the null surface  $\Gamma_N$  and the apparent horizon, for different orders of spherical harmonic expansion:  $L = 16, 20, 24, 28, 30$ . The black hole is a puncture black hole with a spin of  $J/M = a = 0.8M$ . The order of Chebyshev expansion is kept fixed at  $N_r = 40$ . The event horizon finder starts at  $t = 75M$  and evolves backwards in time. The growing difference at late times reflects the event horizon tracker's exponential approach to the horizon, as it is evolved backwards in time.

## 4.5 PUNCTURE BLACK HOLE WITH NEGATIVE ENERGY DENSITY

The numerical evolution of a black hole surrounded by a spherically symmetric cloud of negative energy density was done using the MAYA code with a matter-without-matter (MWM) evolution scheme. The MWM approach consists of evolving the spacetime geometry using the BSSN evolution equations, but without their matter source terms. The vanishing of BSSN source terms imposes specific relations between stress-energy components, but does not require vacuum, and admits negative energy density initial configurations. For more information about the evolution scheme, please refer to Ref. [26].

The black hole is a puncture black hole with an initial irreducible mass  $M_{irr} = 0.908M_0$  and Christodoulou mass  $M = 1.021M_0$ , where  $M_0$  is the ADM mass. The black hole's initial spin is the same as the isolated spinning puncture black hole in Sec. 4.4.2 where  $a = J/M = 0.8M$ . Its initial dimensionless spin parameter  $\chi = J/M^2 = 0.814$  and initial extremality parameter  $\zeta = J/(2M_{irr}^2) = 0.515$ . As the black hole is evolved in time, it accretes negative energy density such that its extremality parameter reaches  $\zeta \approx 0.60$  by the end of the evolution. This black hole is, therefore, a subextremal black hole—even though it has accreted some negative energy density. (This case is exactly equivalent to V2 case in Ref. [26].)

We choose a spheroidal initial null surface (Eq. (4.50)) with  $x_0 = 0.695$ ,  $y_0 = 0.690$ , and  $z_0 = 0.570$ . We also choose to truncate the series expansion

at  $N_r = 40$  and  $L = 30$ . The event horizon finder now begins at  $t_0 = 200M$  and proceeds backwards in time towards  $t = 0M$ .

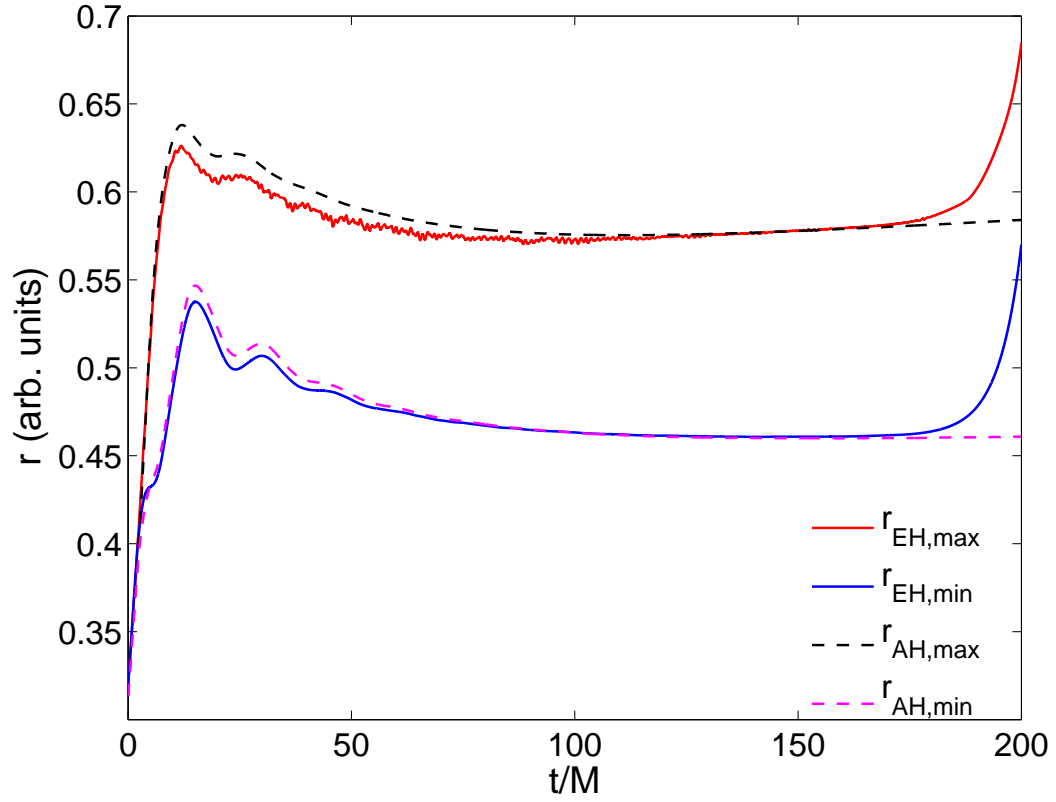
Fig. 4.13 shows a comparison between the maximum and minimum radial coordinate locations of the null surface and the apparent horizon. The apparent high-frequency oscillations in the maximum radial coordinate location  $r_{EH,max}$  and the absence of it in the minimum radial coordinate location  $r_{EH,min}$  are effects of numerical instabilities, which tend to set in at regions of lower resolution. This puncture black hole (and the previous two puncture black holes) are evolved in a nested spatial mesh with decreasing spatial resolution away from the origin. The finest spatial resolution in this case is 0.01 and it becomes coarser by a factor of two at increments of 0.26 away from the origin. The maximum radial coordinate location  $r_{EH,max}$  is located at regions with coarser spatial resolution than those for the minimum radial coordinate location  $r_{EH,min}$ ; hence, the values of  $r_{EH,max}$  tend to oscillate.

Fig. 4.13 suggests that accreting negative energy density causes the maximum and minimum radial coordinates to separate at early times. (This is not an effect of gauge choice because we are using the same spacetime slicing as the previous puncture black hole cases.) This means that the apparent horizon has a more prominent pancake shape. Nevertheless, the event horizon and the apparent horizon still show similar features.

Interestingly, even though the maximum and minimum radial coordinates of the event horizon are smaller to those of the measured apparent horizon—

especially at early times, Fig. 4.14 suggests that the area of the event horizon is almost consistently larger than that of the apparent horizon. The two areas nevertheless agree within  $\mathcal{O}(10^{-3})$  as shown in Fig. 4.15. The resolution of the spacetime metric data for this case is 0.01 (finest) spatially and  $0.005M$  temporally. Even though these resolutions are higher than those in the previous cases, the values of  $|\Delta A|/A(t)$  is larger than those measured previously because this particular black hole has a more prominent pancake shape than the others.

Moreover, this black hole does not exhibit axisymmetry. Fig. 4.16 shows a comparison between four radial coordinates of the event horizon at the equator ( $r(\theta = \frac{\pi}{2}, \phi = 0), r(\theta = \frac{\pi}{2}, \phi = \frac{\pi}{2}), r(\theta = \frac{\pi}{2}, \phi = \pi), r(\theta = \frac{\pi}{2}, \phi = \frac{3\pi}{2})$ ). For an axisymmetric black hole, all the four values of  $r$  will coincide, but this is not so for this case. Fig. 4.16 shows that this loss of axisymmetry is not merely because we started with a non-axisymmetric initial data as the radial coordinates for  $\phi = 0, \pi$  (in the  $x$ -directions) ended up at a smaller value than those for  $\phi = \frac{\pi}{2}, \frac{3\pi}{2}$  (in the  $y$ -directions), even though they started at a larger value of 0.695.



**Figure 4.13:** A comparison between the maximum and minimum radial coordinate locations for both the null surface  $\Gamma_N$  and the apparent horizon. The black hole is a puncture black hole with a spin of  $a = 0.8M$  that has accreted some negative energy density. The apparent high-frequency oscillations in the maximum radial coordinate location  $r_{EH,max}$  and the absence of it in the minimum radial coordinate location  $r_{EH,min}$  are effects of numerical instabilities. The event horizon finder starts at  $t = 200M$  and evolves backwards in time.



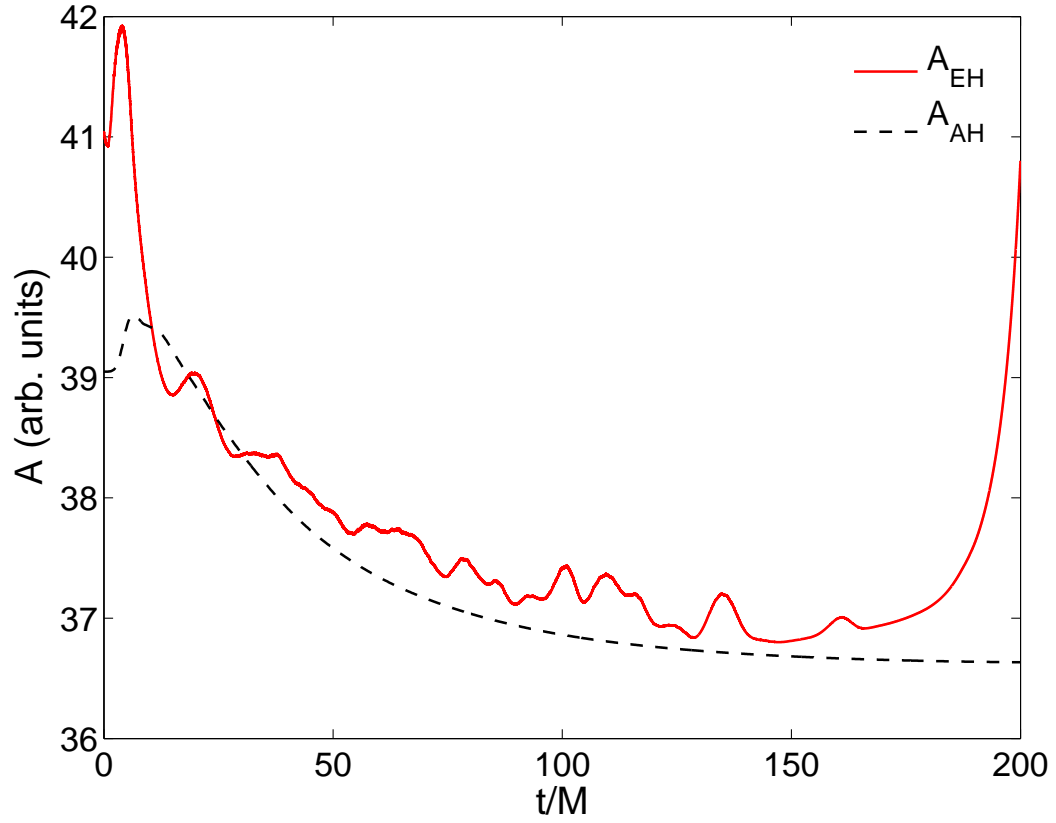


**Figure 4.14:** A comparison between the area of the null surface  $\Gamma_N$  and the area of the apparent horizon. The black hole is a puncture black hole with a spin of  $a = 0.8M$  that has accreted some negative energy density. The event horizon finder starts at  $t = 200M$  and evolves backwards in time.

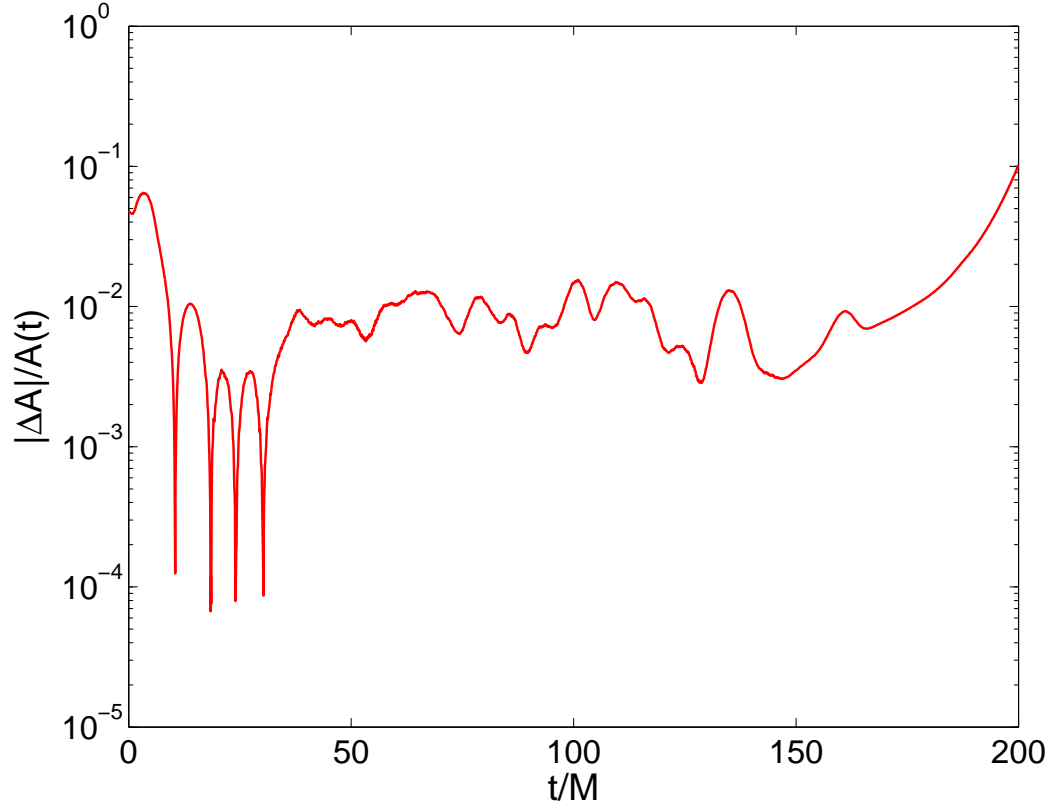


**Figure 4.15:** Normalized absolute area difference between the null surface  $\Gamma_N$  and the apparent horizon. The black hole is a puncture black hole with a spin of  $a = 0.8M$  that has accreted some negative energy density. The event horizon finder starts at  $t = 200M$  and evolves backwards in time. The growing difference at late times reflects the event horizon tracker's exponential approach to the horizon, as it is evolved backwards in time.

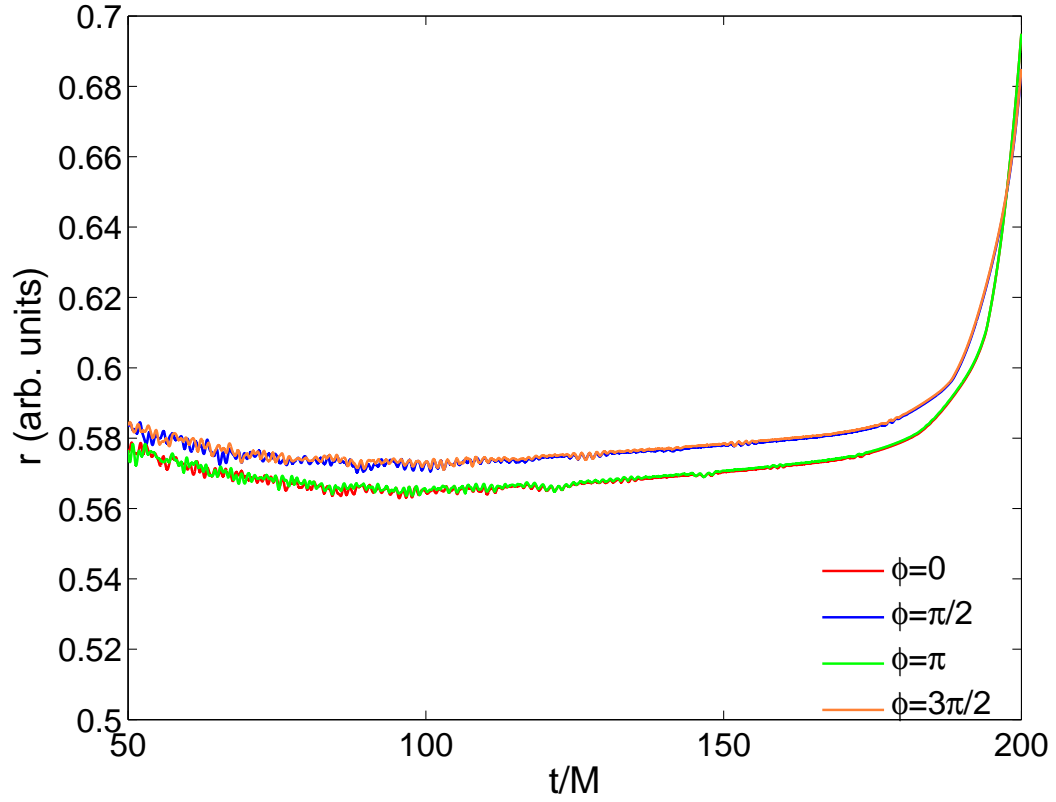


**Figure 4.16:** A comparison between the different radial coordinate locations of the null surface  $\Gamma_N$  at the equator ( $\theta = \pi/2$ )—showing the loss of axisymmetry. The black hole is a puncture black hole with a spin of  $a = 0.8M$  that has accreted some negative energy density. Only evolution between  $t = 50M$  and  $t = 200M$  is shown.

## 4.6 SUMMARY AND FUTURE CONSIDERATIONS

In this chapter, we have developed a simple, robust method of finding the event horizon of any general black hole spacetime (provided that it is a single black hole). The method is simple in the sense that we are simply propagating a null surface, which is a surface that represents a collection of photons, backwards in time. This null surface, because of the properties of the event horizon, will converge on the event horizon when evolved backwards in time.

In addition, the method is robust in the sense that it has performed admirably in locating the event horizon, measuring its area, and picking up the interesting features that the horizon might have. We observe errors in the area calculation of  $\mathcal{O}(10^{-5})$  in the spherically symmetric non-spinning black hole case and of  $\mathcal{O}(10^{-3})$  in the axisymmetric black hole case with spin of  $a = 0.8M$ . The errors in the area can mostly be attributed to the insufficient resolution in the spacetime metric data. The event horizon finder has also successfully captured the loss of axisymmetry in the case of subextremal black hole that has accreted some negative energy density. In addition, for this particular subextremal black hole case, we also observe errors in the area calculation to within  $\mathcal{O}(10^{-3})$ .

While the results in this chapter have proven that our method is simple and robust, we regret that we are currently unable to find the event horizon of a superextremal black hole because of the excessive computational costs.

Currently, to evolve the event horizon finder with  $N_r = 40$  and  $L = 30$  through the subextremal black hole case explored in 4.5, we need to use 16 Intel Xeon E5-2680 2.7GHz Processors for roughly 10 days. Most of the time is spent reading in the spacetime metric data of size 5 TB. Because the superextremal black hole cases have finer resolutions than the subextremal black hole case in 4.5, the event horizon finder would have to read a space-time metric data of approximately 25 TB, which corresponds to roughly 50 days of computational runtime. Such computational costs have become restrictive and unwieldy. Currently, we use the serial HDF5 architecture to read in the metric data [39]. A parallelized method of reading in the space-time metric data might reduce this computational time of 50 days significantly.

# 5

## Conclusions

In this thesis, we have numerically explored two different physical phenomena: gravitational lensing in strong gravitational backgrounds and event horizon surfaces. The numerical methods used employ the simple idea of following the paths of photons through curved spacetimes which satisfy the equations of general relativity. The first numerical exploration, described in Chapter 3 visualizes images that have been distorted by one or more black holes. The images are created by simply following the trails of light rays from the camera back to their sources. The second numerical exploration, described in Chapter 4, locates the event horizon of any generic single black hole spacetime. The black hole’s event horizon was found by propagating a null surface—representing a collection of photon trajectories—backwards in time until it converges to the horizon.

We have also demonstrated that implementations of both numerical simulations are robust. Both methods are robust in the sense that they are able to reliably evolve the paths of light rays not only through static spacetimes produced by one stationary black hole, but also dynamical spacetimes pro-

duced by binary black holes or by a black hole that has accreted some negative energy density. We believe that the numerical tools developed in this thesis can be instrumental in understanding the structure and the dynamics of these spacetimes. For instance, visualizing the distorted images of binary black holes allows us to directly see the amount of curvature produced by these objects. In addition, the event horizon finder code allows us to discern what the effects of swallowing negative energy density have on a black hole.

We find that, while both numerical simulations are robust, they are limited by computational requirements. For this reason, we are unable to produce high-resolution images of the binary black hole coalescence or to find the event horizon of a superextremal black hole, without paying an expensive computational costs. Novel numerical schemes are needed to reduce these costs.

These numerical simulations, however, are but a couple of applications of following the paths of photons through curved spacetimes. The same idea can also be applied to build a fully-relativistic Global Positioning System (GPS) [40], or to investigate the cosmology of our universe [41].

Ultimately, even almost a century after Einstein’s discovery of the General Theory of Relativity, light continues to play an instrumental role in pushing the frontiers of relativity further. Just as light allows us to see the distant parts of our universe, light also allows us to probe into some of the most interesting—but violent—spacetimes that we dare imagine.



# Strong Stability Preserving Runge-Kutta (SSPRK)

The five-stage fourth-order SSPRK (SSPRK{5,4}) for solving the ordinary differential equation  $\mathbf{da}^t/\mathbf{dt} = \mathcal{L}(\mathbf{a}^t)$  is as follows, [33]

$$\begin{aligned}\mathbf{a}^{(1)} &= \mathbf{a}^t + 0.391752226571890\Delta t\mathcal{L}(\mathbf{a}^t) \\ \mathbf{a}^{(2)} &= 0.444370493651235\mathbf{a}^t + 0.555629506348765\mathbf{a}^{(1)} + \\ &\quad 0.368410593050371\Delta t\mathcal{L}(\mathbf{a}^{(1)}) \\ \mathbf{a}^{(3)} &= 0.620101851488403\mathbf{a}^t + 0.379898148511597\mathbf{a}^{(2)} + \\ &\quad 0.251891774271694\Delta t\mathcal{L}(\mathbf{a}^{(2)}) \\ \mathbf{a}^{(4)} &= 0.178079954393132\mathbf{a}^t + 0.821920045606868\mathbf{a}^{(3)} + \\ &\quad 0.544974750228521\Delta t\mathcal{L}(\mathbf{a}^{(3)}) \\ \mathbf{a}^{t+\Delta t} &= 0.517231671970585\mathbf{a}^{(2)} + \\ &\quad 0.096059710526147\mathbf{a}^{(3)} + 0.063692468666290\Delta t\mathcal{L}(\mathbf{a}^{(3)}) + \\ &\quad 0.386708617503269\mathbf{a}^{(4)} + 0.226007483236906\Delta t\mathcal{L}(\mathbf{a}^{(4)}).\end{aligned}\tag{A.1}$$



where  $\mathbf{a}^t$  is a vector of the coefficients  $a_{nlm}(t)$ . This algorithm has a Courant-Friedrich-Levy (CFL) coefficient  $c = 1.508$ .

# References

- [1] J. C. Maxwell, “A dynamical theory of the electromagnetic field,” *Philosophical Transactions of the Royal Society of London* **155** (1865) pp. 459–512.
- [2] B. Schutz, *A First Course in General Relativity*. Cambridge University Press, 2011.
- [3] T. Baumgarte and S. Shapiro, *Numerical Relativity: Solving Einstein’s Equations on the Computer*. Cambridge University Press, 2010.
- [4] K. Camarda and E. Seidel, “Three-dimensional simulations of distorted black holes: Comparison with axisymmetric results,” *Phys. Rev. D* **59** (Feb, 1999) 064019.
- [5] M. D. Duez, Y. T. Liu, S. L. Shapiro, and B. C. Stephens, “Relativistic magnetohydrodynamics in dynamical spacetimes: Numerical methods and tests,” *Phys. Rev. D* **72** (Jul, 2005) 024028.
- [6] M. Shibata and Y.-i. Sekiguchi, “Magnetohydrodynamics in full general relativity: Formulation and tests,” *Phys. Rev. D* **72** (Aug, 2005) 044014.
- [7] F. Pretorius, “Evolution of binary black-hole spacetimes,” *Phys. Rev. Lett.* **95** (Sep, 2005) 121101.
- [8] M. Campanelli, C. O. Lousto, P. Marronetti, and Y. Zlochower, “Accurate evolutions of orbiting black-hole binaries without excision,” *Phys. Rev. Lett.* **96** (Mar, 2006) 111101.
- [9] J. G. Baker, J. Centrella, D.-I. Choi, M. Koppitz, and J. van Meter, “Gravitational-wave extraction from an inspiraling configuration of merging black holes,” *Phys. Rev. Lett.* **96** (Mar, 2006) 111102.
- [10] M. Shibata and K. Uryū, “Simulation of merging binary neutron stars in full general relativity:  $\Gamma = 2$  case,” *Phys. Rev. D* **61** (Feb, 2000) 064001.

- [11] M. Shibata and K. Taniguchi, “Merger of binary neutron stars to a black hole: Disk mass, short gamma-ray bursts, and quasinormal mode ringing,” *Phys. Rev. D* **73** (Mar, 2006) 064027.
- [12] F. Löffler, L. Rezzolla, and M. Ansorg, “Numerical evolutions of a black hole-neutron star system in full general relativity: Head-on collision,” *Phys. Rev. D* **74** (Nov, 2006) 104018.
- [13] M. Shibata and K. Uryū, “Merger of black hole-neutron star binaries: Nonspinning black hole case,” *Phys. Rev. D* **74** (Dec, 2006) 121503.
- [14] C. Misner, K. Thorne, and J. Wheeler, *Gravitation*:. No. pt. 3 in Physics Series. W. H. Freeman, 1973.
- [15] R. Wald, *General Relativity*. University of Chicago Press, 2010.
- [16] A. Bohn, “Building a new event horizon finder,” in *Simulating eXtreme Spacetimes (SXS) Video Conference*. 2012.
- [17] S. A. Hughes, C. R. Keeton, P. Walker, K. T. Walsh, S. L. Shapiro, and S. A. Teukolsky, “Finding black holes in numerical spacetimes,” *Phys. Rev. D* **49** (Apr, 1994) 4004–4015.
- [18] D. Krawisz, “Black hole visualization and animation,” Master’s thesis, The University of Texas at Austin, 2010.
- [19] B. J. Breen, C. E. Weidert, J. F. Lindner, L. M. Walker, K. Kelly, and E. Heidtmann, “Invitation to embarrassingly parallel computing,” *American Journal of Physics* **76** no. 4, (2008) 347–352.
- [20] A. Yumoto, D. Nitta, T. Chiba, and N. Sugiyama, “Shadows of multi-black holes: Analytic exploration,” *Phys. Rev. D* **86** (Nov, 2012) 103001.
- [21] F. H. Vincent, E. Gourgoulhon, and J. Novak, “3+1 geodesic equation and images in numerical spacetimes,” *Classical and Quantum Gravity* **29** no. 24, (2012) 245005.
- [22] D. Fenna, *Cartographic Science: A Compendium of Map Projections, With Derivations*. Taylor & Francis, 2007.

- [23] S. L. Shapiro, “Spin, accretion, and the cosmological growth of supermassive black holes,” *The Astrophysical Journal* **620** no. 1, (2005) 59.
- [24] I. Booth and S. Fairhurst, “Extremality conditions for isolated and dynamical horizons,” *Phys. Rev. D* **77** (Apr, 2008) 084005.
- [25] G. Lovelace, R. Owen, H. P. Pfeiffer, and T. Chu, “Binary-black-hole initial data with nearly extremal spins,” *Phys. Rev. D* **78** (Oct, 2008) 084017.
- [26] T. Bode, P. Laguna, and R. Matzner, “Superextremal spinning black holes via accretion,” *Phys. Rev. D* **84** (Sep, 2011) 064044.
- [27] M. I. Cohen, H. P. Pfeiffer, and M. A. Scheel, “Revisiting event horizon finders,” *Classical and Quantum Gravity* **26** no. 3, (2009) 035005.
- [28] J. Libson, J. Massó, E. Seidel, W.-M. Suen, and P. Walker, “Event horizons in numerical relativity: Methods and tests,” *Phys. Rev. D* **53** (Apr, 1996) 4335–4350.
- [29] P. Diener, “A new general purpose event horizon finder for 3d numerical spacetimes,” *Classical and Quantum Gravity* **20** no. 22, (2003) 4901.
- [30] S. A. Caveny, M. Anderson, and R. A. Matzner, “Tracking black holes in numerical relativity,” *Phys. Rev. D* **68** (Nov, 2003) 104009.
- [31] R. M. Wald and V. Iyer, “Trapped surfaces in the schwarzschild geometry and cosmic censorship,” *Phys. Rev. D* **44** (Dec, 1991) R3719–R3722.
- [32] C. F. Gammie, S. L. Shapiro, and J. C. McKinney, “Black hole spin evolution,” *The Astrophysical Journal* **602** no. 1, (2004) 312.
- [33] J. Hesthaven, S. Gottlieb, and D. Gottlieb, *Spectral Methods for Time-Dependent Problems*. Cambridge Monographs on Applied and Computational Mathematics. Cambridge University Press, 2007.
- [34] J. Boyd, *Chebyshev and Fourier Spectral Methods*. Dover Books on Mathematics Series. Dover Publ., 2001.

- [35] W. Press, *Numerical Recipes 3rd Edition: The Art of Scientific Computing*. Numerical Recipes: The Art of Scientific Computing. Cambridge University Press, 2007.
- [36] F. Lekien and J. Marsden, “Tricubic interpolation in three dimensions,” *International Journal for Numerical Methods in Engineering* **63** no. 3, (2005) 455–471.
- [37] T. W. Baumgarte and S. L. Shapiro, “Numerical integration of einstein’s field equations,” *Phys. Rev. D* **59** (Dec, 1998) 024007.
- [38] M. Shibata and T. Nakamura, “Evolution of three-dimensional gravitational waves: Harmonic slicing case,” *Phys. Rev. D* **52** (Nov, 1995) 5428–5444.
- [39] The HDF Group, “Hierarchical data format version 5,” 2000-2010.
- [40] D. Bunandar, S. A. Caveny, and R. A. Matzner, “Measuring emission coordinates in a pulsar-based relativistic positioning system,” *Phys. Rev. D* **84** (Nov, 2011) 104005.
- [41] M. V. Sazhin, O. S. Khovanskaya, M. Capaccioli, G. Longo, M. Paolillo, G. Covone, N. A. Grogin, and E. J. Schreier, “Gravitational lensing by cosmic strings: what we learn from the csl-1 case,” *Monthly Notices of the Royal Astronomical Society* **376** no. 4, (2007) 1731–1739.